GROWTH OPTIMIZATION AND PROCESS DEVELOPMENT OF INDIUM GALLIUM NITRIDE/GALLIUM NITRIDE SOLAR CELLS

A Thesis
Presented to
The Academic Faculty

by

Matthew B. Jordan

In Partial Fulfillment
of the Requirements for the Degree
Doctor of Philosophy in the
School of Electrical and Computer Engineering

Georgia Institute of Technology
May, 2017

GROWTH OPTIMIZATION AND PROCESS DEVELOPMENT OF INDIUM GALLIUM NITRIDE/GALLIUM NITRIDE SOLAR CELLS

Approved by:

Dr. Abdallah Ougazzaden, Advisor
Director, Co-President, Professor
Georgia Tech Lorraine, UMI GT-CNRS, Institut Lafayette

Dr. David Citrin
Professor, ECE
Georgia Institute of Technology

Dr. Paul Voss
Associate Professor, ECE
Georgia Institute of Technology

Dr. Thomas Sanders
Regents Professor, MSE
Georgia Institute of Technology

Dr. Jean Paul Salvestrini
Directeur du laboratoire, Professor
LMOPS, Supelec, Georgia Tech Lorraine

Date Approved: March 28, 2017

If I have seen further it is by standing on the shoulders of giants.

–Sir Isaac Newton, 1676

I'd put my money on the sun and solar energy. What a source of power! I hope we don't have to wait until oil and coal run out before we tackle that.

–Thomas Edison, 1931

ACKNOWLEDGEMENTS

I'd like to express my gratitude to my advisors, Dr. Abdallah Ougazzaden, Dr. Paul Voss, and Dr. Jean Paul Salvestrini during the completion of this work. This thesis would not have been possible without their knowledge, expertise, and guidance. Furthermore I feel that their confidence in my work allowed me to grow as a scientist, engineer, and researcher. A heartfelt thanks goes out to the other members of my PhD committee who's patience and support has been unwavering during the completion of this thesis. I'd also like to thank the institutions and funding partners that made this work possible. Georgia Tech and Georgia Tech Lorraine have been very supportive during the completion of my PhD. Generous grants from the French National Research Agency (ANR) under the NOVAGAINS (Grant number ANR-12-PRGW-0014-02) and GANEX Laboratory of Excellence (Grant number ANR-11-LABX-0014) have helped make this work possible. Much of the work has been carried out using the equipment, personnel, and resources of the Georgia Tech-CNRS, UMI2958, Centrale Supelec, LMPOS, EA4423, Institut Lafayette, and Georgia Tech IEN laboratories. Further work has been carried out at CNRS, ICube at the Université de Strasbourg, GeePs, CNRS UMR8507, Centrale Supelec, INL – Lyon, CNRS, UPR LPN, and Nanovation.

I'd like to extend my gratitude personally to the other PhD students and colleagues who have assisted in various ways in the making of this thesis. To Suresh Sundaram, Xin Li, and Tarik Moudakir who assisted with MOVPE growth. To Muhammad Arif, Jeremy Streque, Youseff El Gmili who have assisted with characterization. To Walid Elhuni who's work is presented on the modeling of InGaN/Si solar cells.

Finally I would be remiss if I did not thank my family and friends for their love

and support.

TABLE OF CONTENTS

LIST OF TABLES

LIST OF FIGURES

SUMMARY

Chapter one is an introductory chapter defining some basic physics that are important to solar cells as well an introduction to the economic pressures driving solar cell innovation and the state of the art for various types of solar cells.

Chapter two deals with the material indium gallium nitride. The material properties are discussed followed by a discussion of InGaN solar cells. We discuss our laboratory's approach to InGaN solar cells, namely optimizations of the semibulk growth method. We also demonstrate how semibulk InGaN can be used to produce a very high quality solar cell absorber resulting in a high short circuit current. Through this process we found that we may be able to improve the solar cell by optimizing the processing. Lastly we discuss simulations performed on InGaN/Si tandem solar cells and show that this is a promising route to high efficiency solar cells.

In order to decouple the material quality from the device processing and focus on optimizing the solar cell process we use LED samples. We then deconstruct each step of the process and describe the steps we used to optimize them in chapter three. Specifically we discuss:

- Device Design
- GaN Etching
- V-Pits – How they effect solar cell performance and how to passivate them
- Metal contacting to n-GaN – Materials, Improving the specific contact resistance, and yield
- Metal contacting to p-GaN – The transport mechanisms associated with the contacts, various studies optimizing the contact, and the measured effect of the

contact on the electrical performance.

- Passivation of the mesa
- And the next steps – Chiefly investigating the p-contact's optical properties, other p-contact materials, passivation, and antireflective coatings

In this chapter we present device results from LEDs. These LEDs were also characterized as solar cells and used in and InGaN/Si solar cell tandem. We discuss alternative paths to high efficiency InGaN based solar cells and demonstrate InGaN based solar cells grown on BN as well and nanoselective area growth solar cells.

Finally in the last chapter we conclude by briefly recapping the work that has been done as well as what is left to be done to achieve high efficiency InGaN/Si tandem solar cells.

CHAPTER I

INTRODUCTION

The photovoltaic effect is a phenomenon wherein a voltage or current will be induced in a material through exposure to light. The first photovoltaic device was demonstrated by Alexandre-Edmond Becquerel in 1839 and since then photovoltaics have been developed to power everything from handheld calculators to spacecrafts. The advancements in photovoltaics over the past century coincide in no small part with the developments made in the field of microelectronics. Indeed, just as silicon has dominated the microprocessor industry, most solar cells used on the earth (as opposed to those used in outer space) are made from silicon [20]. Silicon has many properties that are beneficial to both industries including its mineral abundance in nature, ease of manufacturing (through Czochralski, float zone, and other crystal growth methods), and the fact that it is a single component semiconducting crystal system [20]. However, silicon is not without drawbacks when used for photovoltaics: it is not possible to tune the energies of light that silicon absorbs and due to the indirect structure of the silicon band gap thicker cells are required to absorb light and energy is lost to phonons [21]. Fortunately our knowledge of other material systems, like indium gallium nitride (InGaN), and crystal growth methods, such as metalorganic vapor phase epitaxy (MOVPE), have improved and it makes sense to investigate the opportunities that these materials provide to the manufacturing of better solar cells. In this work we present the opportunities and challenges that of growing and processing of InGaN devices. We will also show advancements that our laboratory, as well as others, have developed for producing solar cells. Finally, we will propose further refinements to the processes involved in fabricating InGaN solar cells as well as tests of the InGaN

solar cell system.

1.1 The Solar Spectrum

When introducing the topic of solar power, an obvious place to begin is with a basic understanding of the sun and the pathway that the light from the sun takes to reach us on the surface of the earth. In the core of the sun nuclear fusion reactions produce heat raising the temperature to over 20 million degrees Kelvin. The light from the core of the sun is strongly absorbed by the other layers and so is self-attenuated. Thus, very little light from the core escapes, however it does heat the outer layers of the sun, like the photosphere, to approximately 6000 K [22, 23]. The surface of the sun acts like a blackbody and radiates light whose spectrum is closely approximated by Planck's equation (see figure 1). Not all of the light incident on the earth reaches the ground, however. The amount of light reaching an area on earth depends on where that area is, the time of year, absorption and scattering of light in the atmosphere, local weather conditions, and of course the time of day. In the atmosphere ozone, water vapor, dust, and the air molecules themselves can absorb and scatter light. On a clear day at the equator (AM1) only 70% of incident light directly reaches the earth's surface. 18% of the light is absorbed, some of the scattered light, about 7%, and reaches the ground as diffuse radiation, and around 3% of the light is reflected back into space [24]. The losses caused by solar radiation traveling in the atmosphere are taken into account using a parameter called the Air Mass. This parameter is defined using the zenith angle (displacement from vertical), θ, of the sun: AM= $\frac{1}{\cos\theta}$. In practice solar cells on the earth collect light from areas that have an air mass higher than 1. Thus for testing a standard of air mass 1.5 was proposed, which corresponds to a zenith angle of 48.2° and with locations on earth between Caribou, ME and Phoenix, Az depending on the season [6]. The 6000 K blackbody model of the solar spectrum as seen from earth, as well as the measured AM0 (extraterrestrial) and the

standard AM1.5 G spectra are shown in figure 1.

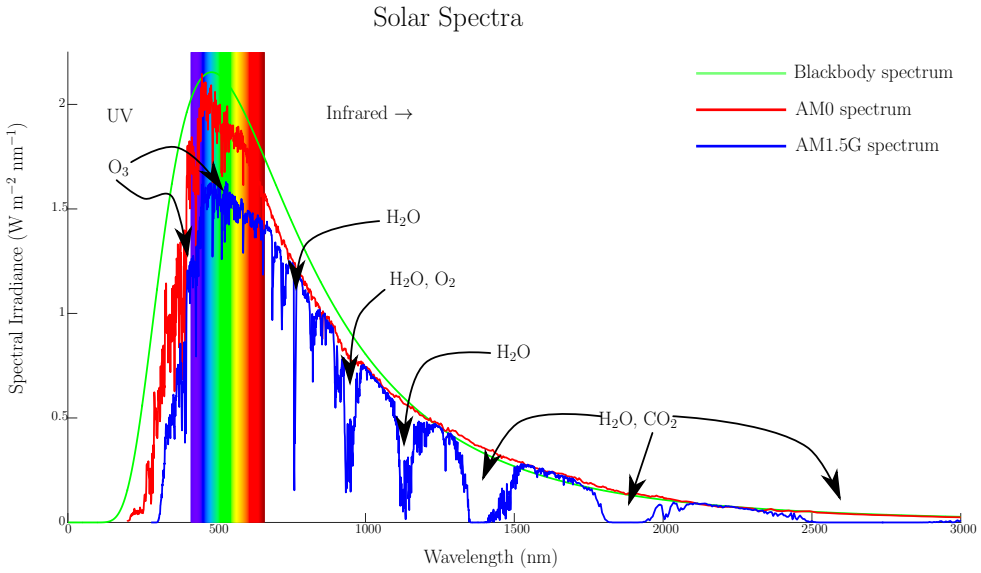

Figure 1: Solar Spectrum as approximated by the sun being an ideal 6000 K blackbody, the WMO/WRDC Wehrli AM0 (extraterrestrial) standard, and the ASTM G-173 (AM1.5G) standard terrestrial spectra with the visible wavelengths highlighted and some absorption lines from atmospheric molecules indicated [6].

The solar spectrum is the power source for all solar cells. What makes the difference between two solar cells is not the spectrum, but the materials and processes that go into making each cell. Therefore, it makes sense to describe how solar cell absorber and then convert light to electricity.

1.2 Basic Semiconductor Physics

1.2.1 Light Absorption in Semiconductors

Todays solar cells are formed from semiconductor materials like Si, Ge, CdS, CdTe, and more. This is done so that engineers can utilize the unique properties of each of these semiconductor materials to collect power generated when the cell is exposed to light. Thus to fully comprehend the function and issues associated with the manufacturing of photovoltaic cells today we must have a strong foundation of knowledge in the electronic structure of semiconductors and semiconductor physics.

The structure of semiconductors gives rise to energy bands where charged particles, like electrons, in the semiconductor can have only specific energies while others are forbidden. The size of the forbidden zone is described by E_g, the band gap energy as shown in figure 2 (a). When light enters the semiconductor it's energy can be absorbed. Only light with an energy, $E = h\nu$ (for the definition of various mathematical symbols or constants refer to Appendix I: Symbols and Physical Constants), greater than the band gap energy of the semiconductor can be absorbed. This light will, through the photovoltaic effect, excite an electron from the valence band, E_V, into the conduction band, E_C as depicted in figure 2 (c) and (d).

The diagrams of figure 2 are simplifications of possible states that electrons can have in semiconductors, and the band gap separates the two energy regimes in that state space: the valence and conduction bands. Since electrons are fermions they must abide by the Pauli exclusion principle, that is that no two electrons can share the same state. In the valence band most of the states are occupied by other electrons. Because of this the electrons cannot move freely and thus the electrons in the valence band do not contribute to electrical conduction. In the conduction band however most of the states are free and so electrons redistribute in space and conduct electricity. Energy put into the system in the form of light or heat or other forms can give electrons in the valence band the necessary energy to overcome the band gap and move in the conduction band. When an electron gains the energy to be in the conduction band (as occurs in figures 2 (c) and (d)) a vacancy is left behind and the residual charge of the protons in the atoms of the semiconductor give this vacancy a +1 charge. This vacancy is commonly referred to as a hole and behaves much as if it were an actual particle of positive charge that can move in the valence band.

Different semiconductors have different band gap energies and thus will absorb different energies of light. There is a tradeoff between amount of light from the spectrum that is absorbed and the amount of energy lost to heat. Furthermore, to

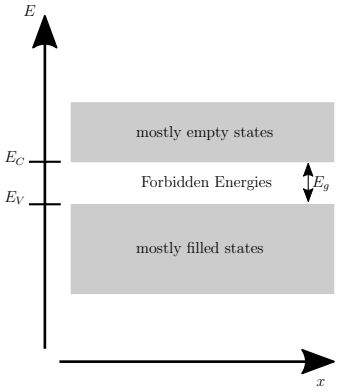

(a) Electronic Structure of Semiconductors

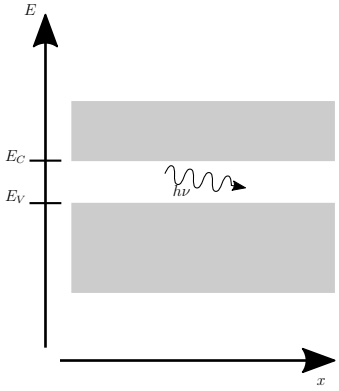

(b) $h\nu < E_g$, No light absorption. Semiconductor is transparent to light of this energy

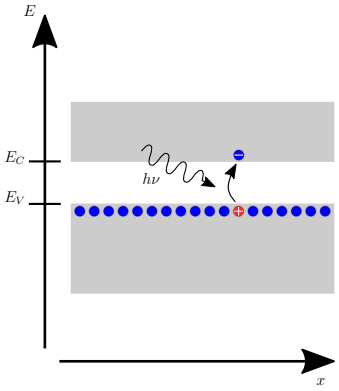

(c) $h\nu = E_g$, Light is absorbed with the energy equal to the band gap (direct semiconductors)

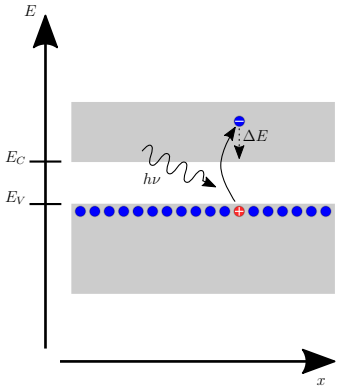

(d) $h\nu > E_g$, Light is absorbed and excess energy, ΔE, is lost to heat

Figure 2: (a) Depiction of the conduction band, valence band, and band gap energy in a semiconductor (E_C, E_V, and E_g respectively). (b) - (d) Absorption of light of various energies in a semiconductor.

collect power solar cells work on the principle of the pn junction.

1.2.2 Doping, PN Junctions, and Recombinations

Pure semiconductor crystals are not very conductive at low temperatures. Figure 3 (a) shows a description of occupied of states in a semiconductor at various temperatures as described by Fermi Dirac statistics. At absolute 0 temperature all the electrons are packed into the lowest energy states in the valence band. The energy

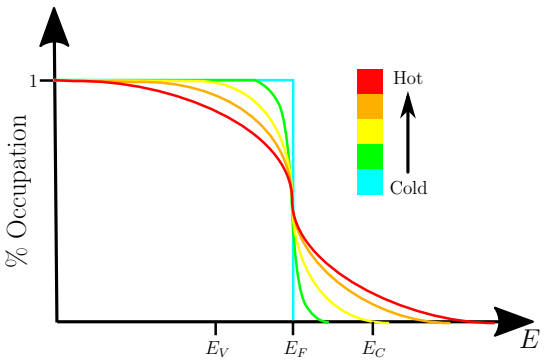

(a) Occupation of states around the fermi level

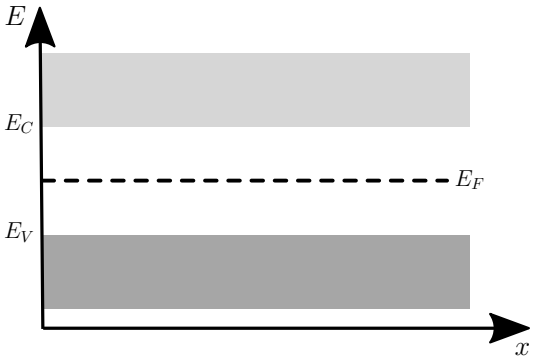

(b) An intrinsic semiconductor with fermi level indicated

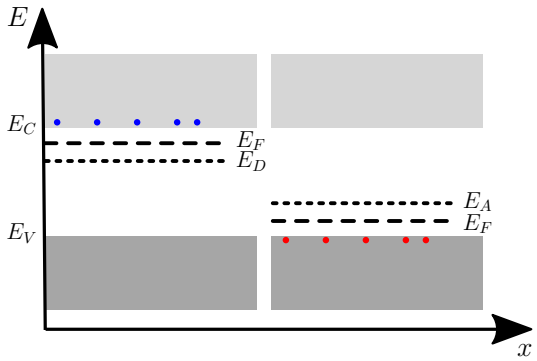

(c) n-type and p-type doped semiconductors with example electrons and holes

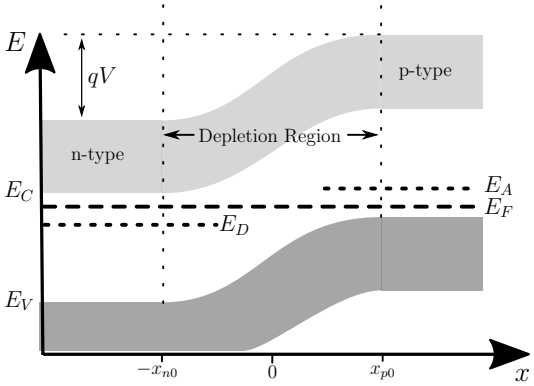

(d) an np junction in a semiconductor with energies indicated

Figure 3: Occupation of states at different temperatures in a semiconductor as well as a description of doping and the formation of an np junction

level that all of the electrons are under at 0 K is called the fermi level, E_F. As the semiconductor is heated more and more electrons have the energy to occupy the conduction band. Often, especially with wide band gap semiconductors, at room temperature the semiconductors are still not very conductive. Thus it is common to intentionally add impurities, called dopants, to increase the amount of carriers in the semiconductor. These impurities have a different number of outer shell electrons than the semiconductor material, that is they are not *isoelectronic* to the semiconductor material. The dopants also perturb the crystal lattice of the semiconductor and create additional energy levels within the band gap as depicted in figure 3 (c). If the energy of the dopant is close to the conduction band and the dopant has more electrons than

the intrinsic semiconductor it is called a donor because it will readily "donate" its electrons to the conduction band. Whereas if the dopant energy is close valence band and it has fewer electrons than the semiconductor it is called an acceptor. Ideally the energies involved are low enough that at room temperature most of the donors have lost their electrons and most of the acceptors have gained extra electrons thus resulting in a higher than normal amount of electrons in the conduction band and holes in the valence band. Examples of donors and acceptors in silicon include phosphorus (donor) and boron (acceptor) [7]. When a semiconductor device is made with a gradient of doping concentrations a junction is formed. Electrons in the conduction band and holes in the valence band will distribute to cancel out charge of the junction and the end result is depicted in figure 3 (d).

In an np or pn junction the fermi levels equalize and the conduction and valence bands bend. The amount that the valence and conduction bands bend is called the built-in potential, qV. This can be calculated from the concentration of donors, N_D, acceptors, N_A, as well as the intrinsic carrier concentration for this semiconductor at room temperature, n_i (assuming all donors and acceptors are ionized) by the following equation [7]:

$$V = \frac{kT}{q} \ln\left(\frac{N_A N_D}{n_i^2}\right) \tag{1}$$

All constants can be found in Appendix I: Symbols and Physical Constants.
The zone where the bands are bending is called the depletion region. This zone is between the x_{n0} and x_{p0} junction depths and has a depletion width defined as $W_0 = x_{n0} + x_{p0}$. In the depletion region electrons and holes have recombined cancelling each other out.

There are several ways in which electrons and holes can be generated or can recombine to cancel each other out. Firstly holes in the valence band and electrons in the conduction band can be generated or recombine directly with the absorption or emission of light. This is called direct band-to-band generation or recombination

and the rates are shown in figure 4 as G and R respectively. The energy released in band-to-band recombinations often results in photons and so is called radiative recombination. Direct band-band generation and recombination is more likely to

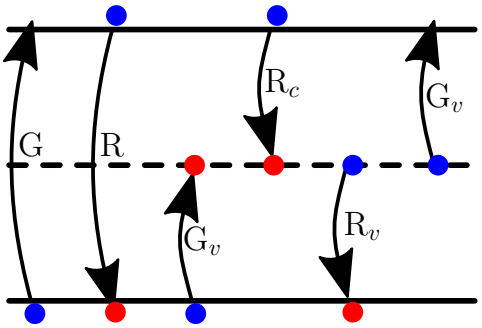

(a) Band to band and SRH generation and recombinations

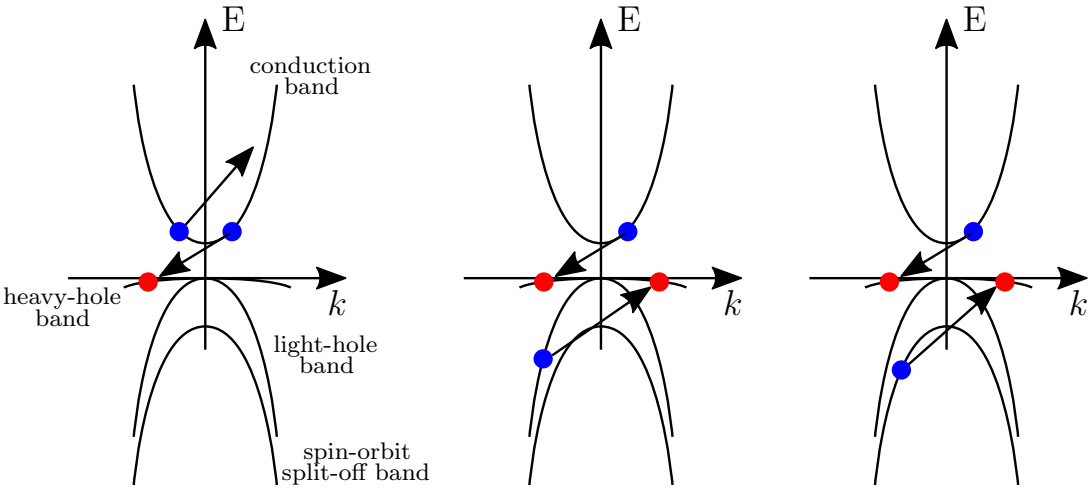

(b) CHCC (c) CHLH (d) CHSH

Figure 4: Some types of recombination and and generation. (a) Direct (R and G) and SRH (R_v, R_v, G_c, and G_c) recombinations and generations. (b-d) Auger recombinations where energy from an electron in the conduction band recombining with a hole in the valence band is transferred to (a) another electron in the valence band (CHCC type), (b) an electron in the LH band becoming excited and moving to an unoccupied location on the HH band (CHLC type), and (d) an electron in the SO band becoming excited and moving to an unoccupied location on the HH band (CHSH type) [7]

occur between electrons and holes that have the same momentum (related to k in figure 4 (b-d)) and thus is most likely to occur in direct band gap materials. In order for band-to-band generation and recombination to occur in indirect band gap

materials, like silicon, a third virtual particle called a phonon must also interact with the electron and hole so that momentum is conserved. Secondly, impurities and defects in the semiconductor crystal lattice can introduce energy levels in the band gap called traps. Electrons can move from the valence and conduction bands into these trap levels in a process described by Shockley Read and Hall and are thus called SRH recombinations. The energy released from SRH recombinations are usually given to the crystal lattice in the form of phonons, or vibrations that can dissipate as heat. Thus band-to-trap recombinations are generally non-radiative. The other major type of recombination is Auger recombination. This occurs when the energy released by the recombination of the electron and hole is transferred to a third particle. This occurs most often in direct band gap semiconductors with a small band gap at elevated temperatures. The three possible Auger recombination mechanisms are shown in figure 4 (b-d).

Knowledge of band gap energies, pn junctions, recombinations, and defects is essential to the design of successful solar cells. In the next section we'll investigate how this information is employed to define the solar cell efficiency as well as the use of InGaN as a material for solar cells, the challenges associated with using InGaN, and progress made in the scientific community towards efficient InGaN based solar cells.

1.3 Solar Cells

An understanding of the solar spectrum and semiconductor physics that govern the absorption and collection of solar energy are essential to the development of solar cells. However, photovoltaics is not a new subject and there are many competing technologies both in the laboratory and commercial markets. An overview of these technologies is presented to provide context for InGaN solar cells and to show the pressures driving innovation in solar cells. Furthermore by investigating the solutions

to problems faced by other solar cell technologies we can adapt the technology and gain inspiration for InGaN solar cells.

1.3.1 The Economics of Solar Power

The energy sector is an extremely competitive area of the economy. The total cost of solar cells must be understood in order to determine how much a it costs to make electricity can be produced. This figure of merit can be analyzed in many ways: levelized cost of electricity, energy payback time, *etc.*. Fundamentally these equations have two parts. First, how much does electricity cost, and second how much electricity is made by the solar cell per dollar. The amount of electricity made by a certain solar cell depends on the type of cell used. The national renewable energy laboratory (NREL) in the United States benchmarks various solar cell technologies and maintains a database of solar cell performance for a number of types of solar cells. As time passes there are more and more materials designs used to make solar cells and the conversion efficiency of each design increases. Many of these materials and designs, and their limitations are the subject of the subsequent sections of this chapter. However, before discussion of the differences between Si and CdTe solar cells we should fill in the remaining pieces of the economic equation: the cost of solar cells and a comparison of the cost of electricity produced by solar power and other sources like nuclear and coal.

The costs of solar power are often broken into three components: the cost of the solar cell module, the cost of the inverter, and "balance of systems" (BOS) costs which cover everything else from the wiring to the frames and the solar trackers used in CPV systems. The module cost depends on the type of solar cell that is used (Si, CIGS, flat panel, concentrated, *etc.*). For example for an unconcentrated solar module set on an incline in southern Europe the largest factor in the cost of a crystalline Si solar cell module is the production of the crystalline Si itself, while for a CIGS cell, which

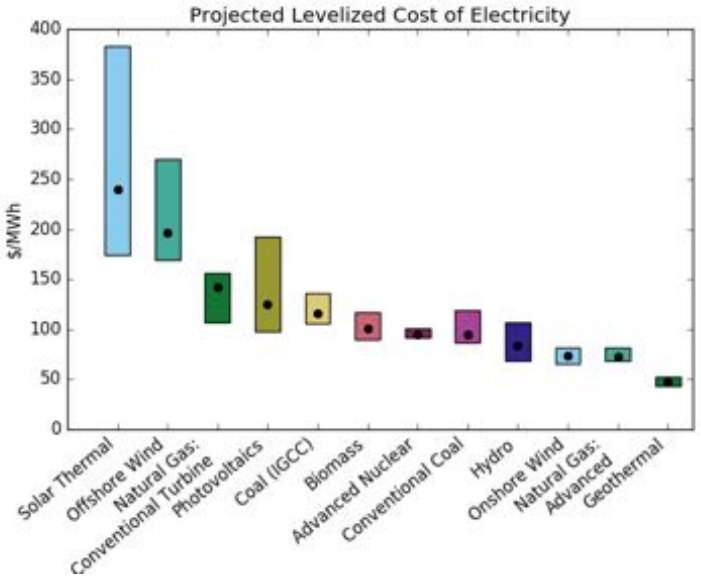

Figure 5: Forecast of the LCOE of various technologies in the US in 2022[8]

is more fragile and potentially more toxic, the primary costs are the laminates used in the production of the module[25]. Other factors that enter into the module cost include the costs of frame, the mounting of the cell, the cabling, and of course the solar cell itself[25]. For concentrated PV systems the 2-axis solar tracker and optics are also included into the module price. In the end the module is priced by $\$/W_p$ or dollars per peak power. The module price does change over time and on average for the past 35 years every time cumulative production has doubled the price of the solar cell modules has decreased by 23%[26]. The BOS costs are often separated into power-related BOS and area-related BOS. Area related BOS costs include installation labor, wiring, hardware, and so on and can be considered in $\$/m^2$. In 2005 the typical area-related BOS was $\$82/m^2$ which accounts for almost 40% of the cost of the entire solar power plant. All of these factors lead to a levelized cost of electricity (LCOE), that is the expected lifetime cost of the system divided by the lifetime power output, as shown in figure 5.

We can also estimate the energy payback of such systems. This is when the amount of energy put into the system is equal to the amount of energy the system produces.

In Germany, for example, where there are generous subsidies for renewable energy, but the climate and latitude are not favorable for solar power the energy payback for a solar power plant is approximately 2.5 years[26]. In Sicily where it is much sunnier a p-Si power plant can reach it's energy payback in 1 year. If, on average, the plant lasts 20 years that means that the solar power plant in Sicily will produce 20× more power than was used to make it[26]. Furthermore, the operations and maintenance costs, not to mention fuel costs, of photovoltaic systems are low compared to other traditional methods of electricity production[27].

This being said, figure 5 makes it clear that, at least for the foreseeable future, solar power is not a "silver bullet" solution to the issue of clean and inexpensive electricity. Instead terrestrial solar power will be one of many solutions deployed to provide electricity to an area depending on its location, and climate. However, as in most economic topics, unforeseeable events, like changes to the price of coal or oil or public policy on global warming, as well as technological advancements will surely tip the economic balance towards or away from solar power. Thus a diverse application of energy technologies is employed including solar, wind, and biomass power, as well as more traditional methods like coal and natural gas.

1.3.2 Single Junction Solar Cells

Historically Si has been the primary choice for single junction solar cells[22, 26]. Si has many qualities that lend itself to use as a solar cell. Firstly it is chemically abundant, and secondly it has a band gap energy of 1.12 eV which is close to the optimal band gap for a single junction solar cell[28]. Furthermore the use of Si in other areas of microelectronics has led to the development of processing standards and driven down the cost of fabricating Si based devices further further encouraging it's use in photovoltaics. In fact according to the Fraunhofer institute Si based photovoltaics accounted for 93% of total solar cell production in 2015[26]. Other

thin film technologies like CdS or CdTe rely on the fact that very little material is necessary for producing a solar cell, further driving down costs. At the lowest end of the cost-spectrum lie emerging PV technologies like organic solar cells and perovskite materials. Each of these avenues for affordable, terrestrial photovoltaics remains an active area of research and each one has its own benefits as well as its challenges.

1.3.2.1 Crystalline Silicon Solar Cells

Monocrystalline Si solar cells are the most expensive to manufacture because they require slow and careful manufacturing to produce[24]. To begin the cells are typically formed using the Czochralski growth method in which a melt of liquid Si is maintained with a single-crystal seed dipped into the melt[29]. The seed is rotated so as to maintain uniformity and slowly drawn from the melt. The seed acts as a template for crystal growth and the Si forms as the crystal cools as a result of being drawn from the melt. The rate at which the seed is drawn from the melt will result in different diameters of crystal ingots being formed[29]. The resulting ingots are then polished to a uniform diameter and cut to form wafers. It is not uncommon to use the float zone method to produce monocrystalline Si wafers also[30].

The typical fabrication process then utilize anisotropic etching to pattern the surface in an inverted pyramidal structure as described by Campbell and Green[31]. This increases the optical thickness of the solar cell by promoting internal light reflections[31, 32]. The top surface is then doped using dopant diffusion or ion implantation[32]. The front side of the structure is passivated using dielectrics like atomic layer deposition (ALD) formed Al_2O_3 and SiN_x[32, 30]. These dielectrics serve the dual purposes of reducing locations for surface recombinations as well as forming an anti-reflective coating. This high-quality electrical passivation lowering the surface recombination is what is known as a "passivated emitter" configuration. Photolithography and chemical etching can be used to open the dielectric to place

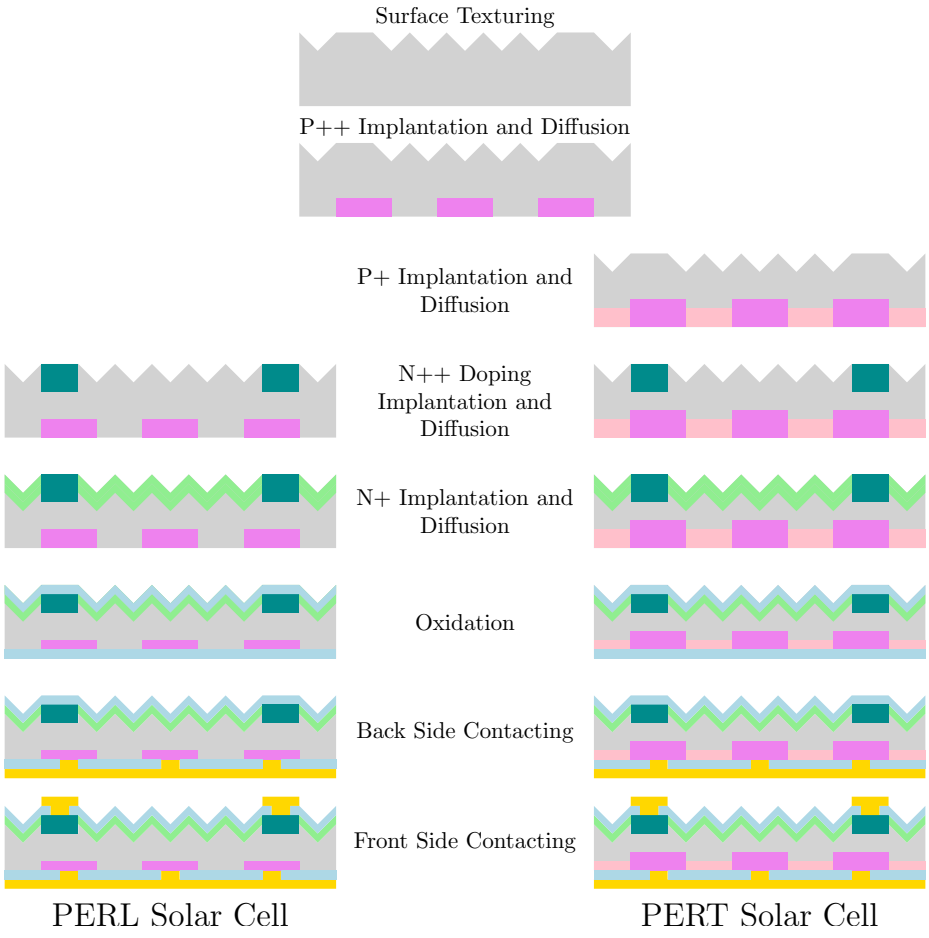

Figure 6: Fabrication of PERL and PERT Solar Cells

the top contact grid. Screen printed contacts are the cheapest, but come at a cost to the efficiency of the solar cell due to shadowing effects[30]. Buried contact based on laser grooved structures have been shown to improve the efficiency of the solar cells, but add complexity to the process[33, 34, 24]. It is typically to utilize electroplated surface contacts as a compromise between the losses of screen printed contacts and the buried contact design[30]. Attention must be paid to the bottom of the solar cell as well. Depending on the resistivity of the solar cell either a totally diffused or locally diffused design is preferred. In higher resistivity cells the totally diffused design is favored where a light dopant concentration is formed across the entire bottom of the cell to prevent current crowding around the higher doped areas near the contacts[30]. In the locally diffused design a "PassDop" process is preferred where the dielectric passivation is opened on the back side of the solar cell and dopants allowed to diffuse through the openings[32]. In both configurations the rear metal contact is formed on the entire back surface. This creates a mirror to increase the optical path for any light that either wasn't absorbed by the solar cell or light that has been emitted from radiative cooling. The contact also completes the electrical circuit at the points where the cell is highly doped and the oxide is open. Schematics of the fabrication of the passivated emitter, rear local diffusion (PERL) and passivated emitter, rear total diffusion (PERT) solar cell designs are shown in figure 6.

1.3.2.2 Polycrystalline Silicon Solar Cells

The processes for manufacturing multicrystalline or polycrystalline Si solar cells require less stringent tolerances than those used to make monocrystalline Si, and are therefore cheaper[24]. Like monocrystalline Si, polycrystalline Si is also grown from a melt, however the material is allowed to solidify without the presence of a seed crystal resulting in the polycrystalline structure. Typically the crucible containing molten Si is allowed to cool slowly from the bottom resulting in a slab of polycrystalline Si which

is later cut into bricks and sliced into wafers. The primary issue with polycrystalline Si solar cells is that they have poorer current-voltage characteristics as defined by the dark current and open circuit voltage[22, 35]. These effect arise from band bending at the grain boundaries due to strained crystal bonds. In addition dangling crystal bonds at the boundaries result manifest as both a short circuit path reducing the shunt resistance as well as a recombination center. This adversely effects the power extracted from the solar cell. In order to avoid recombination losses at the grain boundaries relatively large ($\approx$ 1 mm^2) polysilicon grains are preferred[35]. Despite these challenges to efficiency with respect to monocrystalline silicon, the reduction in cost and the long lifetime of polycrystalline solar cells have resulted in polycrystalline solar cells accounting for 68% of total photovoltaic production in 2015[26].

1.3.2.3 Thin Film Solar Cells

There are large variety of materials and device designs that fall into the category of thin film solar cells. The most prominent material systems that fall into this category are amorphous silicon, cadmium telluride (CdTe), copper indium gallium selenide (CIGS), and gallium arsenide (GaAs). These technologies have some attractive qualities, like their potential for high efficiencies, flexibility allowing for so called roll-to-roll processing, but they also have their drawbacks and according to the annual report on photovoltaics published by the Fraunhofer Institute thin-film technologies accounted for 8% of total photovoltaic production in 2015[26].

Amorphous Silicon

Amorphous silicon (a-Si) can, in principle, be made more cost effectively than polycrystalline silicon[24]. This comes at a cost of solar cell efficiency, however. The lack of long-range structure results in a high defect density inserting traps within the energy band gap of the material. These traps make the formation of a pn junction

in amorphous silicon an impossibility. Furthermore the traps prevent current flow resulting in poor electrical performance of the solar cells[24]. The addition of hydrogen into the a-Si can saturate the traps and lead to an increase of electrical performance. The addition of hydrogen also leads to an increase of the band gap energy from 1.1 eV to 1.7 eV[36, 37]. However there is a degradation of the a-Si that occurs under long-term exposure to light. This Staebler-Wronski effect is caused by energetic light creating dangling bonds within the material that act as recombination centers[38]. This means that the lifetime of the cell is shorter than those made of polycrystalline and monocrystalline Si[36, 37]. of Unlike mono- and polycrystalline silicon a-Si is deposited as a very thin film meaning that it uses very little material to create a solar cell. This is an advantage due to the high cost of monocrystalline si ingots [26]. With these advances a-Si has advanced to having a 14% efficiency[39].

Cadmium Telluride

Cadmium Telluride (CdTe) Cells are actually a heterojunction solar cell based on stacking n-type cadmium sulfide (CdS) and p-type CdTe. The resulting structure has a band gap energy of 1.5 eV which is very close to the ideal band gap of 1.3 eV required for maximum power extraction from the solar spectrum with a single junction. In fact the CdTe solar cells have been reported to have a 22.1% efficiency[39]. One of the factors limiting CdTe solar cells is the availability and toxcicity of the raw materials, namely cadmium and tellurium. Both Cd and Te are toxic and Cd is classified as a hazardous substance and thus requires special handling. Cd is generally obtained as a waste by product from the mining and refining of Zn, and therefore can be purchased relatively cheaply from mining companies who would otherwise store it and dispose of it as hazardous waste. Tellurium, on the other hand, is a rare metalloid occurring on earth in about the same abundance as platinum. Our supply of Te comes almost exclusively as a by-product of copper refining. While new supplies have been found

in China, Mexico, and Sweden as well as on undersea ridges CdTe photovoltaics currently use a large percentage of the worlds production of Te. In 2007 the United States Geological Survey estimated global Te production in 2007 to be 135 metric tons[40]. To produce enough CdTe solar cells to obtain 1 gigawatt of power would require 93 metric tons of Te[41]. For reference the United States used approximately 4000 TWh of electricity in 2012, and so a 1 GW CdTe plant would be able to power the US for 9 milliseconds and yet would use 70% of the worlds yearly Te supply to manufacture[41]. Fortunately there are proposals to mine end-of-life CdTe modules to recycle the Te that would allow CdTe solar cell production independent of the mining of Te by 2038[42].

Even with the high cost of tellurium the overall cost of a CdTe solar cell is low. Depending on the design of the CdTe module and whether materials can be purchased at a bulk cost the cost of CdTe modules is estimated to be less than \$10 USD/m^2 which is very competitive compared with monocrystalline Si[43, 44].

Copper Indium Gallium Selenide

Copper indium gallium selenide (CIGS) is a solid solution of the semiconductors copper indium selenide (CIS) and copper gallium selenide (CGS) and so can be represented with the chemical formula $CuIn_xGa_{1-x}Se_2$. By varying the relative concentrations of In and Ga the band gap energy can be tuned from 1 eV to 1.7 eV, making it an interesting candidate for high efficiency single junction photovoltaics. To date the best CIGS solar cell has an efficiency of 22.6%.

CIGS solar cells are formed from the bottom up. First, the back contact, typically molybdenum, is sputtered onto a substrate, typically glass[45]. The surface morphology and adhesion of the contact to the glass are important for the following CIGS deposition. The CIGS deposition typically is either done using a technique like co-evaporation where the Se is introduced gradually throughout the entire process or in a

multistep process where first the metal layers are deposited followed by chalgenation using either H_2Se gas or elemental Se [45]. Following the CIGS absorber layer deposition there is a buffer layer, often CdS, deposited followed by the top contacts[45]. The top contacts are normally some combination of transparent conductors (ZnO or ITO) and metal grids of Al or Ni/Al. Finally, antireflection coatings of materials like MgF_2 are added to complete the structure[45]. Of the two methods of absorber region formation mentioned the best results come from the single step process using co-evaporation[46, 45].

The co-evaporation technique is a multistage process in which the metal fluxes, temperature, and metal:Se ratio are controlled to obtain the appropriate film. Often this method is performed in a molecular beam epitaxy system (MBE)[45]. The metal sources are evaporated from effusion cells in the presence of H_2Se gas. First a layer of InGaSe is formed at a relatively low temperature (300-350° C). Then Cu is deposited at an elevated temperature which will mix with the InGaSe layer to form a uniform, Cu-rich CIGS layer. The Cu supply is then cut off and the amount of In and Ga increased to form the top layer. The top layer is Cu-deficient and forms an ordered vacancy compound (OVC) at the surface that is very beneficial for solar cell performance[46, 45].

The co-evaporation technique produces the highest quality absorber region, but is slower than the metal deposition-selenization process[45]. In these methods the metal precursors are deposited in stacks either by sputtering, evaporation, or electrochemical deposition. These process are faster, can be scaled up for higher throughput, and occur at a lower temperature than co-evaporation and are therefore more economical. Chalcogenation then occurs at approximately 400° C[45]. The formation rates of CIS and CGS are not the same and as a result the films may not be homogeneously mixed and may separated CGS and CIS phases that degraded performance. However, like most processes for photovoltaics the degradation in performance must be weighed

against cost savings and in this case the cost savings lead to economically viable solar cells.

Gallium Arsenide

Gallium arsenide, like GaN is a III-V semiconductor, and also like GaN it is most frequently grown by MOCVD. For solar cell production an epitaxial lift-off technique pioneered by Konagai *et al.* is preferred because the GaAs template may be reused for future MOCVD growths cutting costs[47]. In this process an AlAs sacrificial layer is grown followed by the GaAs/InGaAsP active regions[47, 11]. Alta Devices has developed a process in which the back contact is then formed on the surface of the substrate[10]. This back contact often acts as a mirror to promote photon absorption. A backing material is then bonded to the back contact and the AlAs is selectively wet etched in hydrofluoric acid[10, 11]. The resulting cell can then be flipped and the front contact layer and antireflective layers formed[11].

Of all the solar cells discussed so far, GaAs cells show the highest performance of between 27 and 28% efficiency. These cells are also the most costly due to the energy intensive MOCVD techniques used to make them. Also the cells are fragile and there is a decrease in the yield due to failures during processing. As such GaAs solar cells are rarely used as a single junction solar cell, especially for unconcentrated photovoltaics. Instead GaAs is more frequently used a component of multijunction solar cells used in concentrated photovoltaics or space applications.

1.3.2.4 Emerging Solar Cells (Organic, Perovskite, etc)

Emerging solar cell technologies are those technologies that have yet to make it to mass production, but have the potential to impact solar energy production in the future. Three technologies in particular are heavily researched and those are organic solar cells, dye sensitized solar cells, and perovskite solar cells. Schematics of these devices are shown in figure 7. A brief outline of how these solar cells are formed

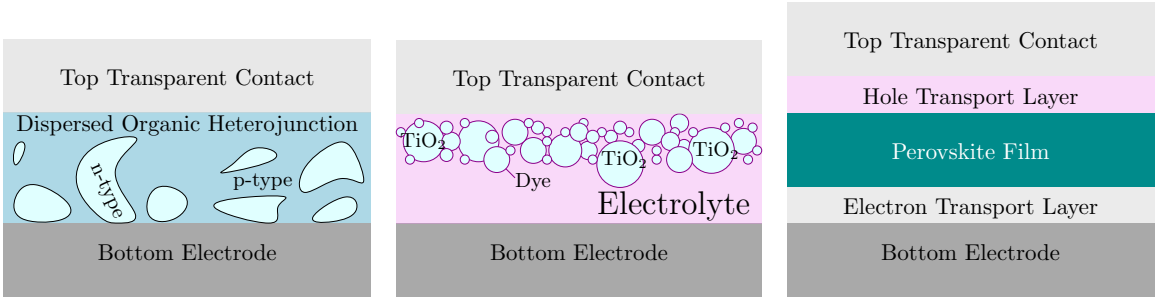

(a) Organic Solar Cell Schematic (b) Dye Sensitized Solar Cell Schematic (c) Perovskite Solar Cell Schematic

Figure 7: Schematic of the an organic, dye sensitized, and perovskite solar cells

and how they operate is given below. In general the processes used for fabrication, methods of operation, and challenges associated with emerging PV technologies are different than those facing InGaN solar cells and so their discussion here is brief.

Organic solar cells use organic conductive compounds, like certain polymers, as the active region of the solar cell. The materials are deposited either by evaporation or by organic vapor phase deposition (OVPD). In order to form a pn-junction the organic compound is either sandwiched between two metals with different work functions, or different organic materials can be used to form heterojunctions. Often with heterojunction organic solar cells the uniformity of the material is key in improving external quantum efficiency. They key challenges facing organic solar cells are their poor efficiencies and natural degradation of the solar cell occurs at a faster rate than with inorgainc cells. The primary advantage of organic solar cells is that the costs for manufacturing them are extremely low. While organic PV has not caught on, their counterpart, organic LEDs are wildly used.

Dye sensitized solar cells (DSSCs) were first inspired by research on the photosynthesis of plants. They are made by sandwiching a junction between a mesoporus conducting oxide layer, typically TiO_2 micro- or nanospheres that have been sintered, and an electrolyte solution between two transparent contacts. The conducting oxide layer is exposed to a charge transfer dye that can absorb light. This dye coats the

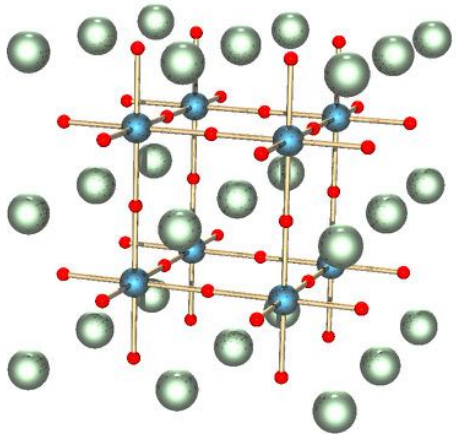

Figure 8: Example of a perovskite crystal structure. Here the blue sphere represent small metallics cation atoms, the red spheres oxygen atoms, and the green tinted spheres larger metallics cations[9]

exposed surfaces of the oxide and forms the absorbing region of the solar cell. Solar exposure excites an electron-hole pair in the dye. The electron can then be collected in the oxide matrix. The conductive pathways through the sintered oxide matrix are formed stochastically and depend on the size of the oxide nano-particles. The larger the particles the more likely there is a conductive path to reach the anode, however this is a tradeoff with the short-circuit current as the smaller the nano-particles the more surface area they have and the effective size of the absorber increases as the surface of theses nano-particles is coated with the dye. After the electrons move into the oxide structure there is an excess hole left in the dye and the electrolyte serves to complete the electrical circuit by reducing the dye. Some challenges associated with DSSCs are the low efficiency due to the poor carrier collection, longevity as the dyes degrade with use and in the presence of the electrolyte, as well as toxicity of the electrolyte solution necessitating additional care in the solar cell production, packaging, care, and disposal[48].

Perovskite solar cells have attracted attention recently as there has been a jump in their efficiency from 14% to over 22% in the past three years. Perovskite solar cells developed out of dye sensitized solar cells where the perovskite material was used on

top of a mesoporous TiO_2 layer[49]. Later it was determined that the mesoporous layer that is critical to DSSCs was not required opening the avenue for research into what is now perovskite solar cells[50]. Perovskite is a solution-processable semiconductor material, which means that the constituents of the film can be dissolved into a liquid or vapor solution, transported to a substrate, and then the solvent can be removed to form the perovskite film. A perovskite is any film that has an ABX_3 structure like $CH_3NH_3PbX_3$, where X can be a halogen such as I, Br, or Cl. This structure is a cubic crystal as shown in figure 8. The film can be formed by spin coating the dissolved components onto a substrate, typically an electron transport layer like ZnO, followed by removing the solvent by either annealing or exposure to a diethyl ether solvent that will selectively remove the first solvent and leave the perovskite film behind. Following the perovskite film formation a hole transport layer like copper iodide is deposited by evaporation. Finally the top contact is made by using metal or a conducting glass like ITO. The simplicity and low cost of the fabrication of perovskite solar cells, and the relatively high efficiencies (up to 22.1% in 2016) makes it attractive for next-generation photovoltaics. However there is a continued problem of the film stability. Exposure to sun light and oxygen tend to degrade the perovskite materials so the cells are very short lived.

1.3.3 Constraints on Solar Cell Efficiency, The Shockley Queisser Limit

Solar cell efficiency is defined as the electrical power obtained from a device divided by the optical power going into it: $\eta = P_{out}/P_{in} = (I \times V)/1000\text{W}$. Both the current and voltage from a solar cell depend on the band gap energy of the semiconductor, thus there is an optimal value for this energy to maximize solar cell efficiency. The first formulation of the optimal bandgap energy as well as the theoretical maximum efficiency of a solar cell was determined by Shockley and Queisser in their 1961 paper. In this paper the following assumptions were made: that a all light with an energy

greater than or equal to the band gap energy will be absorbed, each absorbed photon results in one electron hole pair being generated, the only method of loss in the solar cell is via radiative recombination, and that the cell behaves like an ideal diode and thus can be modeled using the ideal diode equation. There are several more methods of loss limiting the performance of physical solar cells including non-radiative recombination (Auger recombination, trap assisted recombination, *etc.*), but the Shockley and Queisser ignore them in order to find the best possible efficiency for a certain solar cell. This formulation is outlined below and then we extend the formulation using experimentally measured solar spectra.

To begin, we consider that the sun is a spherical blackbody with a diameter of 1.39 million km, a distance to the earth of 149 million km, and temperature of 6000 K. This is a rather good approximation of the solar spectrum in space, but due to scattering of the sun light in the atmosphere (off of air, water vapor, and dust primarily) the terrestrial spectrum is slightly different. Due to the curvature of the earth, and the earth's angle of inclination to the sun the amount of sunlight scattered in the atmosphere changes based on location and season. It is convenient (and typical) to use a normalized spectra for sunlight that has passed through 1.5 thicknesses of atmosphere (called "air mass 1.5," or simply AM1.5). This spectra has been measured and is freely available from http://rredc.nrel.gov/solar/spectra/am1.5/. Both the blackbody approximation and the spectral irradiance for AM1.5 are shown in figure 1.

It is convenient to convert the solar spectral irradiance ($\frac{dE}{d\lambda}$) from figure 1 from units of W per m^2 per nm to the number of photons per m^2 per nm ($\frac{dN}{d\lambda}$).

$$E_{photon} = h\nu \tag{2}$$

$$\begin{aligned} \frac{dN}{d\lambda} &= \frac{dE/d\lambda}{E_{photon}} \\ &= h\frac{c}{\lambda} \\ \implies \frac{dN}{d\lambda} &= \frac{dE/d\lambda}{h\nu} \\ &= \frac{dE/d\lambda}{hc/\lambda} \end{aligned} \tag{3}$$

Where eqn. 1 is the Planck relation, and eqn. 2 converts from energy at a particular wavelength to the number of photons of that wavelength. With $\frac{dN}{d\lambda}$ it is fairly trivial to determine the number of photons absorbed/unit area (assuming that all photons above the energy of the bandgap, E_g, are absorbed):

$$N/A = \int_0^{hc/E_g} \frac{dN}{d\lambda} d\lambda \tag{4}$$

Although it is more common to present the number of photons as a function of energy, $F_{si}(E_g)/A = \int_{E_g}^{\infty} \frac{dN}{dE} dE$, as shown in figure 9[51]:

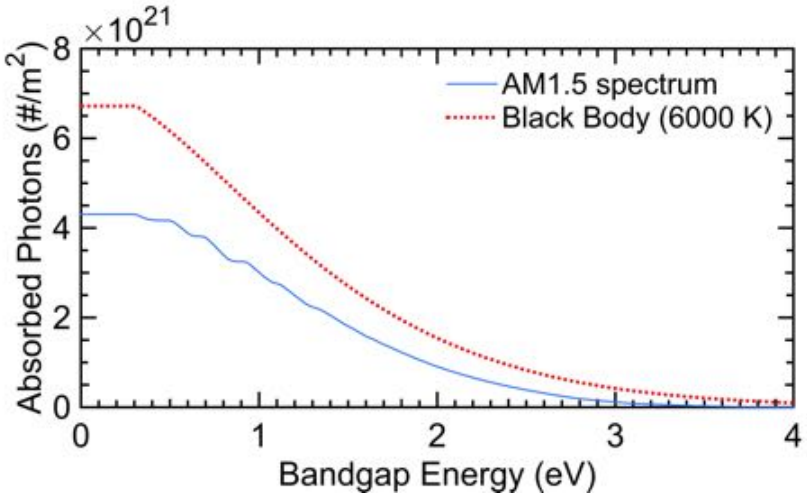

Figure 9: Number of photons absorbed as a function of energy, $N(E_g)$

To account for radiative recombination we can count the number of photons emitted by the semiconductor. To do this we simply consider the material to be a blackbody that follows Planck's distribution:

$$N(\nu, T) = \frac{2\pi}{c^2} \frac{\nu^2}{\exp(h\nu/kT) - 1} \tag{5}$$

Where ν is the frequency, c is the speed of light, k is Boltzmann's constant, and T is the temperature of the blackbody. We assume that for each photon emitted one electron-hole pair is destroyed meaning the radiative recombination is given by:

$$F_{0i}/A = \frac{4\pi}{c^2} \int_{E_g/h}^{\infty} \frac{\nu^2}{\exp(h\nu/kT) - 1} d\nu \tag{6}$$

Using this we can calculate the total current by subtracting the number of electrons that recombine from those generated by illumination.

$$I_{si} = q(F_{si} - F_{0i}) \tag{7}$$

From the recombination we can determine the reverse saturation current:

$$I_{0i} = qF_{0i} \tag{8}$$

Apply this value to the diode equation we obtain:

$$\begin{aligned} I_i(V) &= I_{0i}(\exp(qV_i/kT) - 1) - I_{si} && (9) \\ &= qF_{0i}(\exp(qV_i/kT) - 1) - q(F_{si} - F_{0i}) \\ &= qF_{0i}\exp(qV_i/kT) - qF_{0i} - qF_{si} + qF_{0i} \\ &= qF_{0i}\exp(qV_i/kT) - qF_{si} && (10) \end{aligned}$$

From figure 9 we can come to the conclusion that for a solar cell with a particular band gap energy many photons may not have an energy large enough to be absorbed and the solar cell will be transparent for these photons. This gives rise to an interesting engineering solution: multi-junction solar cells. Solar cells can be stacked so that

the cells with the largest band gap are on the top. These absorb the highest energy photons while the lower energy photons pass through the cell to be absorbed by a lower band gap solar cell later on. We can include solar cell design into the formulation of the Shockley-Queisser limit with no loss of generality. We do that here by considering the maximum power point for a multi-junction solar cell with n junctions:

$$P_m = \sum_{i=1}^{n} V_{mi} I_{mi} \tag{11}$$

$$\frac{dP_m}{dV} = 0$$

$$\implies 0 = q\frac{d}{dV_i}\left(\sum_{i=1}^{n} V_{mi} F_{0i} \exp(qV_{mi}/kT) - V_{mi} F_{si}\right) \tag{12}$$

If we let $x = qV_{mi}/kT$, then:

$$\begin{aligned} 0 &= q/kT\left(kT/q\frac{d}{dx}\sum_{i=1}^{n} xF_{0i}\exp(x) - xF_{si}\right) \\ &= F_{0i}\exp(x) + xF_{0i}\exp(x) - F_{si} \\ &= F_{0i}\exp(x)\,(x+1) - F_{si} \\ \therefore\ &\exp(x)(x+1) - F_{si}/F_{0i} = 0 \end{aligned} \tag{13}$$

This provides us with a system of equations to solve for each F_{si}/F_{0i}, after which we can easily calculate the voltage where each cell is operating most efficiently, V_{mi}, and using eqns. 9 and 10 respectively we can calculate the max current and power of the cell. The efficiency is easily defined as:

$$\eta = P_m/P_{in} \tag{14}$$

Where P_{in} is the power of the light incident on the cell. This is found by integrating the spectral irradiance over the wavelength in figure 1. Doing so using the trapezoidal rule we find that approximately 1003 W of power fall on the earth per m^2 at AM1.5. This is unsurprising as the NREL data is normalized to 1000 W/m^2. We can take

these results and use them to make predictions as to what the optimal band gap energy would be for solar cells of various junctions and compare our results with those published in the literature. The results for the short circuit current density, open circuit voltage and theoretical maximum efficiency as a function of band gap energy produced with this model for a single junction solar cell are shown in figure 10.

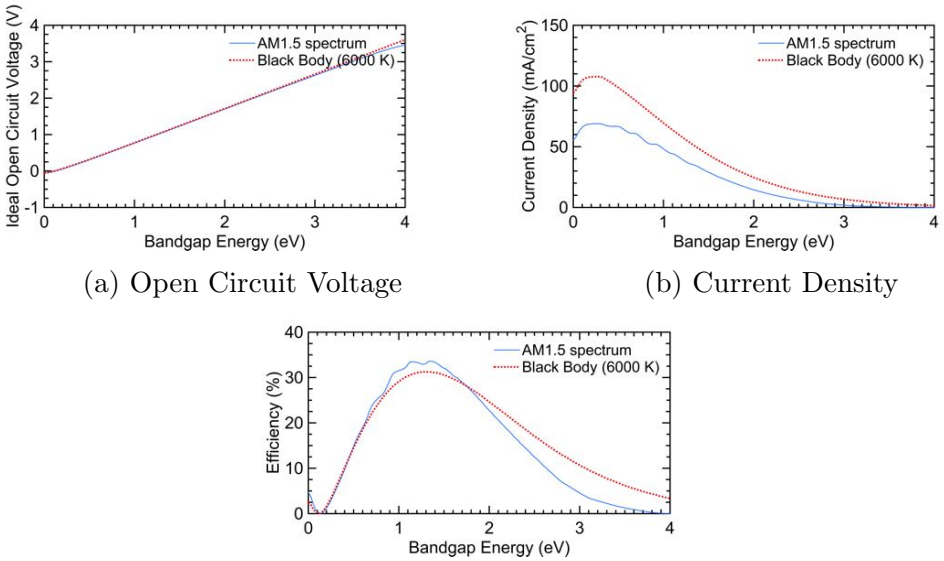

(a) Open Circuit Voltage

(b) Current Density

(c) Single Cell Efficiency

Figure 10: The (a) open circuit voltage, (b) current density, and (c) efficiency of an ideal single solar cell as a function of bandgap energy. This is in good agreement with the Shockley Queisser results.

These results are in very good agreement with the results from Shockley and Queisser and Henry for the ideal J_{sc}, V_{oc}, efficiency, and E_g that provides that efficiency. Further validation was performed using the analysis of Alexis de Vos. He too used the 6000 K approximation of the solar spectrum. Additionally, in his multijunction solar cell formulation he included segments of the spectra absorbed by each solar cell that were emitted by neighboring cells. Adding this electroluminescent spectra to the model changes the overall efficiency of a 2 cell tandem structure by 0.1%. And so it was neglected in our model. Using de Vos's values for optimal bandgap

energies we compare our model with his:

Table 1: Comparison of the modeled efficiency for 1, 2, 3, and 4 junction solar cells with A. de Vos's published results

n	η_{model} (%)	η_{Vos} (%)	$E_{g1}(eV)$	$E_{g2}(eV)$	$E_{g3}(eV)$	$E_{g4}(eV)$
1	31	30	1.3	-	-	-
2	43	42	1.9	1.0	-	-
3	50	49	2.3	1.4	0.8	-
4	53	53	2.6	1.8	1.2	0.8

The difference in the efficiencies between the de Vos result and our model is very small and can be accounted for because we use different solar spectra and because we neglected re-absorption of thermally emitted photons.

In conclusion the maximum theoretical solar cell efficiency of 30% is obtained using a semiconductor with a junction of 1.3 eV. Furthermore, what is of particular interest is that for a 2 junction or tandem solar cell the maximum theoretical efficiency raises to 42% using semiconductors with band gaps of 1 and 1.9 eV. Si has a band gap energy of 1.12 eV, and that the possible band gap energies of InGaN range from 0.64 eV to 3.4 eV. Thus a Si solar cell is close to the optimal for a single junction solar cell, or a combination of InGaN + Si will be close to optimal for a tandem solar cell. While the InGaN material systems spans this entire band gap energy range for four junction solar cells there are additional challenges in stacking more and more complex InGaN solar cells. Furthermore, The combination of Si and InGaN tandem solar cell has the promise of increasing the efficiency of the solar cell while maintaining a low over-all cost for the device.

1.3.4 Multijunction Solar Cells

The primary loss of power in single junction solar cells is from inefficient extraction of the solar spectrum. Either the energy of the sun is smaller than the band gap energy of the solar cell, $E_g > h\nu$, and the light passes through the cell without being

absorbed, or the light has an energy far above the band gap and the excess energy is wasted as heat, $E_g << h\nu$. Multijunction solar cells hope to counter this loss by utilizing more than one material with more than one band gap energy to collect the light more efficiently.

1.3.4.1 Solar Cells with Two Junctions

From the works like that of Shockley, Queisser, de Vos and Henry we can see that the ideal band gap energies for solar 2 junction solar cells are 1.9 and 1.0 eV[28, 51]. Common materials for 2 junction solar cells and their maximum theoretical efficiencies are shown in table 2. These values have been calculated based on the a model derived from GaAs-Ge junctions using carrier mobilities and lifetimes that were appropriate for the date of the publication, but this report has since been updated and therefore the maximum attainable efficiencies can be revised upwards in some cases. They are included here to demonstrate the potential increase in efficiency of two junction solar cells[52, 1, 53]. The primary materials used for two junction solar cells remain AlGaAs-Si and GaAs-InGaP with the world record, unconcentrated double junction solar cell efficiency of 31.6% currently held by Alta Devices[54]. This record was achieved using by using an epitaxial liftoff technique by growing GaAs and InGaP on AlAs[10, 11]. The result was fabricated by MOCVD in an inverted geometry so that first the AlAs layer was grown followed by the upper InGaP layer was grown and then the GaAs layer[10, 11]. The back-side contact was formed on the sample and the resulting structure was then released by dissolving the AlAs in HF allowing for a thin and flexible solar cell structure with back-side contacts[10, 11]. All that remains for operation solar cells is the formation of the front-contact grid and addition of anti-reflective coatings resulting the the structure seen in figure 11.

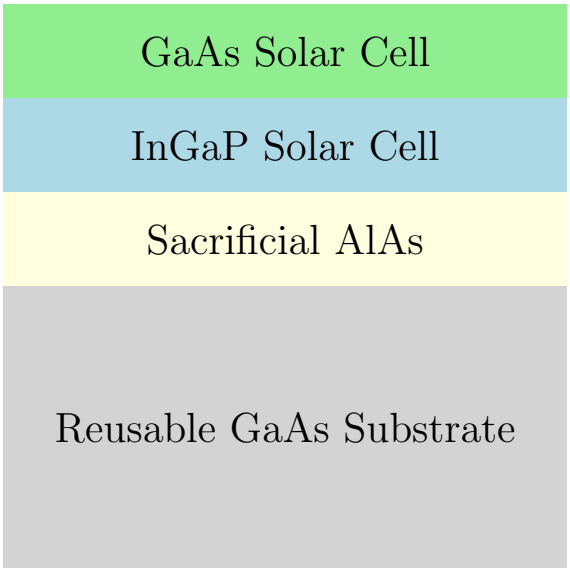

(a) Inverted Geometry Solar Cell Growth

(b) Deposition of Back Contact

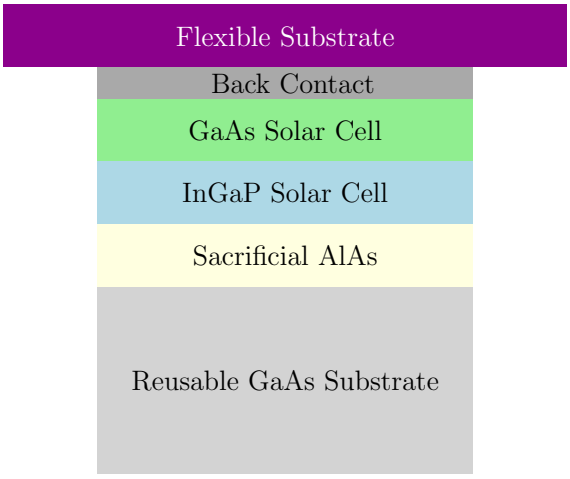

(c) Attachment of Flexible Substrate

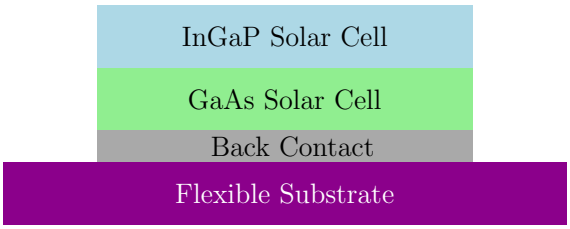

(d) Dissolution of AlAs in HF and Removal of GaAs Substrate

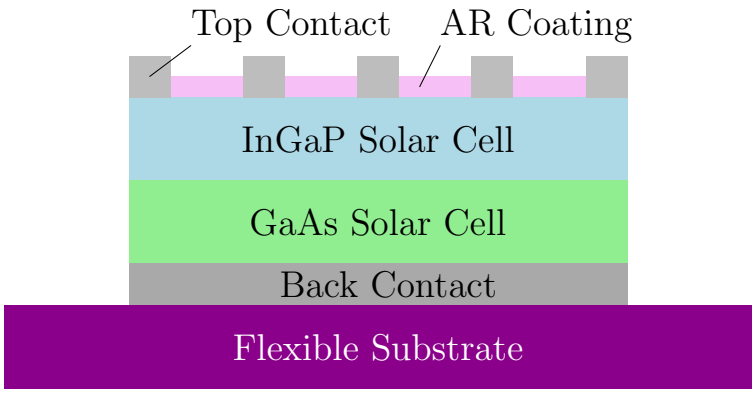

(e) Top Side Processing

Figure 11: Schematic of the process for fabricating the world-recording holding dual junction solar cell fabricated by Alta Devices [10, 11]

Table 2: Maximum Attainable Efficiency for p-n and n-p heterojunction solar cells in 1969 [1]

Materials	p-type Carrier Concentration (cm^{-3})	n-type Carrier Concentration (cm^{-3})	1969-Maximum Attainable Efficiency η_{max} (%)
p-n type			
Si-GaAs	10^{17}	10^{16}	28
Si-GaP	10^{16}	10^{17}	24
InP-GaAs	10^{16}	10^{17}	27
InP-GaP	10^{16}	10^{17}	25
GaAs-GaP	10^{16}	10^{17}	21
n-p type			
Si-GaAs	10^{16}	10^{17}	24
Si-GaP	10^{16}	10^{17}	25
InP-GaAs	10^{16}	10^{17}	30
InP-GaP	10^{16}	10^{17}	30
GaAs-GaP	10^{16}	10^{17}	28

1.3.4.2 Solar Cells with more than 2 junctions

To obtain highly efficient solar cell it is not enough to utilize just one type of semiconductor material. Instead researchers since 1955 have been proposing to use multiple junctions to convert different parts of the spectrum into electricity [55]. By adding more and more junctions a theoretical maximum efficiency of 69% can be obtained, but such an infinitely graded solar cell is at least impractical if not impossible with todays material systems [28]. According to the United States National Renewable Energy Laboratory (NREL) the highest ever reported unconcentrated solar cell efficiency is 38.8%, and has been achieved using a 5 junction solar cell approach by Boeing Spectrolab as can bee seen in figure **??** [56]. These cells require complex and low yield processing steps like wafer bonding, expensive semiconductor materials such as InP and GaAs, and as the cells become thicker it becomes more difficult to cool them and thus require specialize heat sinks. As a result, three, four, and five junction solar cells are for the time being prohibitively expensive for terrestrial use. In their

report Spectrolab explicitly states that such complex solar cells are, by and large, for use in outer space where the limited payload masses preclude using large, heavy solar cell arrays [56]. On earth there is a lot more competition for electricity and so the solar cells must be priced accordingly. Therefore the bulk of solar cells for terrestrial use consists of single and double junction devices.

1.3.4.3 Multijunction solar cell module design

Multijunction solar cell module design can be simplified to either two-terminal series cells, independently contacted vertical cells, or filter-reflector configurations[55, 12]. These aspects of these various designs can be seen in figure 12. The two terminal design is the most simple to operate, but requires the use of tunnel junctions between the various absorber regions. These tunnel junctions are necessary so as to not form reverse junctions within the solar cell. What's more is that the tunnel junctions must have a low resistance and be transparent to the light meant to be absorbed in the lower absorber regions. Furthermore, the thicknesses and band gaps of the absorber regions must be carefully matched so that no region in particular is limiting the performance of the solar cell (current matching). On first glance the independently contacted vertical approach may seem very similar to the two terminal approach, but it suffers from different limiting criteria. Firstly, the contacts on the top cell will necessarily cast a shadow on the bottom cell. One way to minimize the effect of contact shadowing is to align the contacts of the top cell with the top contact of the bottom cell. This is approach can be employed with varying degrees of effectiveness depending on the sheet resistance of the semiconductors involved. For a solar cell the most effective contact pitch is one in which the power lost due to shadowing are equal to the power lost to resistive effects[24, 57]. Depending on the semiconductors used this loss can also be overcome by using transparent or semi-transparent contacts like Indium Tin Oxide (ITO). In practice, however, the shadow loss of the contacts

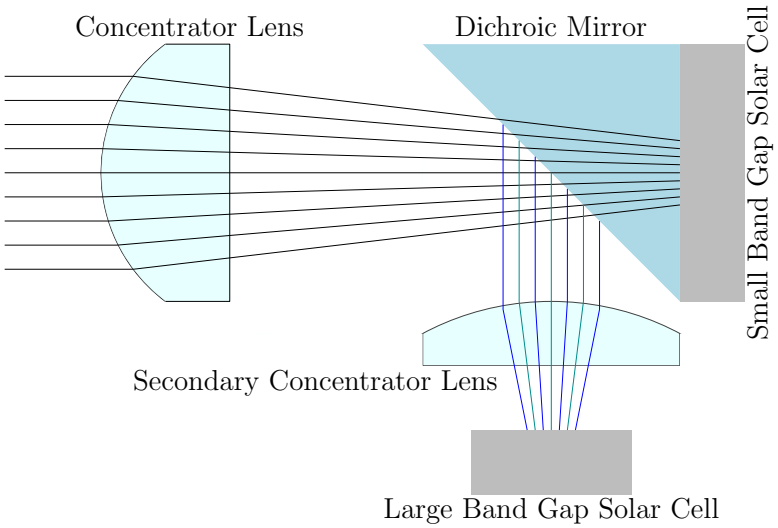

Figure 12: High Efficiency Solar Cell Module Design[12]

if often overlooked or ignored as a necessary evil and rightfully so because often they account for only a small fraction of power lost in the solar cell[24]. A further concern for independently contacted vertical solar cells is surface reflections from stacked solar cells, but antireflective coatings can be effective at countering this. Filter-reflector devices are most similar to the independently contacted vertical cells in that each cell can operate independently from the others and thus requires neither tunnel junctions nor current matching. The difference is that instead of stacking the cells vertically optics are used to separate the light and distribute it to each junction individually [12]. The performance of this design is therefore dependent also on the the performance of the optics. A major benefit of both the independently contacted vertical and filter-reflector designs is that if the various junctions can be made on different dies and do not have to be combined electrically and optically later. This allows for a flexibility in the semiconductor used and the potential to avoid lattice mismatch in the growth of the semiconductor.

1.4 Conclusions

Photovoltaics have many advantages that lend them to playing a large part in producing renewable and environmentally sustainable energy. Firstly solar energy is the abundance of solar energy. Everyday roughly 6000 times more power reaches the earth surface in the form of sunlight than what is consumed by human activities. Secondly, photovoltaics convert sunlight directly into electricity making it very simple to install with (generally) no moving parts. This means that it can be installed in large scale, centrally by utilities or in a distributed manner on residential commercial roofs. This contrast other methods of harvesting solar power which rely on boiling water or liquefying salt to power mechanical turbines and are only suitable for large-scale utilities.

Photovoltaics is not without it's problems and challenges however. In 1961 Shockley and Queisser formulated the thermodynamic maximum efficiency for a solar cell and crystalline silicon solar cells are nearing this technological limit. New cheaper or higher performing solutions are required in order to make photovoltaics more economical and see them implemented more widely. Researchers have taken up this mantle and shown a variety of solutions from inexpensive organic based solar cells to high performance multijunction cells. As of today there is no standardized solution. However, we believe that using a combination of indium gallium nitride and Si we can achieve a compromise between cost a performance that will fill the economic niche.

CHAPTER II

INDIUM GALLIUM NITRIDE: MATERIAL AND GROWTH

2.1 Why Use Indium Gallium Nitride

Indium Gallium Nitride, or InGaN is predicted to be an excellent material for solar cell applications. Firstly, it has a tunable band gap energy that spans from near UV across nearly the entire visible spectrum allowing it to be utilized in highly efficient single or tandem cell designs. It is a direct band gap material and has a high coefficient of optical absorption. InGaN has a high resistance to irradiation making it it suitable for extraterrestrial applications. InGaN has a relatively high thermal conductivity, temperature resistance, and a high carrier mobility and drift velocity that suggest that it will be a good match for concentrated photovoltaic systems. Lastly the calculated band alignments of n-$In_{0.45}Ga_{0.55}N$/p-Si are should be conducive to low resistance tandem solar cells.

These properties as well as the physical and electrical properties, crystal structure, and the growth of InGaN by a variety of methods are discussed in detail in the following sections. Lastly we will review the challenges associated with the growth and fabrication of InGaN based solar cells as well as discuss the state of the art.

2.2 Indium Gallium Nitride

InGaN is a solid solution of GaN and InN. GaN and InN, as well as BN and AlN, are III-Nitride semiconductors formed by creating a crystal with a group III (IUPAC group 13) metal and nitrogen. The III-Nitride materials system has many unique properties including the possibility of using strained and polarized layers to create

2D electronic devices like high electron mobility transistors, and the ability to tune the band gap energy across a wide array of energies opening the avenues toward optoelectronic devices like light emitting diodes, laser, and solar cells. In order to better comprehend the challenges associated with the production of such devices some background on the crystal structure and properties of the III-Nitride material system are necessary.

2.2.1 Indium Gallium Nitride Crystal Structure

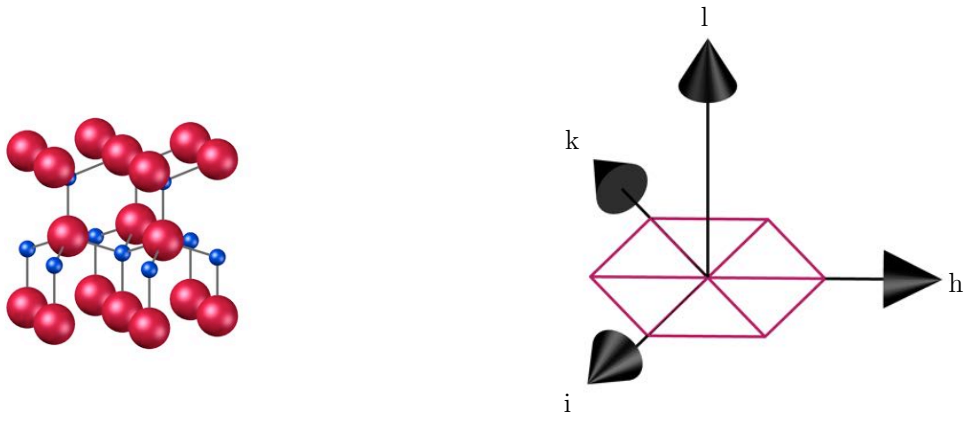

(a) (b)

Figure 13: Schematic representation of a III-Nitride wurtzite crystal. Red spheres represent the group III material and the blue spheres represent nitrogen. (b) description of hexagonal lattice and miller indices.

Both GaN and InN are most stable in a wurtzite crystal structure, which is an interlocking hexagonal crystal lattice where the Ga or In elements make up one hexagonal lattice and the N elements make up the other. Figure 5 (a) illustrates the wurtzite structure of GaN or InGaN. By convention crystal directions and planes in the wurtzite crystal are denoted by the quadruplet (h, k, i, l) instead of the standard (h, k, l) Miller indices. The h, k, and i indices are in plane and 120° from each other, while the l index extends along the crystal's c-axis as shown in figure 5 (b). This

means that the indices are not linearly independent, in fact the extra i index is can be defined in terms of h and k: $i = -(h + k)$. There are two lengths that define the the equilibrium spacing of the crystal lattice and these are denoted as lengths a and c. The crystal lattice spacing along the basal axes is a and the lattice spacing along the vertical axis of the hexagonal prism or c-plane is c.

Furthermore, the wurtzite crystal is symmetric about the [0 0 0 1] (or c axis) direction, but lacks inversion symmetry. In other words the [0 0 0 1] and [0 0 0 $\overline{1}$] directions are not equivalent. The crystalline asymmetry leads to the materials being polar. This polarization is called the spontaneous polarization, $\vec{P}_{\text{sp}}$. Depending on how the crystal is grown the direction of this polarization will either be Ga-faced, pointing opposite of the growth direction as depicted in figure 5 (a), or N-faced and pointing along the growth direction.

When stress is applied to the InGaN crystal it will deform. In the elastic regime this deformation can be approximated by Hooke's law. This assumes that there is a linear relationship between the stress (pressure) and the strain (deformation), and that this can be described by the stiffness of the crystal. As such Hooke's law can be represented using Einstein notation as: $\sigma_{ij} = C_{ijkl}\,\epsilon_{kl}$ where σ_{ij} is the stress tensor, C_{ijkl} is the stiffness tensor and ϵ_{kl} is the deformation vector.

Deformations of the crystal will result in changes of the polarization within the crystal, and *vica versa*. This phenomenon is called the piezoelectric effect. The change in piezoelectric polarization, $P_{\text{pz},i}$, can also be related to the deformation tensor or the stress tensor using the piezoelectric tensor, d_{ij}, by the equation: $P_{\text{pz},i} = d_{ijk}\,\sigma_{jk}$. Thus the total polarization can be calculated as the sum of the spontaneous polarization resulting from the crystal lattice structure and the piezoelectric polarization resulting from a displacement from equilibrium of the crystal lattice: $\vec{P} = \vec{P_{\text{sp}}} + \vec{P_{\text{pz}}}$.

2.2.2 GaN and InN physical properties, and Vegard's Law

InN and GaN each have their own properties and values for quantities like the lattice parameters, stiffness and piezoelectric tensors, band gap energy, and so on. Thus it makes sense that an alloy of the materials will result in an interpolation of these parameters. For many of the parameters a simple linear interpolation of the parameters based on the composition of the alloy is accurate enough to make predictions of the properties of the alloy as done in equation 3. In other cases a quadratic term is added called a bowing parameter to increase the accuracy of the model and the use of these bowing parameters is displayed in equation 4. This type of model for physical parameters based on the relative compositions of the components is referred to as Vegard's Law[58, 59]. Table 3 contains a list of relevant parameters.

$$a_{\mathrm{In}_x\mathrm{Ga}_{(1-x)}\mathrm{N}} = x\, a_{\mathrm{InN}} + (1-x)\, a_{\mathrm{GaN}} \tag{15}$$

$$a_{\mathrm{In}_x\mathrm{Ga}_{(1-x)}\mathrm{N}} = x\, a_{\mathrm{InN}} + (1-x)\, a_{\mathrm{GaN}} - x\,(1-x)\, b_{\mathrm{InGaN}} \tag{16}$$

Table 3: Unstrained lattice parameters for GaN and InN wurtzite crystals [2, 3]

Parameter	Symbol	GaN	InN	b_{InGaN}	Units
Lattice Parameter	a_0	3.189	3.545	–	Å
Lattice Parameter	c_0	5.185	5.703	–	Å
Spontaneous polarization	P_{sp}	-0.029	-0.032	0.037	C/m^2
Elastic constant	C_{11}	390	223	–	GPa
Elastic constant	C_{12}	145	115	–	GPa
Elastic constant	C_{13}	106	92	–	GPa
Elastic constant	C_{33}	398	224	–	GPa
Elastic constant	C_{44}	105	48	–	GPa
Elastic constant	C_{66}	123	141	–	GPa
Piezoelectric coefficient	d_{31}	-0.49	-0.57	–	C/m^2
Piezoelectric coefficient	d_{33}	0.73	0.97	–	C/m^2
Band gap energy at 0 K	E_g	3.510	0.8	1.43	eV
Band gap energy at 300 K	E_g	3.42	0.78	1.43	eV
$\parallel$ electron eff. mass	$m_e^{\parallel}/m_0$	0.12	0.16	–	–
$\perp$ electron eff. mass	$m_e^{\perp}/m_0$	0.13	0.16	–	–
$\parallel$ heavy hole eff. mass	$m_{hh}^{\parallel}/m_0$	1.45	1.39	–	–
$\perp$ heavy hole eff. mass	$m_{hh}^{\perp}/m_0$	1.52	1.41	–	–
$\parallel$ light hole eff. mass	$m_{lh}^{\parallel}/m_0$	1.45	1.39	–	–
$\perp$ light hole eff. mass	$m_{lh}^{\perp}/m_0$	0.168	0.12	–	–
$\parallel$ split-off hole eff. mass	$m_{so}^{\parallel}/m_0$	0.14	0.1	–	–
$\perp$ split-off hole eff. mass	$m_{so}^{\perp}/m_0$	1.96	1.69	–	–

2.2.3 Optical Absorption of III-Nitrides

The optical properties of InGaN depend on the concentration of In. Most importantly for solar cells, is optical absorption in InGaN. The absorption of light in a semiconductor can be modeled simply by the equation:

$$I_T(\lambda) = I_I(\lambda)e^{-\alpha(\lambda)t} \tag{17}$$

Where I_I and I_T are the intensities of the incident and transmitted light, t is the thickness of the material, and $\alpha(\lambda)$ is the absorption coefficient as a function of the wavelength. Prior to 2002, when the band gap energy of InN was revised down to it's current value, the average value of α was reported to be of the order of 1E5 cm^{-1}, and this was later confirmed[60, 61, 62, 63]. Furthermore the absorption coefficient was found to fit the function:

$$\alpha(\frac{hc}{\lambda}) = \alpha_0 \frac{\sqrt{\frac{hc}{\lambda} - E_g}}{\frac{hc}{\lambda}} \tag{18}$$

Where α_0 is approximately 5E5 $eV^{1/2} \cdot cm^{-1}$, h and c are Planck's constant and the speed of light respectively, and E_g is the band gap energy of the InGaN material under consideration[60].

2.2.4 Strain and Polarization in III-Nitrides

Understanding of elastic deformations can be very helpful for characterizing III-Nitride materials. As mentioned above we can relate deformation within a the crystal to stress using Hooke's Law. What this means is that we consider the strain to be deviations of atoms from their equilibrium positions within the crystal lattice as defined by:

$$\epsilon_x = \frac{a_0 - a}{a_0} \tag{19}$$

$$\epsilon_z = \frac{c_0 - c}{c_0} \tag{20}$$

Furthermore we assume that the material is elastic, which means that force required to cause a strain ϵ varies linearly with the size of the displacement and that in the absence of stress the material would return to it's equilibrium state. In this way we can define the Cauchy strain tensor:

$$\sigma_{ij} = C_{ijkl}\,\epsilon_{kl} \tag{21}$$

Finally it is common to take symmetry into account and write the stress and strain tensors in Voigt notation:

$$\sigma = \begin{bmatrix} \sigma_{xx} & \sigma_{yy} & \sigma_{zz} & \sigma_{yz} & \sigma_{xz} & \sigma_{xy} \end{bmatrix} \tag{22}$$

$$\epsilon = \begin{bmatrix} \epsilon_{xx} & \epsilon_{yy} & \epsilon_{zz} & \epsilon_{yz} & \epsilon_{xz} & \epsilon_{xy} \end{bmatrix} \tag{23}$$

As mentioned in the previous section, III-Nitride materials are polar. When the crystal is perturbed from equilibrium they display piezoelectric polarization. This effect can be calculated by the piezoelectric tensor, d:

$$P_{\mathrm{pz},i} = d_{ijk}\,\sigma_{jk} \tag{24}$$

Some of the values of piezoelectric tensor for InN and GaN have been provided in table 3.

Of particular interest in the case of epitaxially grown $\mathrm{In}_x\mathrm{Ga}_{1-x}\mathrm{N}$ is biaxial strain in the basal plane. This can be because the InGaN has a larger a_0 lattice constant than GaN. In this situation the crystal is either under tensile stress or compressive stress perpendicular to the c-axis. The result of this is for the crystal to be displaced from it's equilibrium position in both the a and c-axes as shown in figure 14.

To determine the piezoelectric we follow the procedure of Bernardini *et al.* in which the polarization of the two end point binaries is first calculated and the final

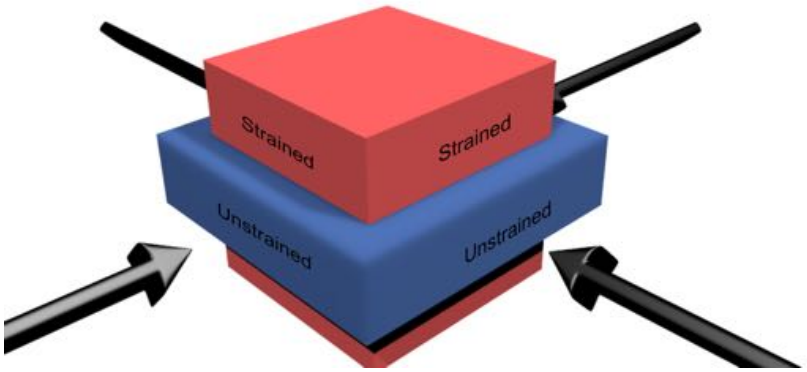

Figure 14: Biaxial Strain representation. Strain in the x and y axes results in a deformation in the x, y, and z directions

effected determined using Vegard's law[58, 59]. The strain can be determined to be:

$$\epsilon_{xx} = \frac{a_{\mathrm{GaN}} - a_{\mathrm{In}_x\mathrm{Ga}_{1-x}\mathrm{N}}}{a_{\mathrm{In}_x\mathrm{Ga}_{1-x}\mathrm{N}}} \tag{25}$$

$$\epsilon_{zz} = \frac{c_{\mathrm{GaN}} - c_{\mathrm{In}_x\mathrm{Ga}_{1-x}\mathrm{N}}}{c_{\mathrm{In}_x\mathrm{Ga}_{1-x}\mathrm{N}}} \tag{26}$$

$$\epsilon_{yy} = \epsilon_{xx} \tag{27}$$

$$\epsilon_{yz} = \epsilon_{xz} = \epsilon_{xy} = 0 \tag{28}$$

This type of strain is particularly useful for determine the crystal composition using X-Ray diffraction. The piezoelectric polarization for the binaries InN and GaN, $P_{pz_{\mathrm{InN}}}$

and $P_{pz_{\mathrm{GaN}}}$, computed with those values of ϵ:

$$P_{pz_{\mathrm{InN}}} = \begin{pmatrix} 0 & 0 & 0 & 0 & d_{15_{\mathrm{InN}}} & 0 \\ 0 & 0 & 0 & d_{15_{\mathrm{InN}}} & 0 & 0 \\ d_{31_{\mathrm{InN}}} & d_{31_{\mathrm{InN}}} & d_{33_{\mathrm{InN}}} & 0 & 0 & 0 \end{pmatrix} \cdot \begin{pmatrix} \epsilon_{xx} \\ \epsilon_{xx} \\ \epsilon_{zz} \\ 0 \\ 0 \\ 0 \end{pmatrix} \tag{29}$$

$$P_{pz_{\mathrm{GaN}}} = \begin{pmatrix} 0 & 0 & 0 & 0 & d_{15_{\mathrm{GaN}}} & 0 \\ 0 & 0 & 0 & d_{15_{\mathrm{GaN}}} & 0 & 0 \\ d_{31_{\mathrm{GaN}}} & d_{31_{\mathrm{GaN}}} & d_{33_{\mathrm{GaN}}} & 0 & 0 & 0 \end{pmatrix} \cdot \begin{pmatrix} \epsilon_{xx} \\ \epsilon_{xx} \\ \epsilon_{zz} \\ 0 \\ 0 \\ 0 \end{pmatrix} \tag{30}$$

Since we are interested in the c-axis direction:

$$P_{pz_{\mathrm{InN},z}} = 2d_{31_{\mathrm{InN}}}\epsilon_{xx} + d_{33_{\mathrm{InN}}}\epsilon_{zz} \tag{31}$$

$$P_{pz_{\mathrm{GaN},z}} = 2d_{31_{\mathrm{GaN}}}\epsilon_{xx} + d_{33_{\mathrm{GaN}}}\epsilon_{zz} \tag{32}$$

Introducing the Poisson ratio which can be derived from equation (6):

$$\epsilon_{zz} = -2\frac{C_{13}}{C_{33}}\epsilon_{xx} \tag{33}$$

$$\implies P_{pz_{\mathrm{InN},z}} = 2\epsilon_{xx}(d_{31_{\mathrm{InN}}} - d_{33_{\mathrm{InN}}}\frac{C_{13}}{C_{33}}) \tag{34}$$

$$P_{pz_{\mathrm{GaN},z}} = 2\epsilon_{xx}(d_{31_{\mathrm{GaN}}} - d_{33_{\mathrm{GaN}}}\frac{C_{13}}{C_{33}}) \tag{35}$$

Finally, using Vegard's law:

$$P_{pz,z} = xP_{pz_{\mathrm{InN},z}} + (1-x)P_{pz_{\mathrm{GaN},z}} \tag{36}$$

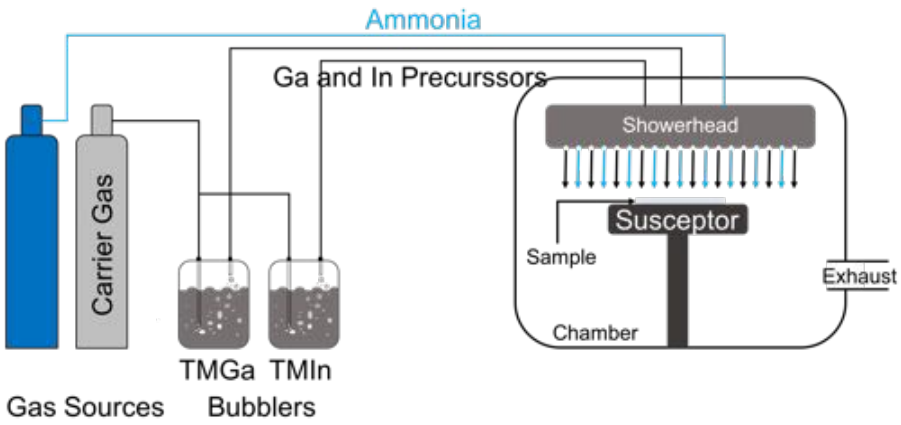

Figure 15: Schematic of an MOVPE system for growing InGaN

2.2.5 Indium Gallium Nitride Epitaxy and Challenges

There are two primary ways of making InGaN semiconductor crystals: molecular beam epitaxy (MBE) and metal organic vapor phase epitaxy (MOVPE). Both methods involve transporting the constituent In, Ga, and N elements to a substrate so that the elements can distribute on the substrate and become incorporated into the crystal. MBE systems often utilize pure elemental sources for the material (just Ga, for example) and transport the material from the source to the substrate using Knudsen cells and other methods. MBE has the capability of growing extremely pure and well ordered semiconductor crystals, however its downside is the speed of crystal growth and throughput.

MOVPE utilizes organic molecules like trimethylgallium (TMGa) to transport the semiconductor crystal constituents to the substrate. These organic molecules are easier to transport because they are often gasses or liquids and neither require the heating nor careful control of the flux that MBE requires. TMGa, for example, is kept in a bubbler as a liquid and then an inert carrier gas like H_2 or N_2 is bubbled through the liquid and then used to transport the precursor to the substrate as shown in figure 15. These precursors are heated at the substrate to cause them to crack, or break apart leaving the inorganic component (Ga for example) behind on the substrate.

The organic components of the precursors are volatile and can be exhausted from the growth chamber. MOVPE films can be of very high crystalline quality and can be nearly atomically abrupt like MBE films despite challenges of defects introduced by the atmosphere and growth temperature [64]. Furthermore, MOVPE systems can achieve much higher growth rates and higher throughput than MBE reactors. This is due in large part because MBE reactors must operate under high vacuum, and so the uniformity of the deposited crystal is related to the kinetics of the sources being deposited on the substrate and redistribution of adsorbed adatoms on the substrate. MOVPE methods can operate at atmospheric pressure and so the uniformity of the deposition is controlled by gas flow in the reactor and substrate heating. As a result the crystal can be deposited on a much larger area at one time using MOVPE making it the industrially preferred method of growing crystals like InGaN. Furthermore, the films grown for this work were all done using MOVPE and so this will be the method detailed in this thesis.

2.2.5.1 Lack of Lattice Matched Substrates

There are several challenges associated with the growth of InGaN solar cells. The first challenge that cannot be overlooked is the lack of a lattice-matched substrate. Generally for epitaxy to occur one must start with a crystal of the same lattice and then add the components of the crystal slowly so that they can use the existing crystal as a template for growth. Crystalline Si, for example, uses the Czochralski growth method where a seed crystal is lowered into a crucible full of molten Si and slowly drawn from the melt cooling and solidifying the Si around the seed into a large single crystal ingot. It is not practicle to grow GaN from a melt. So the majority of InGaN epitaxy is done by MOVPE. While other material systems, like Si or GaAs, use the crystal that they are trying to grow as the template, this is not practical for GaN. Most GaN epitaxy occurs using a Sapphire template [65]. Sapphire does have a hexagonal

crystal, but there is a 14% difference of lattice spacing between the sapphire lattice and GaN lattice and 29% between sapphire and InN. The GaN or InGaN will adopt the Sapphire lattice during growth leading to intrinsic internal stress. As the crystal grows thicker the elastic energy it takes to keep the accommodate the different lattice parameter increases until it is energetically favorable to relieve the stress through a defect in the crystal lattice. The thickness at which this this favorable is called the critical thickness [66]. For sapphire this thickness is very small and so GaN on sapphire often suffers from high concentrations of defects, typically on the order of 1×10^{8} cm^{-3}. To alleviate this problem other substrates have been considered for GaN growth including SiC, ZnO, and Si (1 1 1). In spite of favorable lattice mismatch and/or elastic properties of these substrates none have been shown to improve upon the dislocation density of GaN on sapphire. The primary improvement over sapphire has been in introduction of bulk GaN substrates, typically grown by hydride vapour phase epitaxy (HVPE)[67]. The large scale manufacturing and adoption of these substrates is still in it's infancy making them prohibitively costly.

2.2.5.2 InGaN Phase Separation

Further complicating the growth of InGaN is the problem of phase separation. This is the issue of $In_xGa_{1-x}N$ alloys tending to separate into regions of higher and lower In concentration, even for small In concentrations. This thermodynamics problem caused by differences in the chemical affinity between GaN and InN resulting in solid phase immiscibility. This miscibility gap can be expressed using a model of regular solutions. Thus the change in Gibbs free energy, ΔG, of an $In_xGa_{1-x}N$ alloy can be expressed as:

$$\Delta G = \Delta H_m + RT\left(x\ln(x) + (1-x)\ln(1-x)\right) \tag{37}$$

$$\Delta H_m = \Omega\, x\,(1-x) \tag{38}$$

The second term in the equation for the change in Gibbs free energy, $RT(x\ln(x) + (1-x)\ln(1-x))$, is $-T$ times the entropy of mixing. ΔH_m is the enthalpy of mixing and is related to the heat released when the two end point binaries (GaN and InN in this case) are mixed, and must be parameterized by Ω, the regular solution interaction parameter. This parameter can be calculated using a variety of models including a semi-emperical delta-lattice-parameter model or a valence-force-field model[68]. This model uses the energy to stretch or bend interatomic bonds to calculate the microscopic strain energy in a regular solution. The enthalpy of mixing is the found by summing over the different strain energies[69, 68]. Ho and Stringfellow found values of Ω to be between 5.63 and 6.32 kcal/mole depending on whether the mixture was Ga or In rich respectively[68].

This leads to a phase diagram that exhibits spinodal decomposition for $In_xGa_{1-x}N$ for compositions with $x > 0.06$ for InGaN grown at 800° C[68]. That means that compositions greater than this are thermodynamically unstable. When the InGaN mixtures decompose there will be regions that are In rich have a lower band gap energy than the regions that are Ga rich and have a diode characteristic with a much lower threshold voltage than the rest of the cell. This lower V_{oc} will significantly contribute to a degradation of solar cell efficiency. This problem can be mitigated to a certain extent by incorporating the effect of elastic strain.

Growing pseudomorphically strained InGaN on GaN [70, 2], however it is not practical to grow thick layers of strained InGaN due to the thin critical thickness. Other methods for avoiding spinodal decomposition involve the insertion of thin layers of GaN into the thicker InGaN which serve relieve the compressive strain and absorb the excess In [71]. Also nano-selective area growth methods seem to be an attractive alternative to bulk methods for some applications which require high In incorporation [72].

Including strain into the model of a normal solution can be done my adding

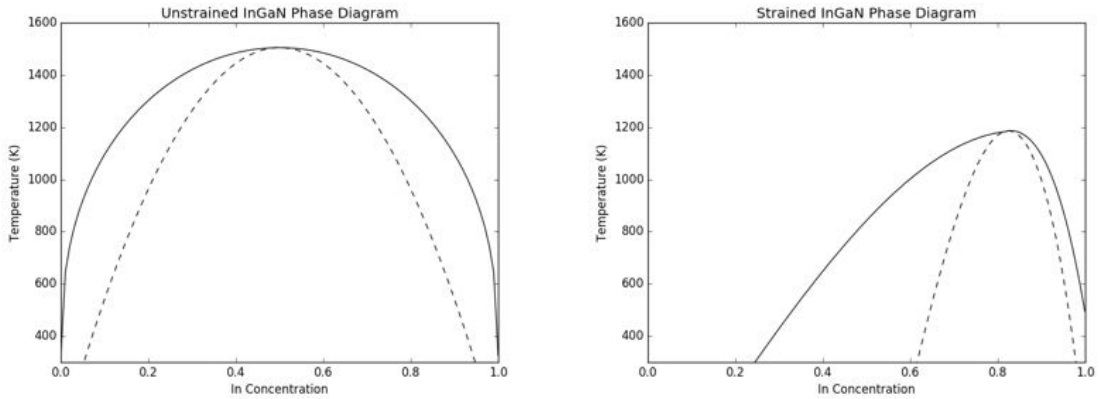

(a) Unstrained T–x diagram[68] (b) Strained T–x diagram[70]

Figure 16: Phase Diagram of relaxed and fully strained InGaN

an additional enthalpy term, ΔH_s, to the equation for the change in Gibbs free energy. In the case of InGaN on GaN the strain is biaxial and perpendicular to the c-axis. Therefore the enthalpy can be written in terms of the lattice displacement from equilibrium Δa and the ternary InGaN lattice parameter a:

$$\Delta H_s = C N_A V \left(\frac{\Delta a}{a}\right)^2 \tag{39}$$

where (40)

$$C = C_{11} + C_{12} - 2\frac{C_{13}^2}{C_{33}} \tag{41}$$

Here C_{ij} are the various members of the InGaN stiffness tensor and $V = \frac{\sqrt{3}}{4}a^2c$ is the molecular volume if the ternary compound. This has the effect of shifting the phase diagram as shown in figure 16. Figure 16 shows the two limits of InN and GaN miscibility. Karpov neglects to consider factors such as bowing, but it does successfully demonstrate that growing coherently strained InGaN on GaN can significantly improve phase separation[70]. Furthermore it should be noted that crystal growth processes like MOVPE and MBE allow for the creation of thermodynamically unstable films. These films if given infinite time or energy would eventually separate into their thermodynamically stable forms, but this is a process limited by kinetics that we can ignore.

2.2.5.3 Difficulty of p-doping GaN

P-type doping of GaN was one of the early challenges facing researchers. The challenges were that undoped GaN is n-type as a result of native defects in in the crystal and that GaN is a wide band gap material and so there were not many candidates for dopants. The search for an effective dopant remained elusive until 1989 when Akasaki demonstrated p-type conduction in Mg compensated films activated by electron irradiation[73, 74]. Shortly there after Nakamura was able to demonstrate Mg doping via a two step process in which the film is grown with Mg (usually from a bis(cyclopentadienyl)magnesium or Cp_2Mg precursor) and then annealed at high temperature under nitrogen[75]. This is the process that is used to this day for doping GaN.

There are, however, some tradeoffs to consider to Mg doping of GaN. Firstly the activation energy of Mg is 160 meV, which is comparatively high for dopants. Consider B doping in Si, for example, where the activation energy is 45 meV. This results in only 1–2% of the Mg dopants contributing to the p-type conduction. Thus to compensate for the intrinsic n-type quality of the film and for the low acceptor rate of Mg high concentrations (1E20 cm^{-2}) are required in order to for the GaN film to display p-type conduction. This has detrimental effects to the GaN film quality. Furthermore, interstitial hydrogen has been shown to form a complex with Mg in the crystal which deactivates the dopant. This is why the annealing occurs in a nitrogen free atmosphere. This causes an additional problem as without a nitrogen precursor like ammonia (NH_3) under high temperature the III-N bond can be broken and nitrogen can desorb from the crystal further reducing crystalline quality.

The high temperature growth and annealing of p-type GaN introduces another practical issue for the growth of InGaN/GaN solar cells. P-type GaN is preferred for making the PN junction above the InGaN absorber layers to p-type InGaN because Mg doping in InGaN can contribute to phase separation [2]. The In-N bond strength

is much lower than the equivalent Ga-N bond and this results in In and N desorbing from the crystal at high temperatures lessening the overall In concentration and decreasing the crystal quality of the structure. To overcome this groups have tried increasing the flow of In during InGaN growth but have found that this results in In droplet formation on the substrate surface [76].

2.3 InGaN Solar Cells

As previously mentioned, InGaN has many properties that lend it to the manufacturing of solar cells. Firstly the band gap of InGaN can be tuned from 0.78 to 3.42 eV depending on the concentration of In. This accounts for more than the entire visual spectrum as shown in figure 17, as well as many of the ideal band gap energies for multijunction solar cells as depicted in table 1. Furthermore InGaN is a direct band gap semiconductor and thus has a large optical absorption coefficient, as such only a few hundred nanometers of material is required to absorb most of the above band gap incident light[77]. Si, on the other hand, is an indirect band gap semiconductor and requires several hundred microns of material to absorb the same amount of light [78]. Thus InGaN solar cells can in theory use less material than a comparable Si solar cell. Further benefits of InGaN solar cells are that the materials have a high radiation and thermal tolerance when compared to GaAs solar cells. They have a high carrier mobility and drift velocity compared to thin film solar cell technologies[77, 80]. When considered as a tandem solar cell InGaN has an additional benefit in that the conduction band of $In_{0.46}Ga_{0.54}N$ is aligned with the valence band of Si[21]. Thus a n-$In_{0.46}Ga_{0.54}N$/p-Si junction as could be found in a series connected or two terminal solar cell would have a low resistance[77].

Despite these benefits, InGaN solar cells are still plagued with poor performance. The record efficiency for an InGaN solar cell remains around 6%. This caused by difficulties in growing high In concentration InGaN, high defect densities, and poor

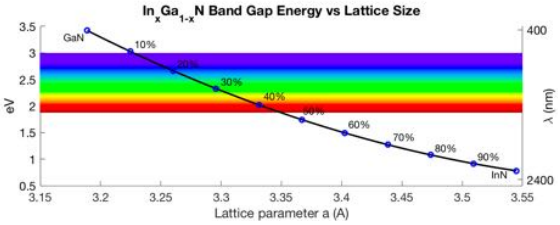

(a) Band gap *vs* lattice parameter

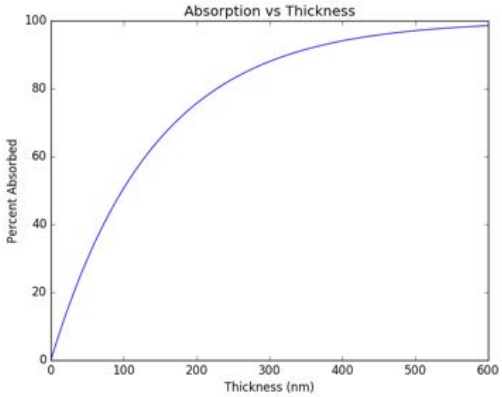

(b) Optical Absorption for 16% In and 3.1 eV photons[79]

Figure 17: Band gap of InGaN compared to other solar cell materials and the optical absorption properties of InGaN compared to Si

metal contacts to the p-type GaN resulting in large series resistances.

The promise of III-nitrides as photovoltaics has been well documented and attracted the attention of many researchers[80]. One can characterize the solar cells into a variety of categories: bulk *vs* quantum-structured cells and heterojunction *vs* homojunction cells. The bulk cells consist of a single material absorber of GaN or InGaN, where the quantum-structured cells utilize compositional variations within the absorber layer to create quantum wells, superlattices, or other quantum structures. The quantum structure has the benefit of utilizing high In content layers pseudomorphically strained to the GaN template, thus maintaining the crystal quality and having strong light absorption within the quantum wells [81]. However the overall thickness of the InGaN quantum structures is limited, and thus much of the light passes through the InGaN layers unabsorbed. The homojunction photovoltaic devices are made using combinations of p-type, intrinsic, and n-type InGaN. Heterojunction devices are made by combining an InGaN absorber with n-GaN and/or p-GaN. The heterojunction devices typically have a structure of p-GaN/nid-InGaN/n-GaN. The homojunction devices usually display lower collection efficiencies and thus degraded short circuit currents compared to heterojunction devices [82]. This translates to

nearly double the efficiency of heterojunction cells ($\eta = 0.62\%$ *vs* $\eta = 0.32\%$) under illumination of 1 sun of AM1.5G spectra [82]. Comparisons of many of the InGaN solar cells are presented in table 3.

Structure	Growth	In %, (nm)	V_{oc} (V)	J_{sc} (mA/cm^2)	Spectra	Ref.
Homojunction Solar Cells						
p-n InGaN	MOVPE	18 (320)	0.43	0.04	UV	[83]
		28 (100)	2.1	–	Light + UV	[79]
		12 (300)	1.5–2	0.04	–	[84]
		25 (700)	1.5	0.5	AM1.5G	[85] [86]
		14.8–16.8 (80)	1.73/1.47	0.91/0.26	AM0/AM1.5G	[87]
	MBE	31 (700–1000)	0.55/0.78	0.24/1.99	AM0/3 suns AM0	[88]
		14–33 (400–1000)	0.2–1.8	1–2.2	UV	[89]
p-i-n InGaN	MOVPE	2–10 (400)	0.96–2.24	1.4–1.87	UV	[90]
	MBE	0–30 (800)	2.5	30	UV	[91] [92]
Quantum Heterojunction Solar Cells						
p-GaN/InGaN-GaN MQW/n-GaN	MOVPE	30 (24)	2	1.5	white source	[93]
		20/28 (15/15)	2.2/1.8	0.66/1.09	AM1.5G/UV enhanced	[94]
		30 (27)	1.95	0.83	AM1.5G	[95]
		35 (36)	1.8	2.56	AM1.5G	[96]
		23 (25)	2.05	1.09	AM1.5G	[97]
InGaN-GaN SL	MOVPE	25 (84)	1.4	0.8	AM1.5G	[98]

2.3.1 Challenges associated with the fabrication of InGaN solar cells

Apart from and in some cases arising from the issues associated with the growth of InGaN semiconductor crystals there are additional challenges associated with the

Structure	Growth	In %, (nm)	V_{oc} (V)	J_{sc} (mA/cm^2)	Spectra	Ref.
Quantum Heterojunction Solar Cells						
InGaN-GaN MQW	MOVPE	19–36 (46)	2.72–2.92	2.72–2.97	AM1.5G	[99]
InGaN-AlGaN SL	MOVPE	21 (42)	2.1	0.84	AM1.5G	[100]
InGaN-InGaN SL	MOVPE	7/17 (240)	1.78	3.08	AM1.5G/1.5 suns	[101]
Bulk Heterojunction Solar Cells						
p-GaN/InGaN/n-GaN	MOVPE	4–5 (200)	2.4	–	Light + UV	[102]
		12 (200)	1.81	4.2	Concentrated AM0	[103]
		10 (150)	2.1	0.46	AM1.5G	[104]
		10 (150)	2.09	0.52	AM1.5G	[105]
		8 (150)	1.8	0.44	AM1.5G	[106]
		10 (250)	2.23	1.59	AM1.5G	[107]
		12 (60)	1.89	1.06	AM1.5G	[108]
		0–11 (200)	1.33	0.59	AM1.5G	[109]
		108 (200)	2.0	0.83	AM1.5G	[110]
	MBE	11 (90)	1.75	1.11	AM0	[111]

Table 4: List Published of InGaN Solar Cell Designs and Performances [4]

fabrication of InGaN solar cells. Firstly, intrinsic GaN (often called non-intentionally doped or nid-GaN) is a strong n-type semiconductor with a carrier concentration ranging from 1E16 to 1E18 [112]. The background concentration can be compensated for by the inclusion of Fe during nid-GaN growth [113, 114]. The high background would not be an insurmountable problem, except that it is quite difficult to dope GaN p-type [2]. Mg is the most common p-type dopant for GaN, but of the acceptors used it also has the largest activation energy [2]. This results in only between 1% and 3% of the Mg acceptors in the crystal actively contributing to p-type conductivity at room temperature. Furthermore, there is the risk of forming hydrogen complexes with native defects in GaN like nitrogen vacancies, V_N-H, or with the Mg dopants Mg-H complexes which can deactivate the Mg dopants and compensate for p-doping [115, 116]. As there is hydrogen present during the epitaxial growth process a prolonged annealing step in a hydrogen-free ambient is required. This in turn, may lead to a desorption of nitrogen introducing defects into the crystal. p-GaN's sensitivity to hydrogen also has ramifications to processes further down the line as well as it is common to use SiO_2 as a dielectric but many recipes for depositing and etching SiO_2 also include hydrogen. Thus if used, the material must be annealed to reactivate the Mg dopants.

A further challenge involves v-defects. These are defects that originate at threading or screw dislocations within the crystal. Growth at the site of the defect occurs slower than in the bulk resulting in a V-shaped hexagonal pit on the surface. When contacting the top surface of the structure metal can seep into the pit and create a short-circuit path to the bottom layers. The best alternative to this is to improve the film quality to avoid v-defects. However as solar cell devices are quite large compared to LEDs (1 cm^2 vs 15 mm^2) or other devices made with GaN materials the elimination of v-defects may be an unobtainable goal. Further methods of compensating for the v-defects include filling the defects with a spin-on hydrogen silsesquioxane (HSQ)

resin [2].

The metallization of n-type and p-type GaN also presents challenges to solar cell fabrication. Specifically, there is a difficulty obtaining ohmic contacts with n and p-type GaN. Ohmic contacts are preferred for solar cells because the alternative, Schottky contacts result in a barrier to collecting the charge carriers which reduces the solar cell efficiency. The metals used to make ohmic contact to need to have the proper work function. On n-type GaN ohmic contact is typically achieved with low work function metals like Ti or Al [117, 118, 119]. Further improvements on n-type GaN can be made by depositing an alloy of Ti and Al as well as by annealing [120]. Formation of an ohmic contact in p-type GaN, however, is extremely difficulty. There are not many metals with the appropriate work function to form an ohmic contact on p-type GaN. This problem is exacerbated by low p-type activated dopant concentrations. Thus if a Schottky contact is formed the barrier to carriers is wide and the tunneling efficiency is low. Ohmic contact formation on p-type GaN is extensively studied however [121]. Typically thin layers of Ni and Au are used to make the contacts [122, 123]. These contacts are then annealed to improve their resistivity.

Finally, there are challenges that arise from the use of dry etching in the processing of the solar cells. Dry etching introduces damage to the surface of the semiconductor [124]. This damage is responsible for degrading solar cell performance by introducing donor like traps near the surface, further degrading the p-type GaN carrier concentration [124]. However, the effect of the etch damage can be lessened by chemical or annealing treatments [124].

2.3.2 Semibulk InGaN for Photovoltaics

One of the primary blocking points of high efficiency InGaN solar cells is the challenge of growing thick, high In content InGaN[4]. The lack of high In content results in the material being transparent to most of the solar spectrum and as a result InGaN solar

cell efficiency has been blocked below 5%[4, 125]. One method used to counter this is to alternate between thicker InGaN and thin GaN layers forming what is called a semibulk (also called multi-layer) material [2, 71, 126]. The thin GaN interlayers serve to absorb excess In as well as relieve some of the built up strain and yet the layers are thin enough to not provide a significant barrier to charge transport at low In concentration as shown in figure 18.

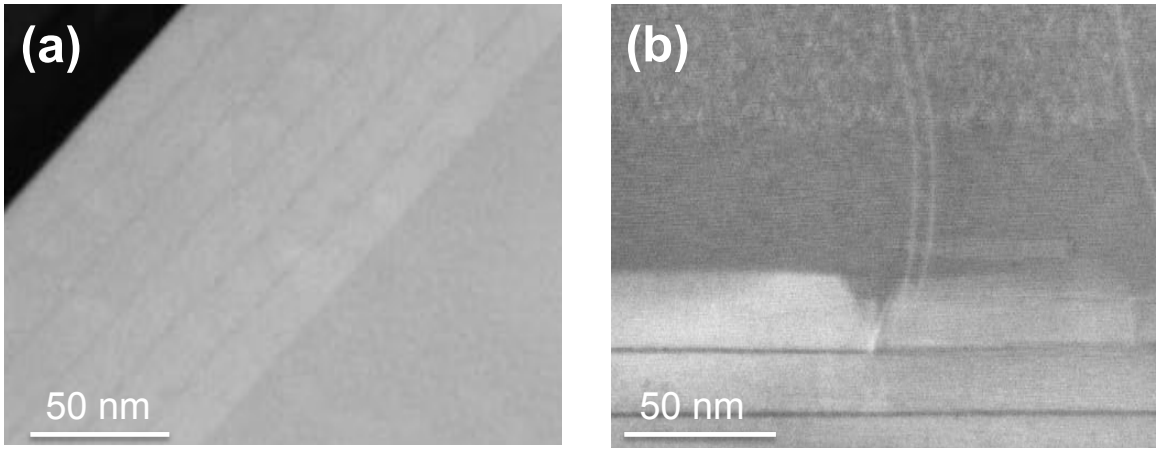

Figure 18: TEM of a semibulk InGaN absorber layer used for a solar cell showing (a) good periodicity and (b) the presence of defects[13]

Adding thin GaN barriers in the absorber region will effect the electrical and optical performance of InGaN based solar cells. We can simulate the effect on the solar cell conversion efficiency for different GaN interlayer thicknesses as is shown in figure 19[13].

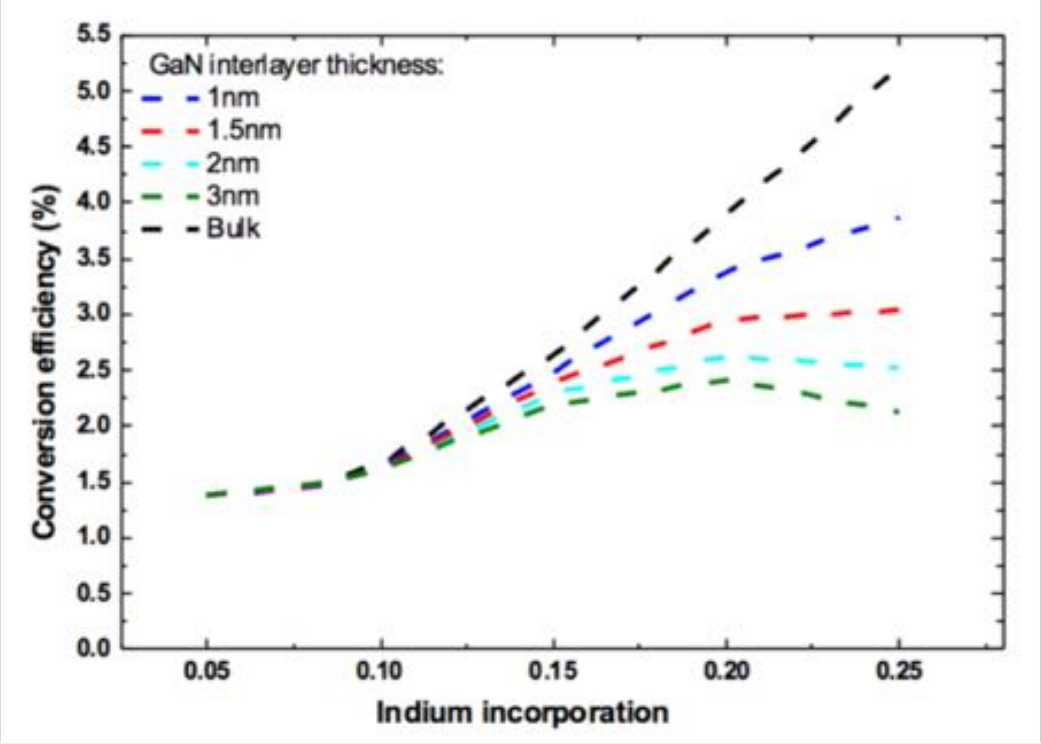

Figure 19: Simulated solar conversion efficiency for thick InGaN semibulk absorbers with different GaN interlayer thickness[13]

As is clear from the figure, for InGaN solar cells where the In content is less than 10% the CE is not strongly effected by the addition of thin GaN interlayers. However, the addition of the thin interlayers do allow us to grow a thicker, higher quality absorber which will increase the solar cell short circuit current. Using the 8% semibulk layer shown in figure 18 we have grown p-GaN on top of it to form a PIN solar cell and determine the initial, unoptimized photovoltaic performance as shown in figure 20.

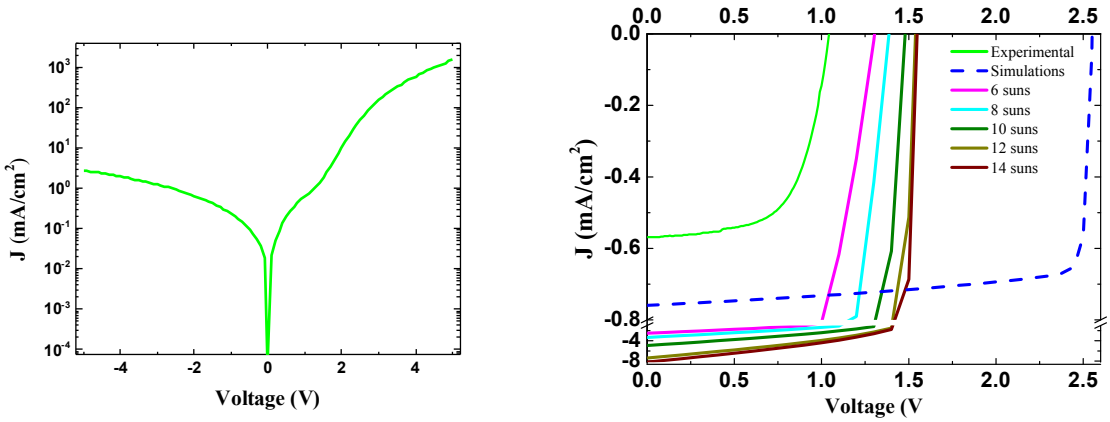

(a) Dark IV characteristic of 8% semibulk solar cell

(b) Illuminated and Simulated performance

Figure 20: Performance of an 8% semibulk InGaN Solar Cell[13]

Figure 20 shows some remarkable characteristics. Firstly the illuminated current density is near to the simulated value and in–fact represents the highest value reported for an 8% In photovoltaic device. Secondly the short circuit current density increases linearly with amount of concentrated light as would be expected for a high–quality absorber. However the V_{OC} did not increase linearly and saturated at approximately 1.5 V, significantly lower than the simulated value of 2.56 V. This is a result of high series resistance and low shunt resistance. The high series resistance ($\approx 100\ \Omega$) is likely caused by both the junctions in the semiconductor material as well as non-optimized p-contacts and the low shunt resistance ($\approx 6\ M\Omega$) is caused by a lack of passivation of the edge of the mesa coupled with defects in the semiconductor material. Further evidence of material defects is shown in the reverse current in figure 20 (a) which appears to exhibit similar characteristics to a bulk solar cell reported by Sang *et al.* which was dominated by defect-related Poole-Frenkel emission[127]. Further evidence of material defects is shown in figure 18 (b) and in the electron beam induced current (EBIC) measurements of figure 21 (b) and (c). EBIC is discussed in further detail in the next chapter but from the figure one can see inhomogeneities resulting from

defects in the material.

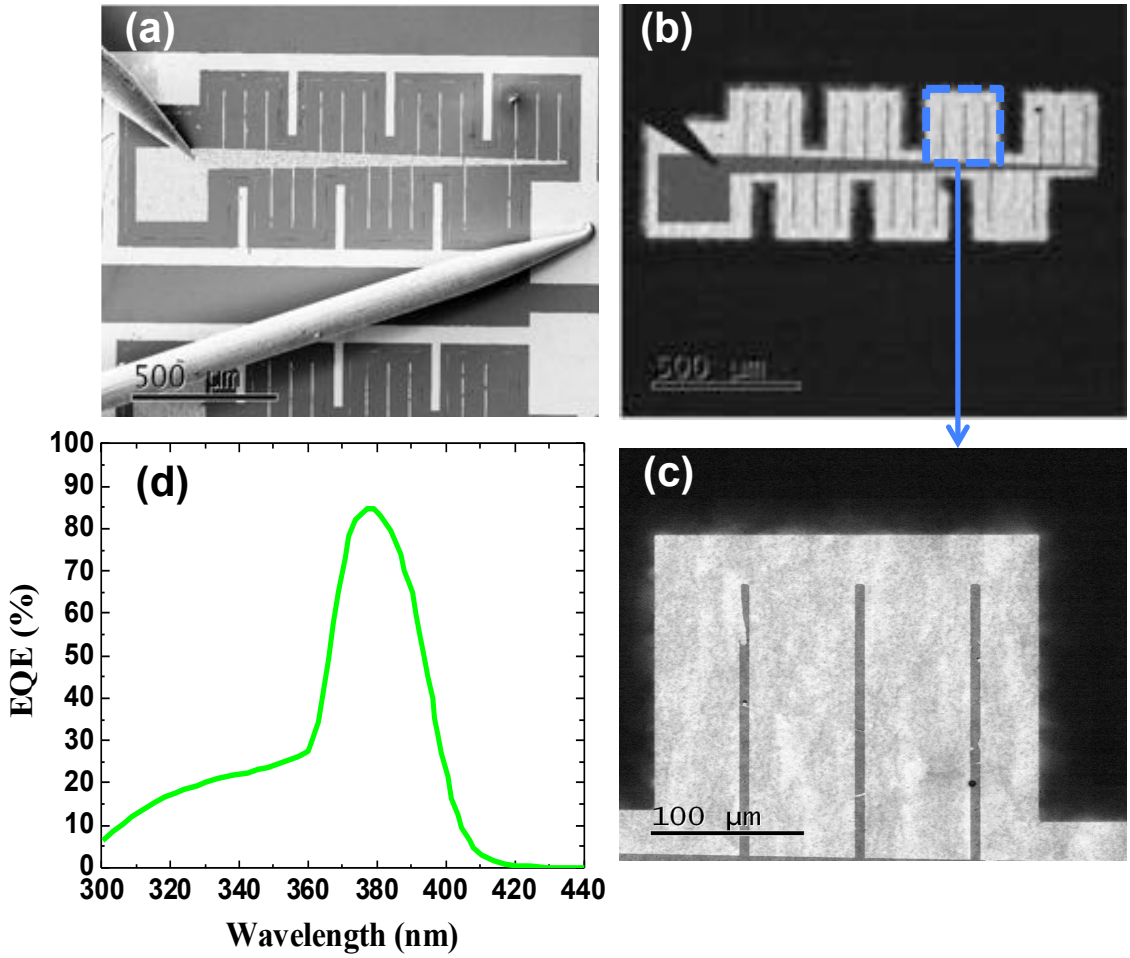

Figure 21: (a) SEM of a semibulk InGaN solar cell and (b and c) EBIC mapping of that same cell. (d) EQE measurements of the solar cell[13]

More exciting about figure **??** is that the semibulk solar cell displayed has a maximum EQE of 85%, at a wavelength of 380 nm. This is the maximum EQE reported for an InGaN heterojunction solar cell. We can further improve the performance of the solar cell at lower wavelengths by optimizing processing conditions as well as investigating new structures with different p-GaN layer thickness. Further gains can be made by reducing the defects caused by lattice mismatch by growing on a GaN substrate as well as carefully optimizing a rear reflector and antirefleciton coatings.

2.3.3 InGaN Tandem solar cells

InGaN/Si tandem solar cells have the possibility to combine the benefits of both materials. Simulations suggest that efficiencies of a InGaN/Si solar cell could be as high as 31%[21]. Furthermore the calculated band alignments of $In_{0.45}Ga_{0.55}N$/p-Si could result in a two–terminal device without the need for a tunnel junction which would reduce the series resistance of the device and further boost collection efficiency[128]. Growing directly on Si is a problem for InGaN materials as there is a large lattice mismatch between Si (111) and InGaN structures. Furthermore is is extremely difficult to grow well crystallized InGaN on Si because Si has a cubic lattice and InGaN is typically grown in the hexagonal lattice configuration. El-Huni *et al.* suggest growing InGaN on a ZnO buffer as this has shown to reduce defect propagation into the nitride material [14, 129]. In order to achieve current matching and implement a high efficiency InGaN Si tandem the In content needs to be around 50%. Furthermore a tunnel junction must be realized in Si. The resulting simulated energy band diagram and solar cell characteristic is shown in figure 22.

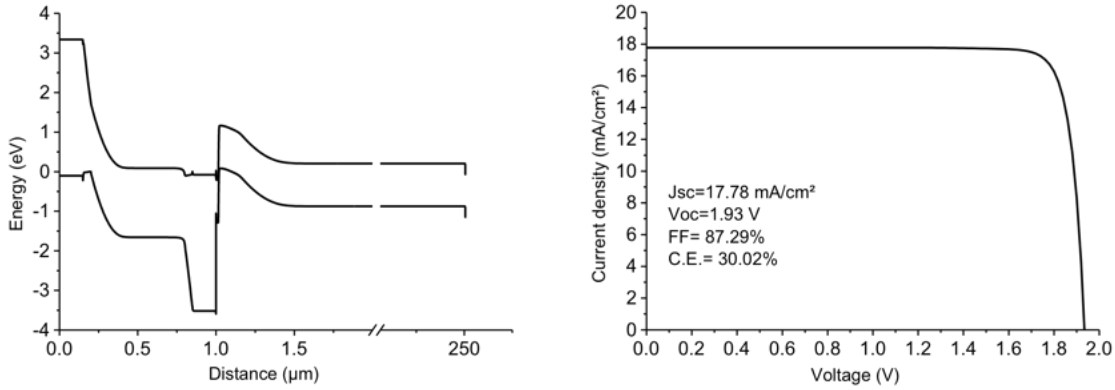

(a) Simulated energy band diagram (b) Simulated solar cell performance

Figure 22: Realistic simulated $In_{0.5}Ga_{0.5}N$/Si monolithic tandem solar cell[14]

The performance of such a solar cell is simulated to be over 30%. However in reality there are many technical challenges associated with realizing such a structure.

First InGaN and p-GaN growth occurs at high temperatures and exceeds the thermal budget of the tunnel junction in the Si. A second scheme is to grow the InGaN solar cell separately on ZnO and release it by chemical liftoff. This solar cell can then be direct bonded to a the Si cell with a ZnO top contact as shown in figure 23. This process is also challenged by the fact that it is currently impossible to achieve such thicknesses of high In content material.

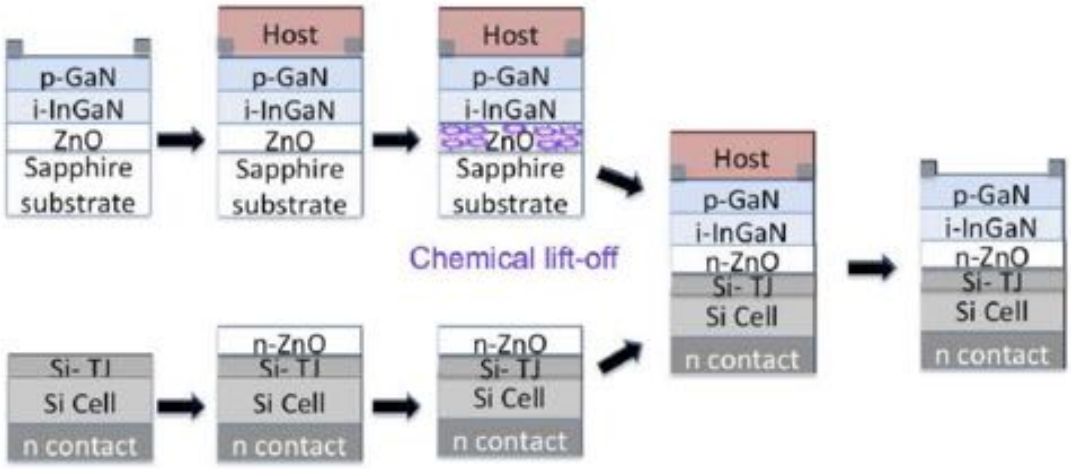

Figure 23: Proposed tandem fabrication of a tandem solar cell

Lower In content monolithic tandems have been achieved by Reichertz *et al.* and Gherasoiu *et al.* using PA-MBE on Si solar cells[130, 131]. Their devices show a poor collection efficiency, however due to the low indium content of the solar cell and the high defect density in the InGaN material. Both of these mechanisms result in efficiency losses. The low indium content results in the material being transparent to most of the solar spectrum resulting in a lower J_{sc}. The high defect density tends to lower the carrier lifetime which lowers the J_{sc} and also tends to decrease the shunt resistance resulting in a lower V_{oc}[4]. The low J_{sc} is particularly troubling for two terminal tandem solar cells because the top and bottom cells will not be

current matched. This issue is readily apparent in the reported EQE of the GaN/Si tandem[130]. Therefore it is unrealistic that a two terminal device will improve in performance by one of todays InGaN solar cells to it [14].

It is for this reason that four terminal InGaN/Si devices are being investigated[14]. In simulated tandem solar cell performances it has been found that even a thin layer (10 nm) of semibulk InGaN with In incorporation of 25% has the ability to increase the overall efficiency of a four terminal InGaN/Si solar cell from between 4–8% for a PERT or PERL Si solar cell alone as shown in figure 24[14].

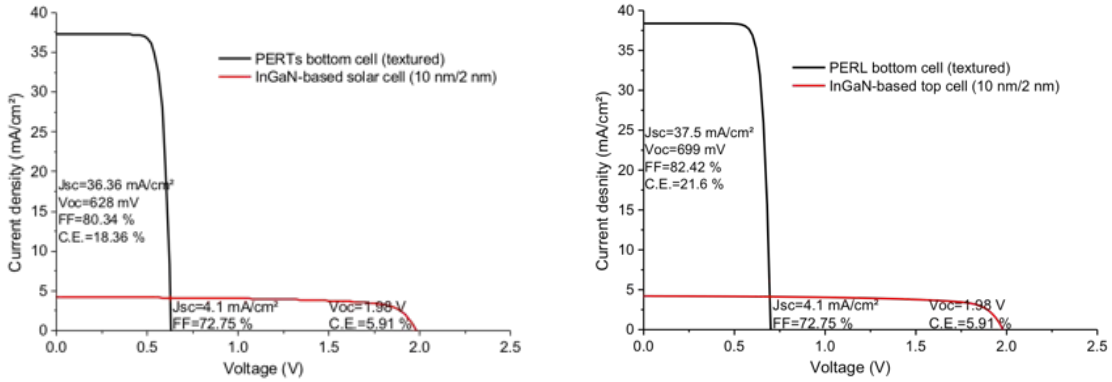

(a) InGaN/PERT-Si Solar Cell

(b) InGaN/PERL-Si Solar Cell

Figure 24: Simulated performance of a 4 terminal InGaN/Si solar cell with a 25% In, semibulk absorber[14]

CHAPTER III

DEVICE FABRICATION

3.1 Solar Cell Design and LED fabrication

Following the success of the first InGaN semibulk solar cells we concluded that the photovoltaic performance could be improved through careful optimization of the device processing. While the device processing does show promise in decreasing the series resistance caused by the contacts and increasing the shunt resistance caused by leakage current across the surface, processing cannot improve the effect of defects in the bulk material or the resistance of the junctions within the material. Presented below is a review of the optimizations that have been achieved and a discussion of what can still be improved.

3.1.1 Process Flow and Photomask Design

The process for fabricating InGaN LEDs and InGaN Solar Cells is the same. The only variations are the semiconductor structure and the passivation of v-pits which is sometimes necessary when processing solar cells. LEDs will have a multi-quantum well (MQW) GaN/InGaN structure and may also have an AlGaN electron blocking layer. Solar cells may have MQWs but they are not limited to this design. Bulk, superlattice, and semibulk absorber layers are also used. There is also a difference in the p-GaN layers on the top of the device. Because the thin MQWs in LEDs are not as sensitive to p-GaN growth temperature and the p-GaN will not absorber the light emitted from the MQWs they will have a thicker p-GaN layer grown at higher temperature than the solar cells V-pits can arise from the low temperature growth conditions of p-GaN layers used to preserve the thick InGaN based absorber layer of solar cells. The relationship between v-pits and solar cell performance is complicated,

and is discussed in greater detail in a later section. Suffice it to say that in some cases it is necessary to passivate the v-pits in between the GaN etching and n-contacting steps show in figure 25. However, for most of the process can be optimized using and LED structure. In fact the optimizations required for high efficiency solar cells also insure that the devices will also operate as efficient LEDs[132]. Thus in order to decouple the processing from the materials we grew a commercial LED structure and optimize the processing using the solar cell mask.

The solar cell and LED process involves many steps which are depicted schematically in cross-section in figure 25.

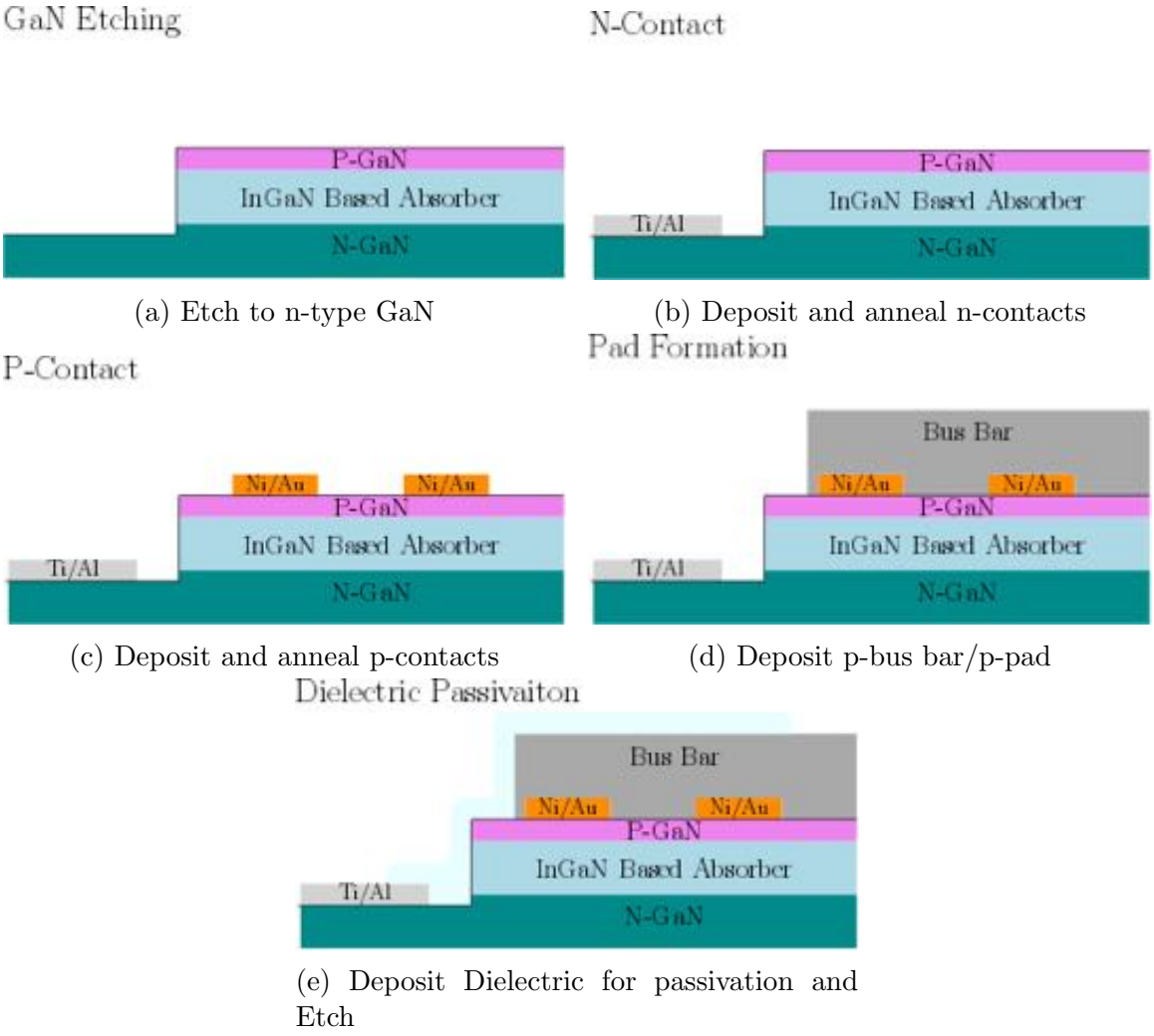

(a) Etch to n-type GaN

(b) Deposit and anneal n-contacts

(c) Deposit and anneal p-contacts

(d) Deposit p-bus bar/p-pad

(e) Deposit Dielectric for passivation and Etch

Figure 25: Typical Solar Cell or LED process using a cover dielectric pattern

In this chapter we deconstruct each processing step and discuss optimizations that we have performed. It is impractical to investigate every parameter and impossible to follow every pathway when optimizing the processing. This is why a through literature review has been included in the discussion of each process step. In this way context into the key parameters and figures of merit can be introduced for each processing step. It is also meant to allow the discussion of each step to stand alone as reference and a starting point that can be built upon by later PhD students.

The presented process flow is just one of many possible routes that may be taken to achieve similar results. For example the presented process flow includes a dielectric layer encapsulating the entire diode at the end of the process. Mesa passivation does not have to occur at the end and often passivation is achieved immediately after etching. This is why we provided for the possibility to try three different passivation schemes. We label these three schemes: cover, edge, and surface passivation and they are depicted schematically in figure 26.

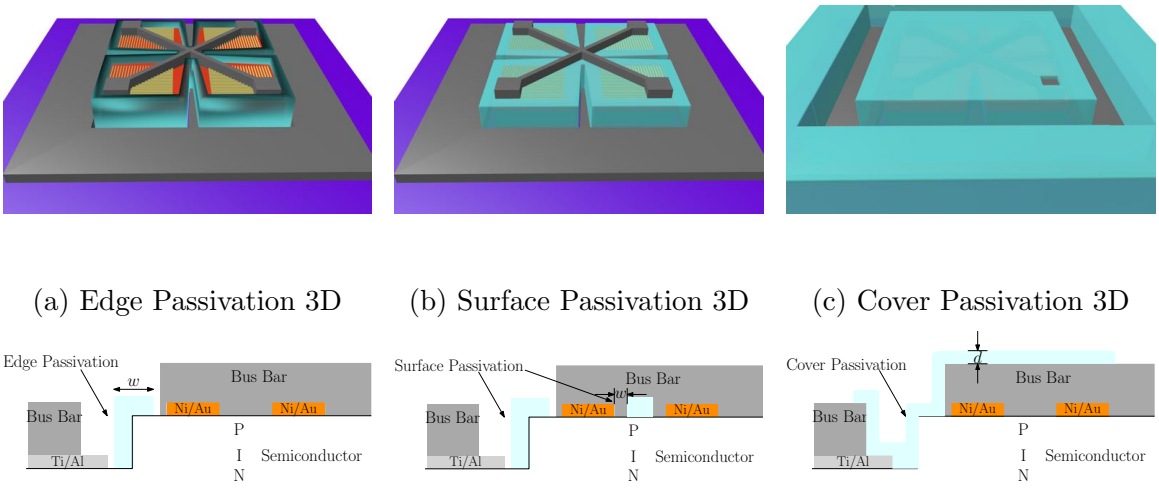

(a) Edge Passivation 3D (b) Surface Passivation 3D (c) Cover Passivation 3D

(d) Edge Passivation (e) Surface Passivation (f) Cover Passivation

Figure 26: Cover, Surface, and Edge Passivation designs

The edge passivation scheme passivates only the edge of the mesa. This prevents

parasitic leakage currents flowing along the surface between the p and n contacts. In the first processing attempt we annealed the p-contacts at high temperature and there was an issue of metal migration on the surface. The surface passivation scheme was meant to help counter-act this issue as well as help us to investigate the use of anti-reflective coatings on the solar cell. We could vary the surface coverage of the dielectric anti-reflective coating by changing the distance between the contact fingers and the dielectric, or the design parameter, w, in figure 26 (d and e). Finally the cover passivation scheme both passivates the mesa and has the highest coverage of dielectric that may be beneficial as an antireflective coating.

The variations of process design are accomplished in parallel on the mask. The layout of the photomask is shown in figure 27 with the locations 1–7 and the 1 cm^2 large solar cells indicated (BSC 1–6).

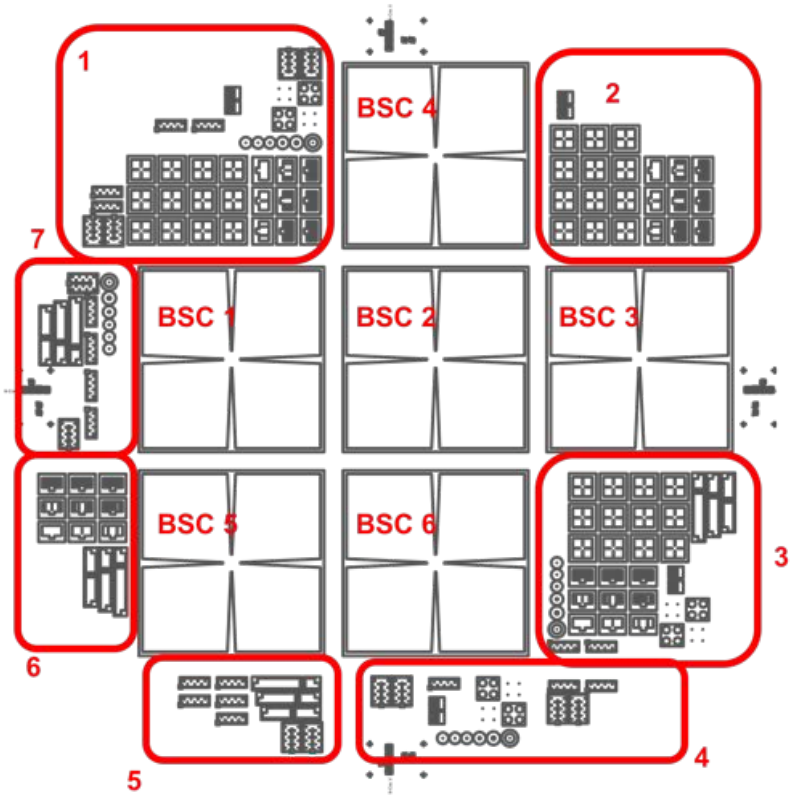

Figure 27: Overview of the entire solar cell/LED photomask

Each of the big solar cells has a different p-contact design and therefore the amount of the mesa that is covered by the p-contact varies from device to device. These values are summarized in table 5.

Table 5: 1 cm^2, BSC solar cells/LED Design

			P-Contact Coverage	
Device	P-Contact Design	Pitch (μm)	(cm^2)	(%)
BSC 1	Fingers	30	0.247	28.2
BSC 2	Fingers	60	0.124	14.4
BSC 3	Fingers	120	0.062	7.2
BSC 4	Current Spreading	N/A	0.742	86.3
BSC 5	Hexagonal Grid	N/A	0.066	7.7
BSC 6	Square Grid	120	0.112	13.1
Common Mesa Area: 0.8602 cm^2, P-Contact Finger Width: 10 μm				

The other locations of the photomask have a large variety of devices and device designs. These devices are classified below in figure 28.

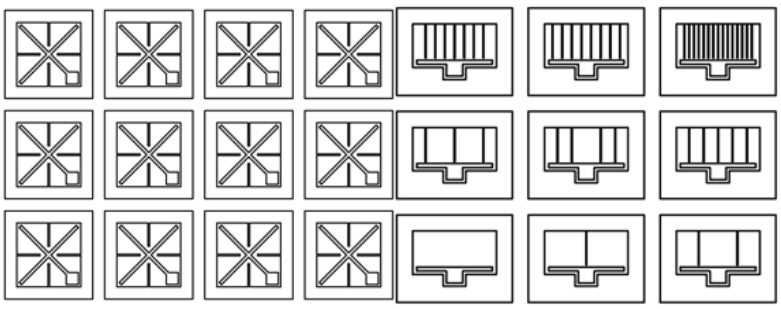

(a) Pattern A, solar cells with varying p-contact and passivation

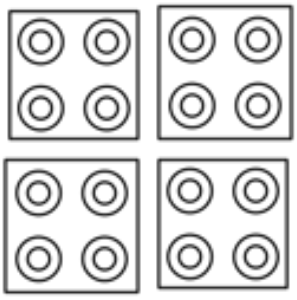

(b) Pattern B, solar cells with varying n-contact

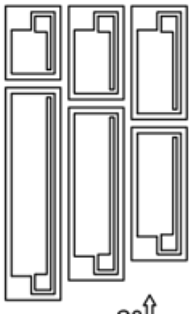

(c) Pattern C, solar cells of varying size

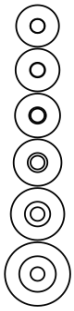

(d) Patterns D and E, TLM devices on n and p-GaN

(f) Pattern G, Copy of LPN solar cells

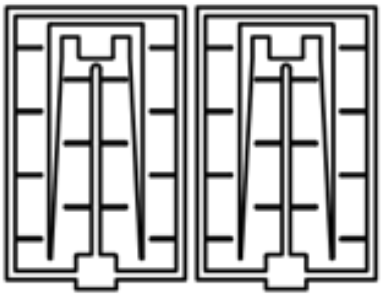

(g) Pattern H, Copy of LPN solar cells

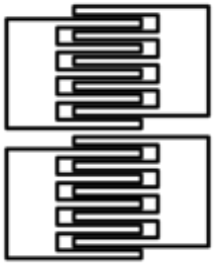

(h) Pattern I, Interdigited conctacts on n and p GaN

Figure 28: Various Device Designs for Solar Cells and LEDs.

The patterns A, B, C, F, G, and H are all solar cells or LEDs. Patterns D and E are circular TLM patterns on both the surface (p-GaN) and etched (n-GAN) layers. The analysis of the c-TLM devices on the p-GaN is challenging because the current flow is

not isolated to the p-GaN, but instead flows through the absorber/emitter region and n-GaN region. The classical diode patterns (F) are circular diodes with the p-contact either on the inside of the circle or on the outside. Lastly the interdigited contacts (I) were added to have the possibility of creating ohmic-schottky contacts. As can be seen examining figure 28 (a) and (b) there are many solar cells for each pattern (each pattern A consists of 12 solar cells and B has 9). These are labeled starting from the top left with the convention A<column><row>. So The top left A pattern is A11, the pattern to the right of A11 is A21, and the bottom right pattern is A43. With this convention we can define the various differences in design from A11 to A43 as is shown in table 6.

Table 6: Solar Cell/LED mask, Pattern A description

	P-Contact Design				Dielectric Etch Design	
Device	Design	Pitch (μm)	Total Area (mm^2)	Mesa Coverage (%)	Design	Design Parameter, w (μm)
A11	Fingers	25	0.328	34.99	Surface	5
A12	Fingers	25	0.328	34.99	Edge	20
A13	Current Spreading	25	0.799	84.97	Edge	20
A14	Fingers	50	0.171	18.17	Surface	5
A21	Fingers	50	0.171	18.17	Edge	20
A22	Fingers	75	0.113	11.97	Edge	10
A23	Fingers	75	0.121	12.91	Surface	5
A24	Fingers	75	0.113	11.97	Edge	20
A31	Fingers	75	0.113	11.97	None	N/A
A32	Fingers	75	0.121	12.91	Surface	2.5
A33	Fingers	75	0.121	12.91	Surface	7.5
A34	Fingers	75	0.121	12.91	Surface	10

Common Mesa Area: 0.940 mm^2, Finger width: 10 μm, Top Pad Total Area: 0.159 mm^2, Pad width: 50 μm

Examination of table 6 shows that on the same sample there can be many devices with different designs allowing for experiments of the device design to occur. It should be pointed out that if the cover passivation scheme is used then all of the devices are passivated the same and the dielectric etch design does not apply. However if the edge

and surface passivation schemes used, then there is variation between two devices with different design parameter, w, as described in figure 26 (d) and (e).

Pattern B has devices where the inclusion of the n-contact inside the mesa varies from zero (n-contact just on the surrounding device) to fifteen but the p-contact pitch and dielectric design remain constant. Pattern C has no n-contact inclusions, no variation of p-contact or dielectric etching but instead the size of the mesa is varied along with the bus bar. The thought being that if there are non-uniformities in the growth of the solar cells or LEDs (like a low density of v-pits) that have roughly the same density as the size of the devices, then by varying the device size we may, over time, be able to determine the effect of these non-uniformities.

3.2 GaN Etching

Etching of GaN is accomplished using a Cl–based plasma in a commercially available inductively coupled plasma (ICP) etcher. Plasma etching, or dry etching, involves the balancing of two mechanisms. First there is a physical etching process in which the plasma is accelerated towards the substrate (III-Nitride materials in this case) and they physical impingement of the ionized species with the substrate can etch the material. This process is highly directional and only the exposed surface will be etched physically. Secondly there is a chemical etching caused by molecules in the plasma reacting with the substrate. The reaction products are volatile and can be exhausted from the etching chamber. The chemical process is more isotropic compared to physical etching, meaning that the reaction can occur laterally, tending to widen etch trenches. The physical reaction doesn't "care" whether the material is nitride, oxide, metal, or photoresist and will remove all of them. Thus the physical etching is not very selective. Furthermore reaction products sputtered from the mask by physical etching may not be volatile and can land on the substrate where it will slow etching progress in that area. This leads to a higher roughness on the etched

surface and in extreme cases results in the formation of "grass" which are fine needle like structures that form under the sputtered mask. The chemical process is much more selective as the species will only react with the substrate material and not the mask. A combination of these processes is necessary to avoid grass formation as the physical etching can sputter mask material onto the substrate and chemical etching can reduce these high-surface area structures. In some cases, typically with Si, very high aspect ratio structures are desired. In these cases it may be desired to use a chemical process to passivate the side-walls of the etched structure limiting the isotropic chemical process. This can be done by pulsing etching and passivation species, as is done with the Bosch process, or by cryogenic ICP etching where the low temperature allows for the formation of an SiO_xF_y passivation layer that is unstable above -70° C. In both cases the passivation layer forms on both the planar surface and the etch sidewall, but the passivation layer on the planar surface removed by the directional physical etching.

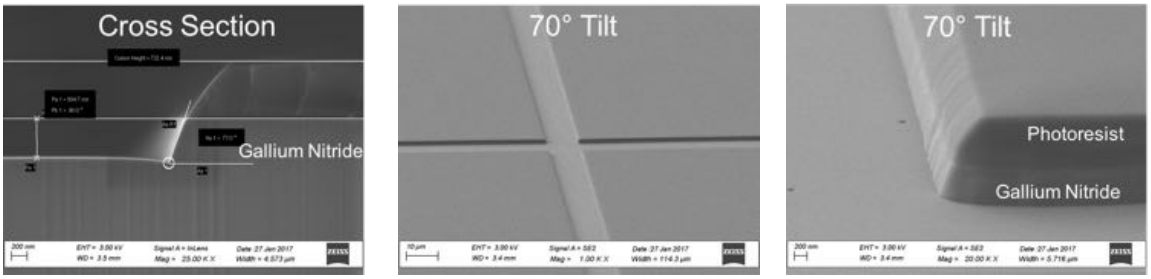

(a) Cross-Section of GaN etch sample

(b) 70° tilt view of the surface of GaN etch sample

(c) 70° detail tilt view of the surface of GaN etch sample

Figure 29: SEM of a GaN Etch sample

Figures 29 show cross sections of a test sample that were taken to validate the etching recipe. As is evident from the figure a sidewall angle between 70 and 75° can be expected when using a photoresist mask. This is sufficient for the formation of LEDs and Solar cells. Furthermore we find a uniformity within the wafer of 1.55%

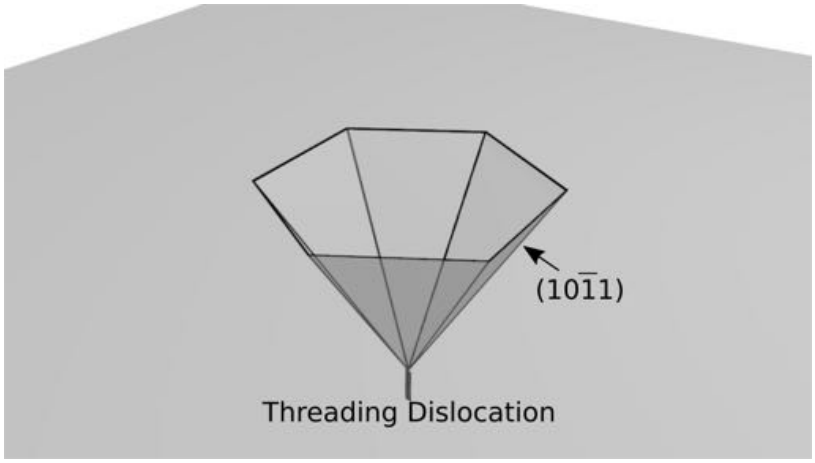

Figure 30: Anatomy of a V-Pit

and a wafer-to-wafer uniformity of 0.78%.

3.3 The role of V-Pits and V-Pit Passivation

V-Pits are volumetric voids visible on the surface of GaN and InGaN crystals after growth. They are often referred to as V-defects, but this can be a bit of a misnomer as the crystalline quality of the pits is pristine[133]. The pits form inverted pyramidal structures along the $\{1\,0\,\bar{1}\,1\}$ crystal planes as depicted in figure 30. Often the v-pits start from threading dislocations (TDs) in the crystal with a higher probability of formation for mixed TDs than pure edge TDs[133, 15]. This defect propagates because the growth rate on the $\{1\,0\,\bar{1}\,1\}$ plane is slower than the growth rate on the exposed $(0\,0\,0\,2)$ surface.

The effect of v-pits on solar cell performance is complex. On the one hand the v-pits provide a natural surface roughening that tends to promote internal light reflection analogous to the roughening done to high efficiency Si based solar cells[60]. This effect has been cited to increase the short circuit current of InGaN solar cells and thus improve performance[108, 134]. The v-pits also have an unwanted consequence of degrading the shunt resistance of the solar cell by providing a short-circuit pathway through the p-GaN[15].

3.3.1 Analysis of an unpassivated InGaN solar cell

In order to understand the effects of v-pits on bulk solar cell performance we used electrical, optical, and electron beam induced current or EBIC measurements to study a bulk InGaN/GaN heterojunction solar cell[15]. The structure and device design of the solar cell is shown in figure 31.

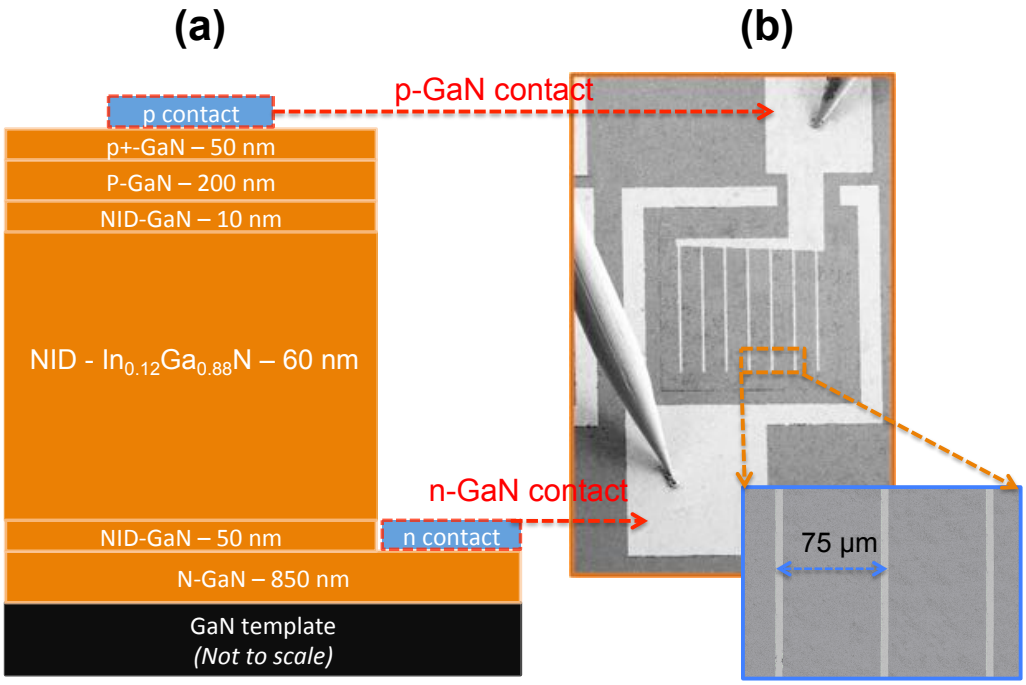

Figure 31: Bulk solar cell struct and device design[15]

In this device the p-GaN was grown at 800° C which preserves the absorber layer, but also leads to a high density of v-pits in the p-GaN layer. From SEM and AFM microscopy we can see that the v-pits typically range in size from 30–1000 nm in diameter. Since the v-pits form along crystal facets, we can estimate the v-pit depth from the diameter at the surface. We then define three areas of interest depending on the thickness of the top p-GaN layers: The first area is smooth and contains no v-pits, the second contains shallow v-pits (SVPs) which have a diameter less than 300 nm and do not penetrate the p-GaN layers and instead germinate somewhere within the p-GaN, and the third contains deep v-pits (DVPs) have a diameter greater than

300 nm and thus germinate somewhere in the InGaN layer or deeper. The v-pits appear to be distributed randomly on the surface of the sample and thus when we processed the sample into solar cells we found that the performance of the individual cells varied. We then correlated the electrical performance based on the density of SVPs and DVPs of 6 devices under illumination using a UV lamp.

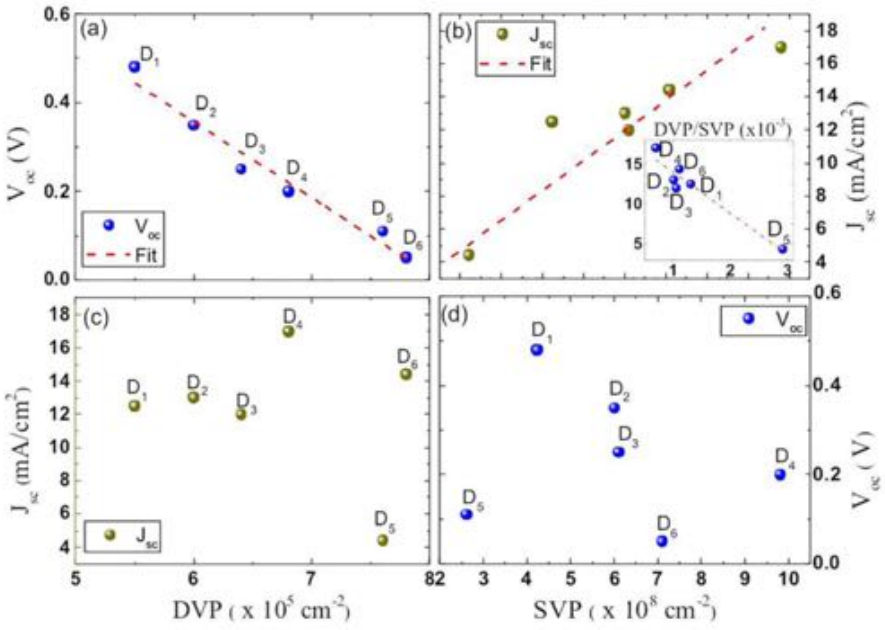

Figure 32: Correlation of DVP and SVP density with low V_{oc} and high J_{sc}[15]

As can be seen by figure 32 (a) and (c) as the density of DVPs increased the V_{oc} of the solar cells was reduced, but there was no discernible correlation between the DVP density and the J_{sc} of the solar cells. This supports the theory that deep v-pits tend to decrease the shunt resistance by providing a thinner pathway of lower resistance through the p-GaN. Figure 32 (b) suggests that as the density of SVPs increases there is a corresponding increase in the short circuit current, but as is shown in plot (d) of that same figure there seems to be no effect between the SVP density and

the V_{oc}. The J_{sc} enhancement with SVPs could, in part, be described by enhanced optical absorption in the material as a result of the textured surface as is suggested by Matioli *et al*, but we determined that this effect warranted further investigation[108].

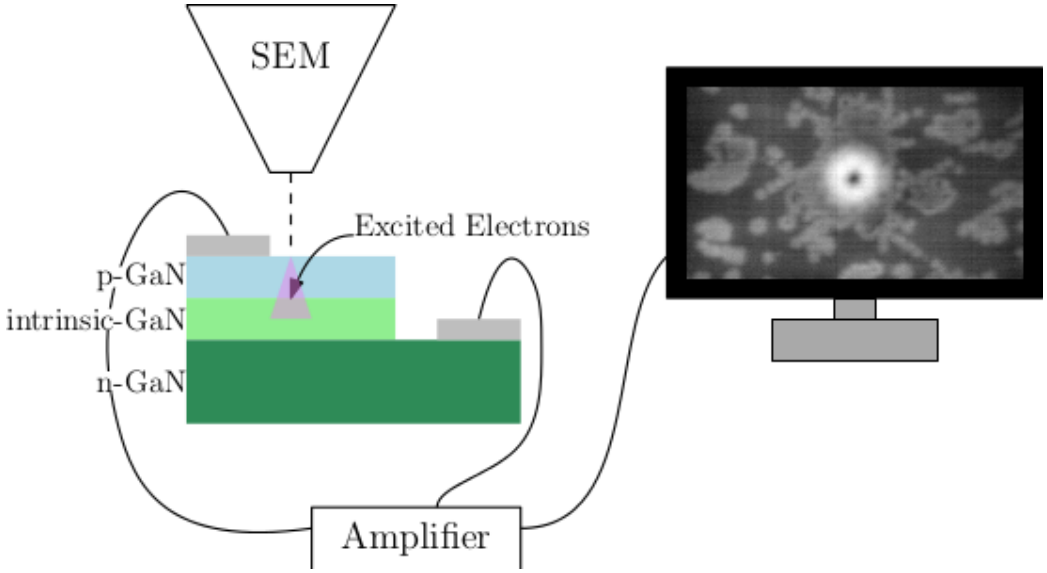

Figure 33: Schematic of the principle of electron beam induced current

Electron beam induced current, as shown in figure 33, is a way of imaging electric fields in a semiconductor. When the electron beam hits the material it will collide with the electrons in the material and excite some of them from the valence to the conduction band. Those electrons will then diffuse if they are not in the presence of an electric field, or will drift towards the contacts when there is an electric field like a pn junction present. Thus when the electron beam hits a junction there is a current signal, and when it hits the other components of a device there is no signal. EBIC is very useful for imaging junctions and defects in insulators and semiconductors.

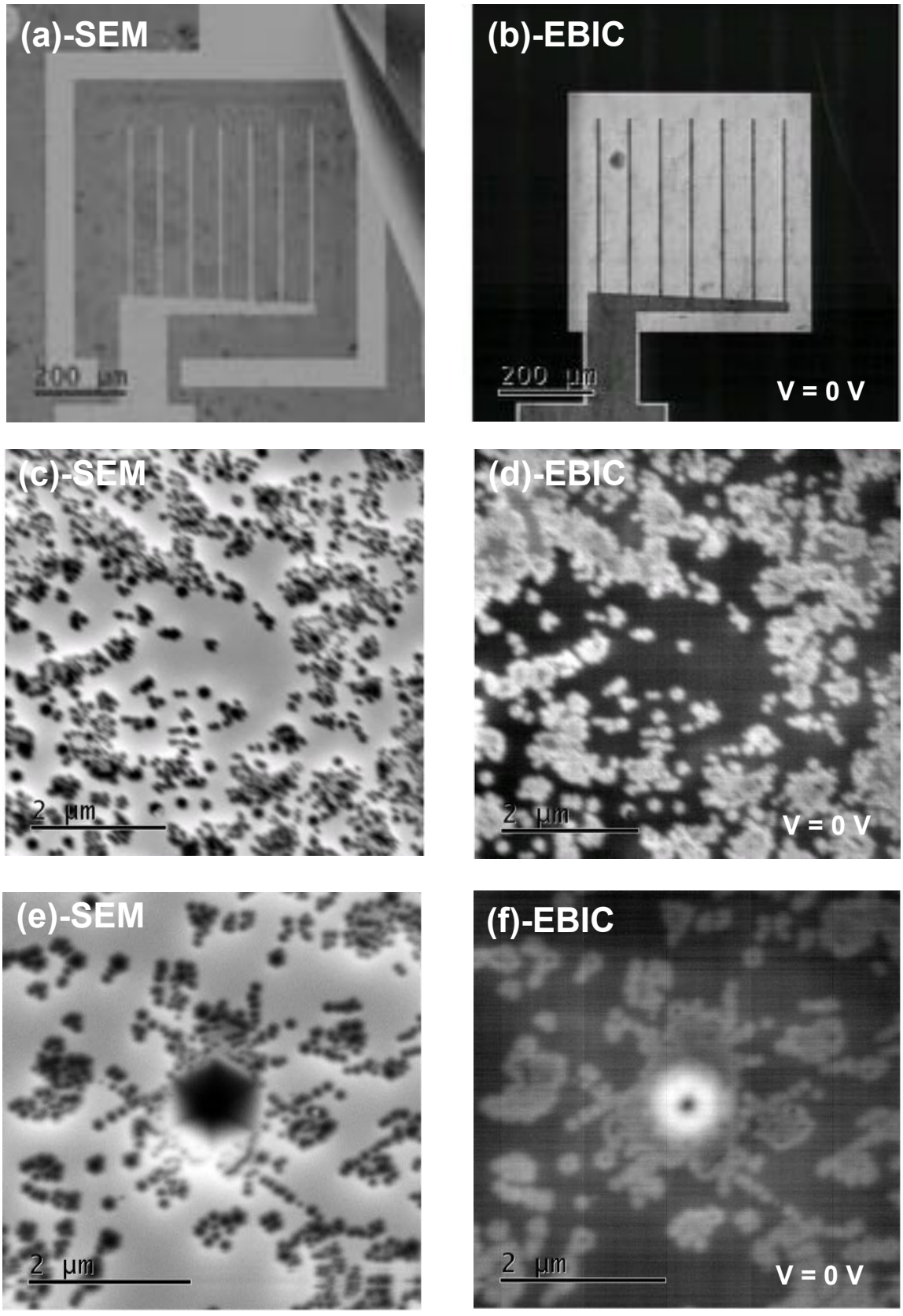

Figure 34: SEM (left) and EBIC (right) measurements showing inhomogeneous surface caused by v-pits resulting in similar inhomogeneous carrier collection[15]

In our case we can vary the depth of the penetration of the electron beam by changing the accelerating voltage of the SEM. When the signal is bright, that means that electrons are being collected from that region of the solar cell, but when the signal is dark there is no carrier collection. This can parallel carrier collection that is generated by exposure to solar radiation. As can be seen in figure 34 (e) and (f), the center of the deep v-pit shows no collection. This is what is expected if the v-pit serves as a channel for by-passing the junction and is consistent with our interpretation of figure 32 (a). There is another interesting phenomenon present in figures 32 and 34, and that is the effect of the edges of the VPs, especially the SVPs on carrier collection.

As is clear from figure 34 (d) the SVPs show an enhanced EBIC signal in comparison to the smooth areas that contain no v-pits. In figure 34 (f) there is an enhancement in collection from the edges of the v-pit even while the center is dark. This is evidence that the enhanced short circuit current of "rough" InGaN solar cells is a result of extra carrier collection as due to the presence of v-pits and not only due to better light-trapping. There is a strain-field associated with the formation of v-pits and this could act as a trap for impurities and defects, or indeed for the dopant atoms, which are themselves substitutional impurities[135, 136]. Furthermore GaN films have a high concentration of nitrogen vacancies (V_N) which act as compensating centers for the Mg, p-type doping and could be accommodated by the v-pits[137, 138, 139, 140]. All of these lead to an enhancement of the space-charge region around the v-pits which would increase carrier collection as demonstrated by the EBIC results and an enhanced short-circuit current in InGaN solar cells with a high density of v-pits.

3.3.2 Passivation of v-pits

Since the incorporation of v-pits seems to benefit the short-circuit current of InGaN bases solar cells, but degrades the V_{oc} an attempt was made to fill the v-pits with an

insulating material. Thus we sought to maintain their beneficial qualities to J_{sc} while increasing the resistance of the leakage pathway. The process settled upon was to use a spin on glass followed by etching. The thought was that after spin coating and curing a spin on glass could recover the film's smoothness. This smoothness would then assist during the etching step by carefully etching down to the surface of the p-GaN but leaving the glass in side the v-pits. Hydrogen silsesquioxane (HSQ) was chosen as the spin on glass because of its low viscosity was believed to aide in the filling of the v-pits, and because it was readily available.

HSQ is commercially available from DOW-Corning in a suspension that is either 1, 2, or 6%. The higher the percent of solid material the higher the viscosity and thus the thicker the resulting film. The chemical formula for HSQ can be written $HSiO_{3/2}$. HSQ is typically used as a negative tone resist for electron beam lithography as exposure to radiation tends to cause cross-linking which makes the film more difficult to remove in basic solution. There is also literature on the properties and use of cured HSQ as a spin-on glass[16, 17, **?**, 141]. In this case instead of cross-linking the resist using electron radiation various chemical reactions are promoted by annealing at different temperatures. Yang, *et al* break the annealing and chemical regimes into 4: room temperature–250° C, 250–350° C, 350–435° C, and > 435° C [**?**]. In the first regime the solvent is removed. In the second regime, 250–350° C, the following chemical reactions are promoted:

$$2\,HSiO_{3/2} \longrightarrow H_2SiO_{2/2} + SiO_{4/2}$$
$$H_2SiO_{2/2} + HSiO_{3/2} \longrightarrow SiO_{4/2} + H_3SiO_{1/2}$$
$$H_3SiO_{1/2} + HSiO_{3/2} \longrightarrow SiO_{4/2} + SiH_4$$

Then in regime 3, 350–435° C Si-H thermal disassociation and network redistribution occur:

$$4\,HSiO_{3/2} \longrightarrow 3\,SiO_{4/2} + SiH_4$$

$$SiH_4 \longrightarrow Si + 2\,H_2 \text{ or } SiH_4 \longrightarrow Si{-}H$$

Finally above 435° C the pore structure of the film collapses and the film shrinks[16, ?]. In the end a network structure that resembles SiO_2 is formed. The resultant film is an electrical insulator and has an optical index of refraction similar to glass with a typical value between 1.3 and 1.6 at 1550 nm[16]. These various stages of chemistry result in typical curing recipes for containing multiple steps. The recipe that we tested was reported by Holzwarth and Liou independently and involved four steps of increasing temperature and is shown in figure 35[16, 17].

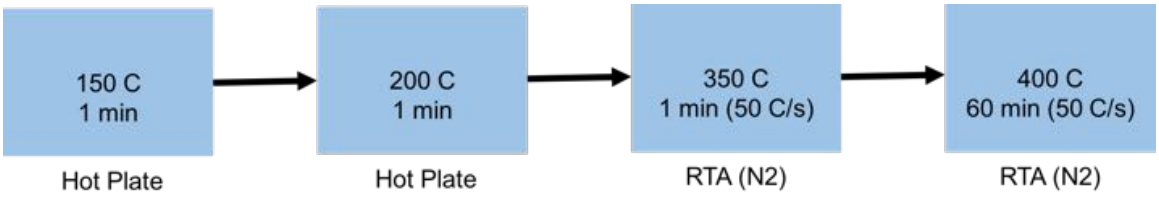

Figure 35: Recipe for HSQ curing adopted from [16, 17]

For our work we used 6% HSQ spun at 4000 rpm which results in a film of approximately 100 nm thick. In order to test the repeatability of the spin coating and determine the refractive index HSQ was spun on a number of sapphire wafers, cured, and measured in an ellipsometer. The expected index of refraction given by Holzwarth *et al* was 1.370 and our measured index of refraction was 1.353 which is in very good agreement[16]. The thicknesses of the films measured at 9 points by ellipsometer and the results are shown in table 7.

Table 7: Measured cured HSQ film thickness

	Thickness (nm)	Standard Deviation	Uniformity (%)
Sample 1	106	1.5	2.5
Sample 2	96	1.0	1.6
Sample 3	98	1.5	2.6

Thus the films are fairly uniform across the wafer (within 2.5%), and the average thickness was exactly 100 nm, which was expected. Furthermore, from wafer to wafer the results are consistent within a few nanometers, which falls below our accuracy for etching and is therefore satisfactory.

The next step was to etch the films. This is the necessary next step in recovering the p-GaN surface so that metal contacts can be formed. It was believed that chemical etching may be too fast to control accurately, and so our focus was on dry etching. Subsequent experience with cured HSQ or c-HSQ films has shown them to be fairly resilient to HCl and concentrated TMAH solutions and so this assumption may be worth revisiting in the future. Furthermore the high aspect ratio of the structures may slow the etching of the c-HSQ in dilute solution which is beneficial for our purposes. Additionally there is a risk of dry etch damage effecting the performance of the solar cells for two foreseeable reasons. First dry etch damage has been shown to compensate p-doping on the surface of III-Nitrides[124]. These effects can be countered to some extent by chemical or thermal treatments[124]. The second effect possible effect of dry etching is a result of the atmosphere used to etch the oxide–like film. Typical recipes for oxide etching use a mixture of tetrafluoromethane (CF_4) or other fluorine containing gasses and H_2. H_2 is necessary to the process for forming volatile etching by-products that can be exhausted from the reactor, but can also for Mg–H complexes

that tend to deactivate the p-dopant. The overall result is that it is likely that the p-GaN will be of lower quality if overexposed to dry etching. Thus it is crucial to dry etch to the p-GaN surface but no further.

First the etch recipe was investigated by varying the ICP and platen powers from 1000 W and 80 W to 900 W and 40 W respectively. The ICP power controls the formation of the plasma and by lowering the power the density of the plasma was expected to change. The platen power couples the plasma and the sample and by lowering the platen power less physical etching was expected which we hypothesized would cause less etch damage in the p-GaN. The etch rate did decrease when the platen power was decreased the film roughness increased substantially. By lowering the ICP power the etching results were inconsistent and non-uniform. Thus the original recipe was determined to be the best of the few recipes tested, and all further optimizations occurred using this recipe which is shown in table 8.

Table 8: SiO_2 Etch Recipe

Gas Flows (sccm)		Plasma Powers (W)			
H_2	CF_4	Source	Platen	Pressure (mTorr)	Backside Temp (° C)
60	60	1000	80	5	0

The Oxford ICP etchers on which this work was performed are equipped with an end-point detection apparatus. Using this system it is possible to measure the intensity of a variety of spectral lines formed by photon emission in the reaction by-products. Typically for SiO_2 or SiN_x on GaN the SiF_2 peak at 390 nm is analyzed. This peak is chosen as the majority of the Si in the reaction by-products comes from the oxide being etched and because it does not overlap with any of the spectral lines from He which is used for backing pressure and temperature control of the sample and may be present in the chamber. There were issues associated with analyzing

this peak, however, as in our case the majority of the SiF_2 signal came not from the c-HSQ on the sample, but from the carrier the sample was mounted on. Attempts were made to recalibrate the system for the Ga peak at 417 nm, but the signal was too weak to use for reliable end point detection at this time.

Instead we decided to characterize the etch rate of c-HSQ and control the etch thickness by varying the time. To investigate this we deposited HSQ on sapphire wafers and cured it, as previously discussed. After we characterized the HSQ thickness using ellipsometry. Finally we would etch the sample for various times to determine the etch rate using least squares linear regression weighted by the variance of the ellipsometry measurement. The resulting data are presented in figure 36 and the final value is 3.3 nm/s plus an offset of 14 nm due to the plasma start step of the etching.

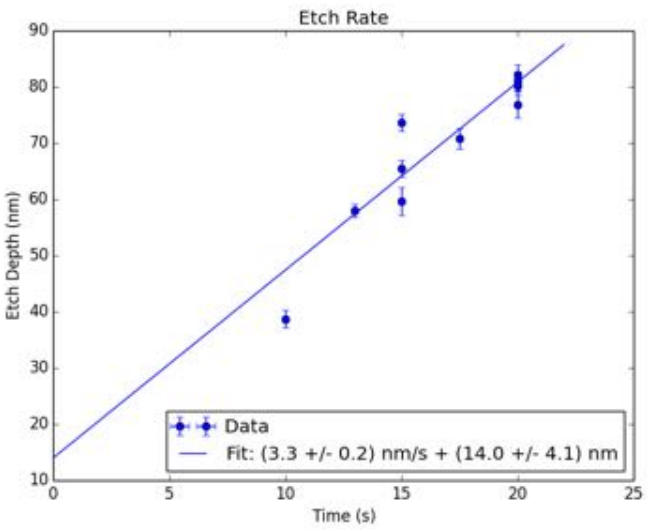

Figure 36: ICP etching rate determination for HSQ

The next step of our analysis was to see if the c-HSQ in fact filled the v-pits and whether or not the resulting c-HSQ film was smoother than the original v-pitted GaN film. To this effect we used some GaN/AlGaN/GaN HEMTs that had a high density of v-pits to test the c-HSQ filling and etching. Before we spin coated the HSQ we

analyzed the surface using a SEM and AFM. The results are shown in figure 37. We

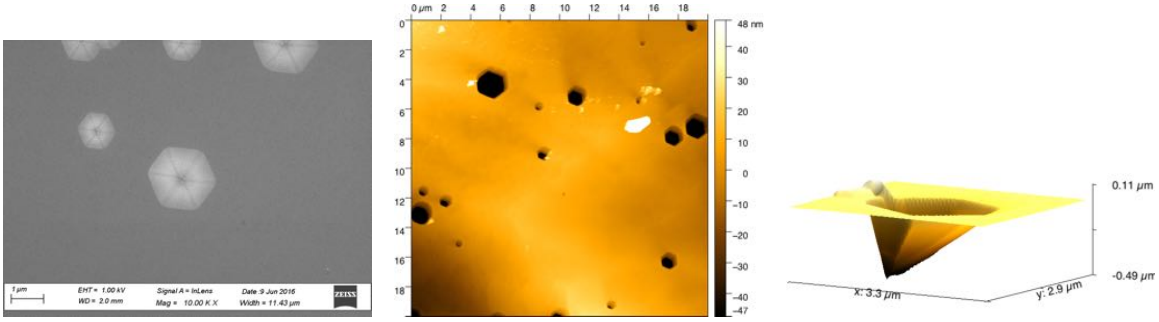

(a) SEM (b) AFM (c) 3D render of v-pit from AFM

Figure 37: SEM, AFM, showing v-pits before HSQ deposition, and a 3D detail of a v-pit showing the asymmetry of the AFM scan

can analyze the AFM data a little more rigorously if we keep in mind that the AFM tip is a wedge that cannot penetrate very deeply into the high aspect ratio v-pits as is shown in figure 38 (a–c). With this in mind we can plot the depth of penetration

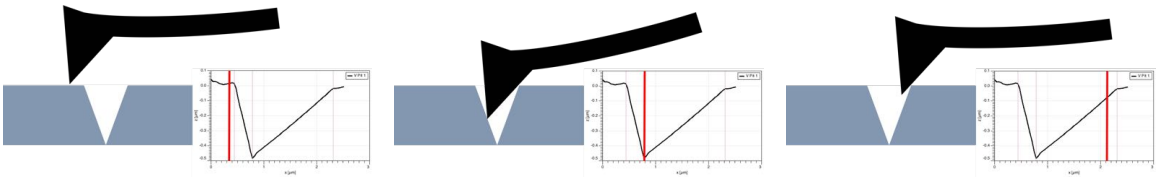

(a) AFM tip before vpit (b) AFM tip at maximum depth (c) AFM tip being removed from v-pit

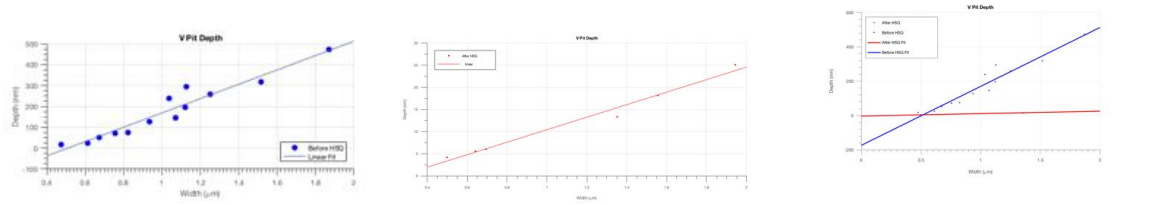

(d) AFM tip max penetration before HSQ (e) AFM tip max penetration after HSQ (f) AFM tip max penetration before and after comparison

Figure 38: (a–c) AFM tip penetration and (d–f) penetration vs width before and after HSQ

of the AFM tip *vs* the width of the v-pit before and after coating the sample with HSQ and curing the HSQ. This analysis is shown in figure 38 (d–f). This is a better metric than the rms roughness because we are interested in the coating properties of

the c-HSQ in and around the v-pits which is related to the wetting of the HSQ to the GaN surface as well as the film shrinkage during annealing and not the surface morphology of the HSQ film. From this analysis we can clearly see that the c-HSQ tends to smooth the surface above the v-pits.

In order to confirm the AFM finding and show that the c-HSQ filled the v-pits with out voids we cleaved the sample and examined it using cross-sectional SEM. Figure 39 shows that the c-HSQ fills the v-pit with a minimum of film shrinkage above the v-pit despite the depth of the v-pit being an order of magnitude thicker than the surface thickness of the c-HSQ.

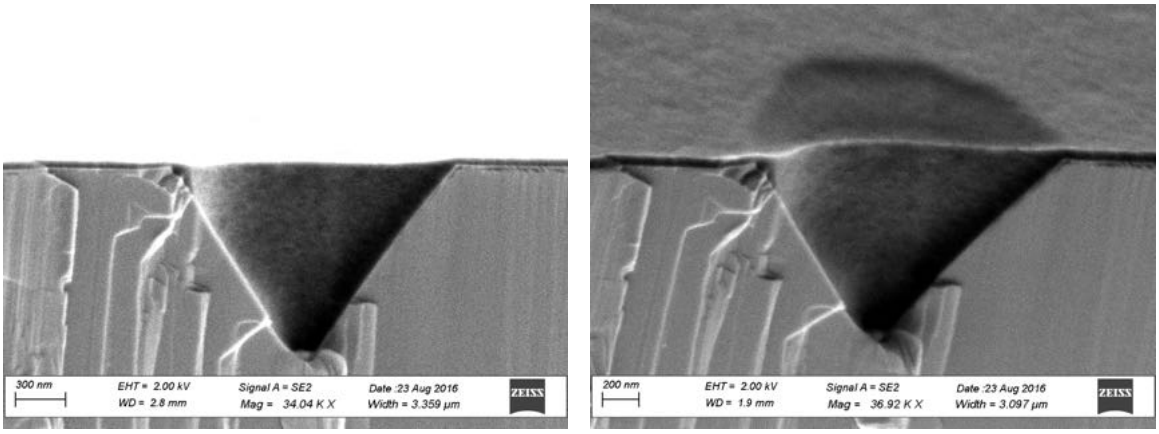

(a) SEM Cross-Section (b) SEM Cross-Section at a 60° Angle

Figure 39: Filled but unetched vpit

Finally we tested the sensitivity of the c-HSQ v-pits to over etching. In this experiment we coated HEMT samples with v-pits with HSQ and cured it. Then we etched the c-HSQ for 21, 24, 27, 30, 33, 36, 39, and 42 seconds. The resulting structures were imaged in the SEM, cleaved and the cross-section was imaged as well. The results of the experiment are shown if figure 40.

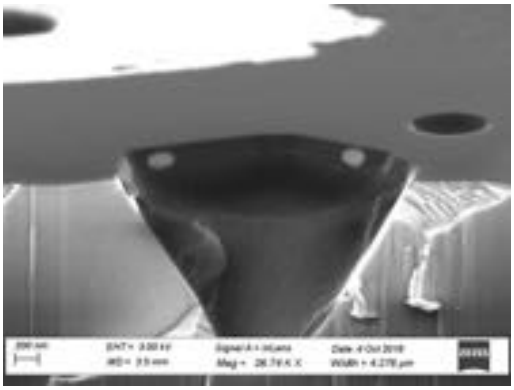

(a) 21s Etched

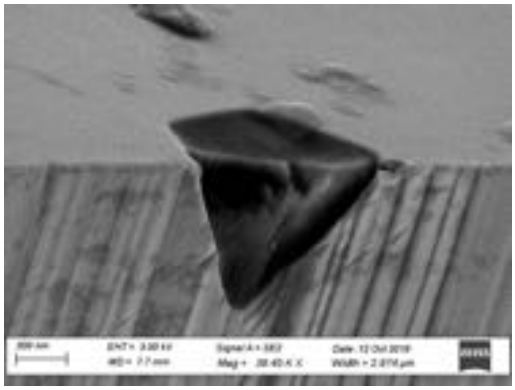

(b) 24s Etched

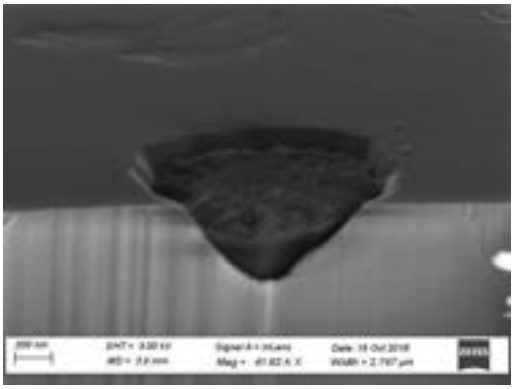

(c) 27s Etched

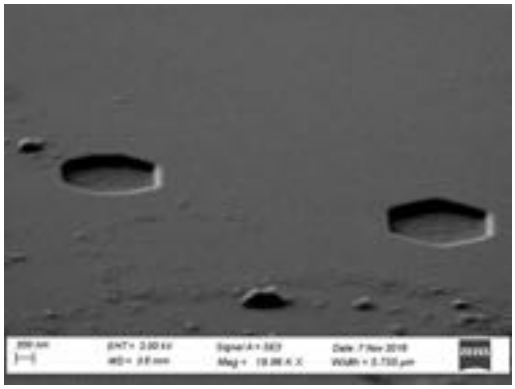

(d) 30s Etched

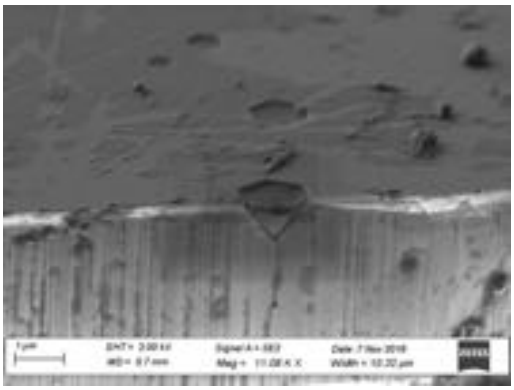

(e) 33s Etched

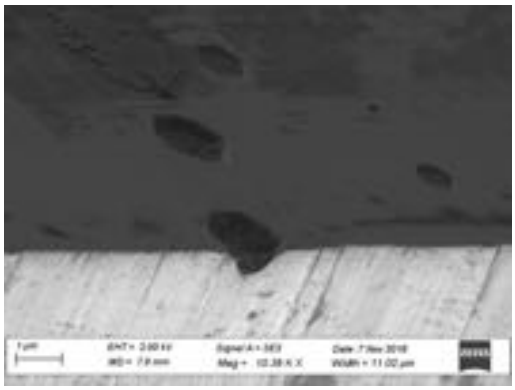

(f) 36s Etched

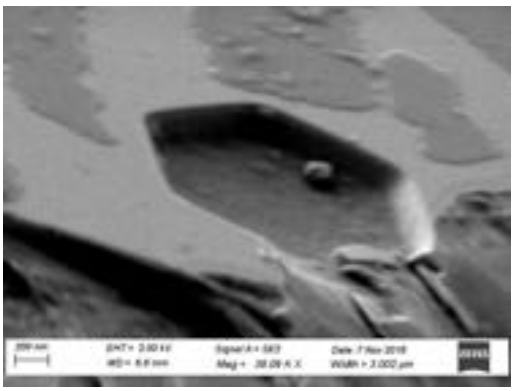

(g) 39s Etched

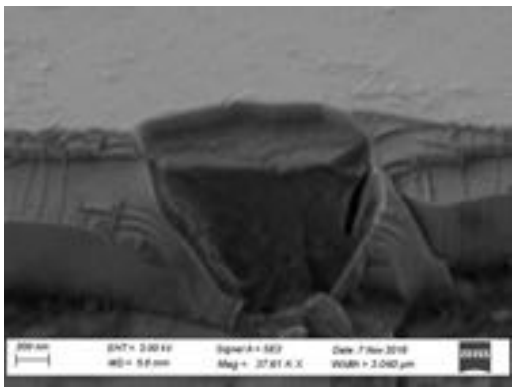

(h) 42s Etched

Figure 40: HSQ filled and etched vpits

It is clear from the images that the HSQ is etched on the surface and inside the v-pit to some extent, but etching in the v-pits seems to be fairly resilient as there is very little difference between 21 and 42s of etching. Furthermore the process more repeatable because the c-HSQ is only 100 nm thick on the surface and the v-pits that need to be masked are often twice as thick.

3.4 Metal–Gan Contacts

We address the work done on metal contacting of GaN. Since solar cells and LEDs are both PIN diode structures n-type and p-type contacts are required. N-type metal–semiconductor ohmic contact formation in GaN has not posed much of a problem. Typically low work function metals are used, and wide variety of metals can make ohmic, n-type contact to GaN. Metal to p-GaN ohmic contacts have been more difficult to achieve. Firstly high work function metals are required because GaN is a wide band gap semiconductor, and this narrows the selection of metals significantly. This is further compounded by the difficulty of p-doping GaN.

We investigate a variety of contacting schemes as well as recipes for achieving high quality metal–GaN contacts. Of chief concern is the resistance of the contacts in Ωs. A high contact resistance leads to a high series resistance for the solar cell and a degradation of the efficiency. This quantity is typically characterized by the specific contact resistivity, ρ_c, which is independent of the contact geometry and has units of $\Omega\cdot$ cm^2. The specific contact resistivity is equivalent to the change in voltage divided by the current density or:

$$p_c = \left(\frac{\partial J}{\partial V}\right)^{-1}_{V=0} \tag{42}$$

The various factors associated with specific contact resistivity are discussed below and several contacting schemes were investigated for both n and p-type GaN.

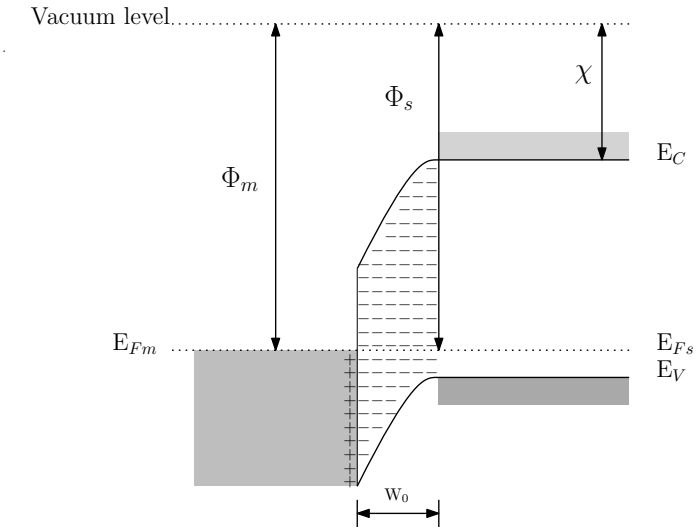

(a) Definition of Vacuum Energy, Metal, and Semiconductor Work Functions

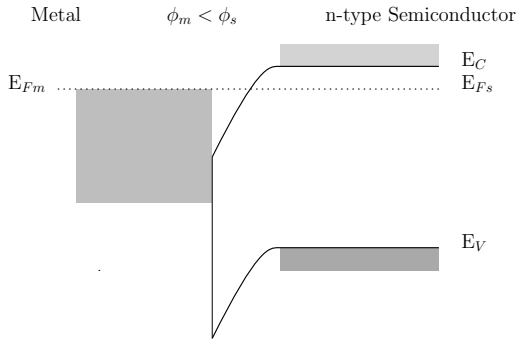

(b) N-type Ohmic Contact

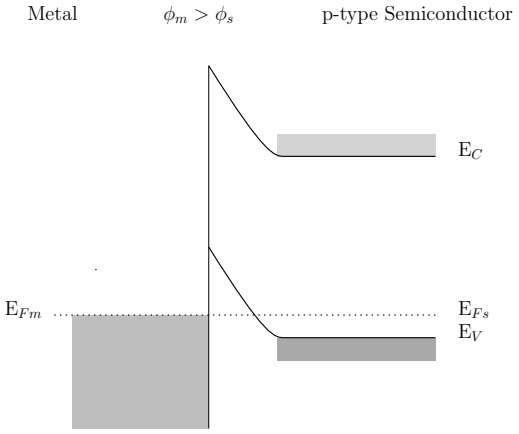

(c) P-type Ohmic Contact

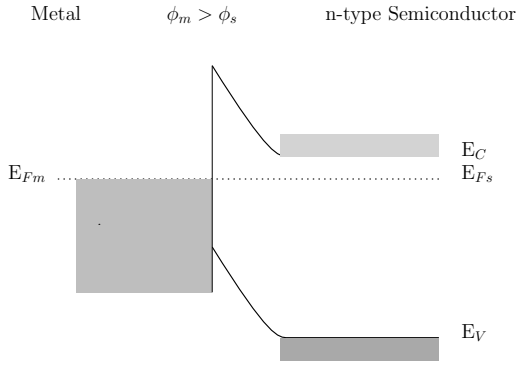

(d) N-type Schottky Contact

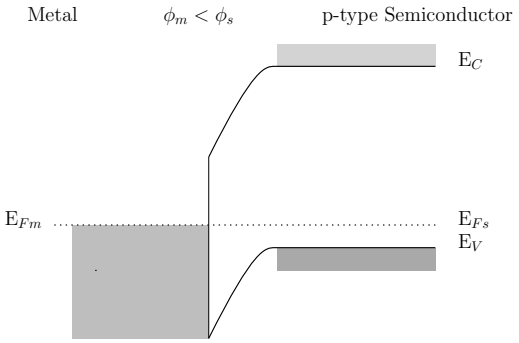

(e) P-type Schottky Contact

Figure 41: Ohmic and Schottky type Metal–Semiconductor junctions

When metals and semiconductors join to for a junction the work functions of the

two materials align. For ohmic contact to be achieved there is no barrier between the majority carriers and the metal so that the carrier "fall" into the metal and are collected with little resistance as is shown in figure 41 (b) and (c). In 41 (d) and (e) you can see that there is a barrier to electron collection in the n-type semiconductor and hole collection in the p-type semiconductor that is characteristic of Schottky contact. Schottky contacts have a diode–like electrical characteristic. This can be beneficial for HEMTs, Schottky diodes, and Schottky solar cells, but when contacting a PIN solar cell structure the additional diode will have detrimental effects on the EQE as carriers will recombine at the barrier and not be collected.

There are three carrier transport mechanisms that occur at the interface of Schottky contacts: thermionic emission, field emission, and thermionic field emission which is a combination of the two as demonstrated in figure 42. The relative proportion of

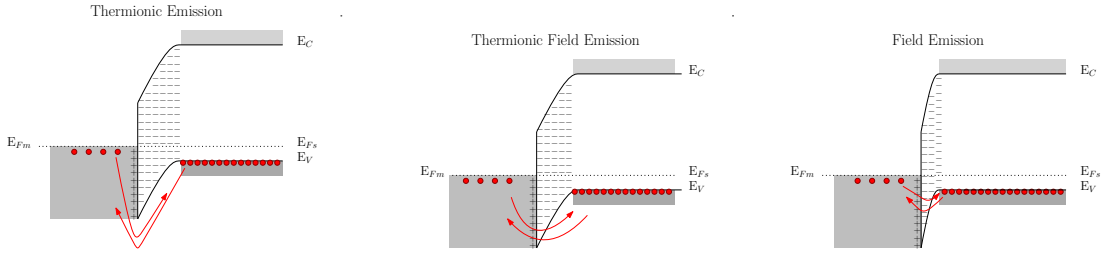

Figure 42: Carrier transport mechanisms in a p-GaN–Metal Schottky contact

these three mechanisms that occurs in a Schottky contact is defined by the width of the space charge region and the Schottky Barrier height as defined by $q\Phi_B = q\Phi_m - \chi$ for an n-type Schottky contact or $q\Phi_B = E_g - (q\Phi_m - \chi)$ for a p-type Schottky contact. Typically in low-doped GaN (N $< 1 \times 10^{17}$) thermionic emission dominates, in medium doped GaN (1×10^{17} <N $< 1 \times 10^{19}$) thermion field emission is the primary mechanism, and in highly doped GaN (N $> 1 \times 10^{19}$) field emission is the dominant method[5]. Thermionic emission occurs when hot carriers have the energy to overcome the Schottky Barrier, Φ_B. Field emission occurs when the barrier is narrow which allows for quantum tunneling to occur through the barrier. Thermionic–field

Table 9: Specific contact resistivity for different current transport mechanisms in Schottky contacts[5]

Thermionic Emission	$\rho_c = \frac{k}{qA-GT} \exp\left(\frac{q\Phi_B}{kT}\right)$
Thermionic Field Emission	$\rho_c \propto \exp \frac{\Phi_B}{E_{00} \coth\left(\frac{E_{00}}{kT}\right)}$
Field Emission	$\rho_c \propto \exp\left(\frac{\Phi_B}{\sqrt{N_{A/D}}}\right)$

emission is a combination of the two. The specific contact resistance of each mechanism is dependent on the Schottky barrier height, Φ_B, the doping concentration $N_{A/D}$, and the temperature. The dependance of the specific contact resistance for each of the mechanisms is summarized in table 9, where $A - G$ is the Richardson constant and E_{00} is a characteristic energy defined as:

$$E_{00} = \frac{qh}{4\pi}\sqrt{\frac{N_{A/D}}{\epsilon_r m^*}} \tag{43}$$

With ϵ_r and m^* equal to the relative permittivity and effective mass. As such to obtain low specific contact resistances either ohmic contacts are necessary, or a low barrier height and high doping concentration are necessary in Schottky contacts.

3.4.1 Transfer Length Method

Often the transfer length measurement method, or TLM method, is used to determine the specific contact resistance. We discuss in this section the TLM method as well as how this method was applied to the current work. Specifically this section may be used as a technical reference to the TLM_Analysis software that was written by the author and is available either by request, or on the shared computer at the Institut Lafayette.

In the TLM method contacts are formed on a semiconductor with varying distances between the two contacts. Typically linear or circular contact designs are used as is shown in figure 43. Linear TLMs are more simplistic to analyze, but suffer from

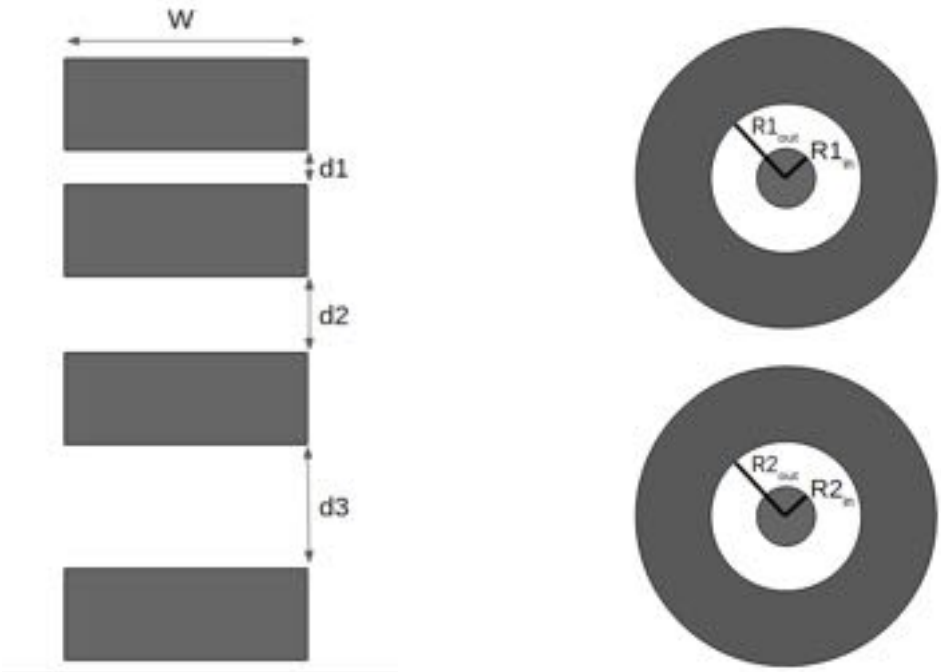

(a) Linear TLM (b) Circular TLM

Figure 43: Typical metal contact patterns for TLM measurements

the downside that edge effects may skew the data. For this reason it is important that $W >> d_i$ and that external to the the width W the material is either passivated or etched so that current is confined to flowing directly from one pad to the next. For simplicity we'll confine our discussion to linear TLM patterns where these criteria are satisfied. Four–probe measurements are used on each of the pads to characterized the current–voltage characteristics for each of the gaps, d1, d2, *etc.*. The resulting curves are fit to a linear model $I = V/R + b$. The parameter, b, should be very small (we are performing the measurements in the dark) but since we deal with physical data which can be noisy it is included because it increases the accuracy of the fit on the resistance and in a typical measurement it is 3–4 orders of magnitude less than the SMU range. This fitting is done my orthogonal distance regression and both the fit of the resistance in Ωs and the standard error of the fit are found for each of the the gap distances d_i.

In a typical measurement the resistance increases as the gap size increases as

shown by figure 44 which was a measurement done of linear TLM patterns on a p-GaN sample. The data is then again fit with a linear model using orthogonal distance

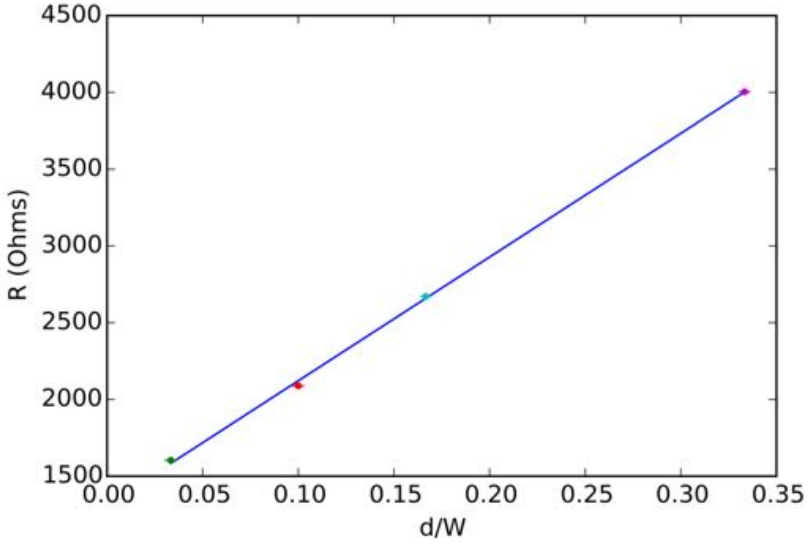

Figure 44: Typical linear TLM resistance vs d_i/W results of a p-GaN sample

regression weighted by the inverse of the variance of the resistance. In this way the less uncertainty there is in the resistance of a particular gap distance the more that gap will count in the curve fitting. The sheet resistance of the semiconductor can be deduced directly from the slope of the curve. In order to determine the specific contact resistance we have to consider the geometry of the contacts.

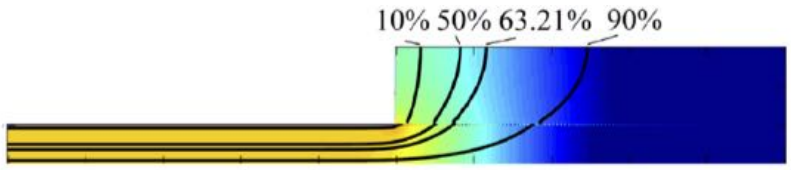

Figure 45: Current spreading under the edge of a contact on the surface of a semiconductor

Figure 45 show the typical geometry of a linear of current crowding at the edge of a contact. As can be seen the current density is uniform in between the two contacts, but it is not uniform under the contacts where it drops off exponentially from the edge of the contact as $I(x) \propto \exp\left(-\frac{x}{L_T}\right)$, where L_T is the average distance a carrier

travels under the contact before it is collected by the contact and is called the transfer length. Thus the effective contact area is $W \times L_T$, and we can write the resistance as a function of d the gap between two contacts as:

$$R(d) = \frac{R_{sh}}{W} d + 2\frac{R_{sh} L_T}{W} \tag{44}$$

We can also determine the specific contact resistance:

$$\rho_c = L_T^2 R_{sh} \tag{45}$$

The results for R_{sh}, L_T, and ρ_c are then obtained from the linear fit and the associated uncertainties from the standard errors of the fit. Analogously for circular TLM patterns we can write the total resistance as a function of the inner and outer radii as such:

$$R = \frac{R_{sh}}{2\pi}\left(\ln\frac{R_{\text{out}}}{R_{\text{in}}} + L_T\left(\frac{1}{R_{\text{out}}} + \frac{1}{R_{\text{in}}}\right)\right) \tag{46}$$

If all of the inner radii are equal we can further parameterize this equation by the gap between the inner and outer raddi, d:

$$R(d) = \frac{R_{sh}}{2\pi}\left(\ln\frac{R_{\text{in+d}}}{R_{\text{in}}} + L_T\left(\frac{1}{R_{\text{in+d}}} + \frac{1}{R_{\text{in}}}\right)\right) \tag{47}$$

This equation can easily be fit using non-linear regression methods like orthogonal distance regression. If both of the inner and outer radii vary however regression becomes difficult. Furthermore the experiment becomes more of a practical challenge as intuition is lost as to whether one gap size should have a higher or lower resistance than a previous gap size and experimental errors are more common. However we can parameterize the general equation by defining $A = \frac{1}{2\pi}\ln\frac{R_{\text{out}}}{R_{\text{in}}}$ and $B = \frac{1}{2\pi}\left(\frac{1}{R_{\text{out}}} + \frac{1}{R_{\text{in}}}\right)$ which depend on the known radii. Then we can rearrange to discover a linear relationship *vs* B/A:

$$\frac{R}{A}(B/A) = R_{sh}\left(1 + L_T(B/A)\right) \tag{48}$$

We can then find the values of R_{sh}, L_T, and ρ_c by plotting $\frac{R}{A}$ *vs* B/A.

3.4.2 Metal–N-type GaN Contacts

3.4.2.1 Common n-contacting schemes found in literature

Formation of ohmic metal–n-GaN contacts require the use of low work function metals. The use of metals like Ti (4.33 eV) or Al (4.26 eV) have been investigated[142, 143], but it was found that this lead to a series of problems. Firstly Ti tends to react with GaN to form TiN compounds resulting in voids in the GaN–Ti interface[144]. Al tends to insufficiently wet the GaN surface after high temperature annealing leading to droplet formation after annealing[145]. Also Ti and Al both can both oxidize, further increasing the resistance of the metal. Using Ti/Al bilayers tend to alleviate but not fix these problems.

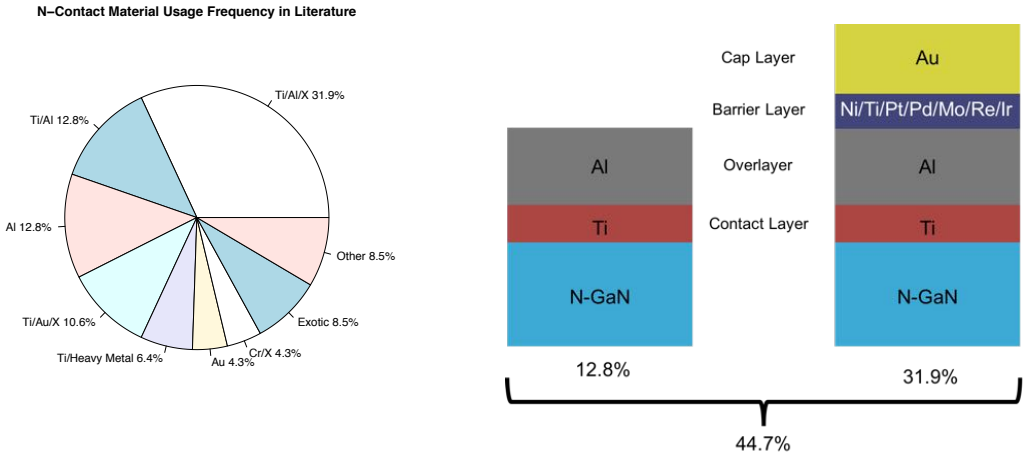

(a) Reported Metal Systems used for N-Contact (b) Primarily used Ti/Al and Ti/Al/barrier/cap contact schemes

Figure 46: Common metal/n-GaN contact systems described in literature

Instead what is now preferred for n-contact formation is a four layer metal stack as shown in figure 46 (b)[5]. Ti or Ta is preferred for the contact layer because it has good adhesion to the GaN as well as the possibility to form TiN or TaN. The formation of TiN or TaN increases the number of nitrogen vacancies, V_N, at the surface which act as donors at the interface and increases the local carrier concentration. Furthermore Ti has the ability to reduce the Ga_2O_3 native oxide that may be present, resulting

in a self–cleaning effect[146]. Al is the preferred metal for the overlayer because it has a low resistivity and because it can form low work function compounds with the other metals[5]. For the third layer or barrier layer a metal with a high melting point is used. This is so that during annealing the barrier layer can limit the reactions between the fourth and second metal layers. Finally the cap layer is primarily used to prevent oxidation of the other metal layers. Gold is typically employed for this task.

Reported specific contact resistances of between 10^{-2} and 10^{-7} Ω cm^2 have been reported. The lowest specific contact resistances are reported for contacts that are annealed around 850° C. While there is a significant reported trend showing the effect of annealing temperature on n-contact formation, there is no discernible trend between the specific contact resistance and the doping concentration of the n-type GaN and the annealed contact for concentrations between 5E17 and 5E18 cm^{-3}[5]. This is evidence that the contacts are ohmic. The difference between unannealed and annealed contacts is clear in this respect, as the unannealed contacts are strongly influenced by the doping concentration. Some believe that this is a result of a lower Schottky barrier height between TiN and n-GaN and other cite the high local doping caused by nitrogen vacancies[5].

Regardless of the mechanisms of ohmic n-type formation insights into the materials used, annealing conditions, and cleaning procedures commonly used in literature have proved invaluable in guiding the n-contacts used in this work.

3.4.2.2 Double Annealing of N-Contacts

In the formation of InGaN based solar cells both p-type and n-type contacts are required. As will be discussed in depth in the next section p-contact formation is challenging and achieving a high quality p-contact is essential to high performance solar cells. It is more common to form the n-contact first and then form the p-contact.

In this case the n-contact is made and annealed followed by p-contact formation and annealing. Thus the n-contact is annealed twice. We have studied the effect of double annealing on three different n-contacting schemes on identical LED samples.

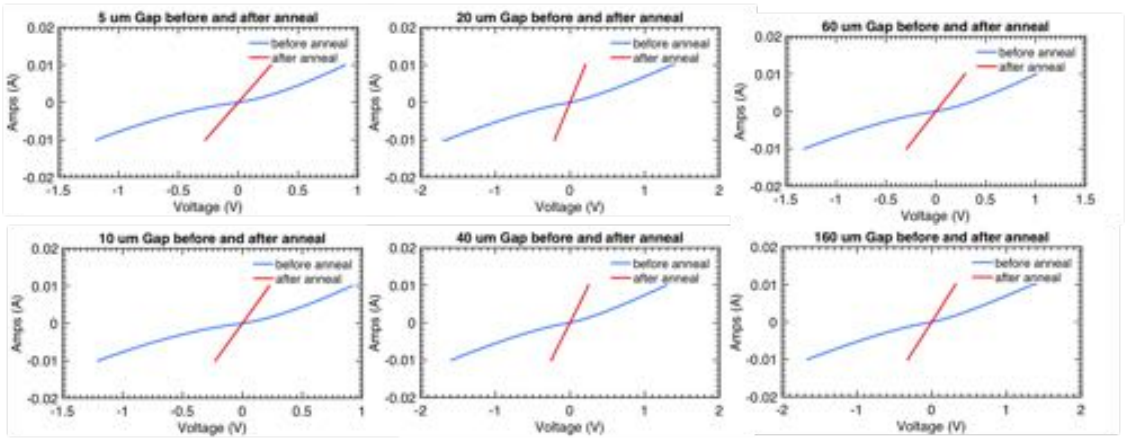

Figure 47: Ti/Al (20/20 nm) circular TLM contacts before and after annealing at

The first n-contact scheme investigated was to use Ti/Al (20/20 nm), annealed under nitrogen for ohmic n-contact formation and then annealed again under oxygen, this time for the ohmic p-contact formation. After the p-contact was formed the same bus bar would be deposited on both the p and n contacts. This bus bar consisted of Ni/Al/Ni/Au (25/200/25/25 nm). The Ni/Al/Ni/Au stack was supposed to have a low resistance as well as interface well with both the p-contact (Ni/Au) and the n-contact (Ti/Al). Figure 47 shows the effect of 60s annealing at 850° C under nitrogen atmosphere on the current–voltage characteristics of the contacts. As can be seen the resistance decreases significantly and the contacts go from having a Schottky behavior to displaying ohmic characteristics. However the surface morphology of the contacts

changed after annealing. This is because the Al has balled up during the annealing

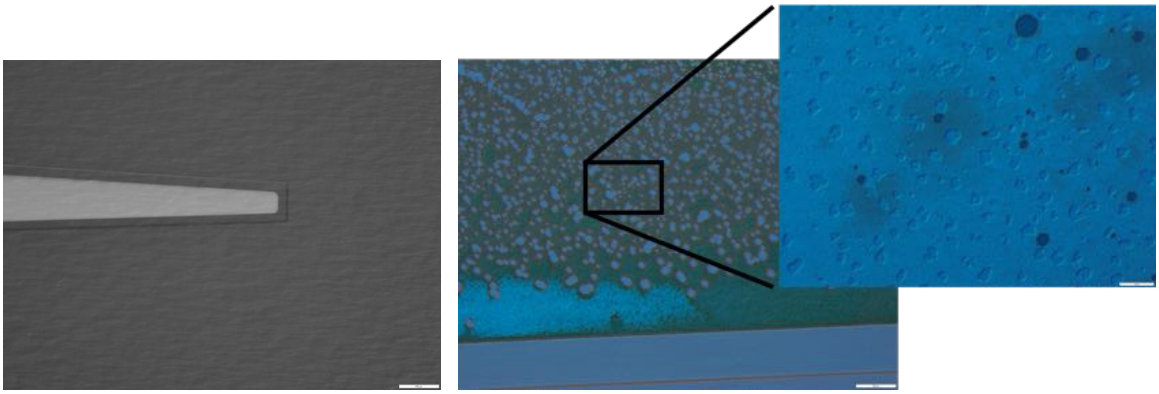

(a) Ti/Al contact before annealing (b) Ti/Al contact after annealing

Figure 48: Effect of annealing on Ti/Al n-GaN contacts displaying Al beads.

process. Furthermore when the samples were annealed a second time to form the p-contact there was a 3–4× increase in the contact resistance. We hypothesized that there could be due to two effects: first non-uniformity of the contact due to Al beading during n-contact annealing and oxidation of the Ti and Al during the p-contact annealing.

Instead of a two step process where the n-contact was formed followed by p-contact annealing and then bus bar deposition we tested a one step process where the n-contact and bus bar was deposited all at once. We tested both the previous device structure deposited all at once (Ti/Al/Ni/Al/Ni/Au, 20/20/25/200/25/25 nm) and a more traditional contact structure (Ti/Al/Ni/Au, 20/200/25/25 nm) as shown in figure 49.

Table 10: Results of Double Annealing on N-Contact Stacks

Figure of Merit	ρ_c (Ω cm^2) $\times 10^{-6}$		L_T (μm)		R_{sh} (Ω $\square$)	
Anneal	First	Second	First	Second	First	Second
Ti/Al/Ni/Al/Ni/Au	0.33 ± 0.24	6.1 ± 2.6	2.0 ± 0.5	6.3 ± 1.5	13.10 ± 0.03	14.8 ± 0.95
Ti/Al/Ni/Au	1.1 ± 0.5	1.2 ± 0.6	2.8 ± 1.0	2.9 ± 0.6	16.2 ± 0.4	12.9 ± 0.2

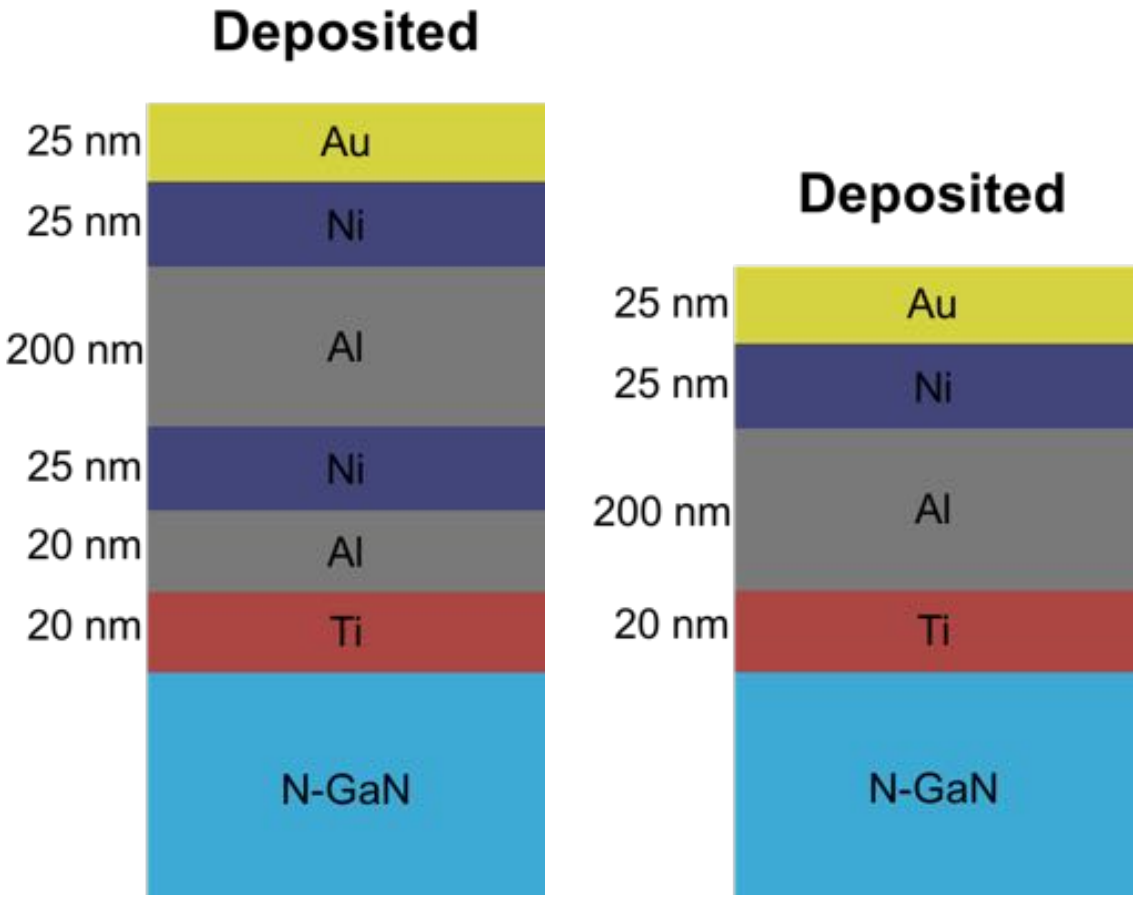

(a) N-Contact and Pad 1 (b) N-Contact and Pad 2

Figure 49: Cross-section of the two N-Contact/Pad schemes studied

The results of the two n-contact schemes are summarized in table 10. As one can see the transfer length (and thus specific contact resistance) of the first (Ti/Al/Ni/Al/Ni/Au) contact scheme increased from the first anneal to the second. The second contact scheme (Ti/Al/Ni/Au) shows no discernible degradation. This is evidence that the second, simpler scheme is more stable and is thus preferred for further processing.

3.4.3 Metal–P-type GaN Contacts

3.4.3.1 Common p-contacting schemes found in literature

Metal–p-GaN ohmic contact formation continues to be a challenge in InGaN LED and solar cell processing. This is due to several factors. Firstly GaN has an electron affinity of 4.1 eV and a band gap energy of 3.4 eV[147]. Thus it is difficult to obtain a

low Schottky barrier height Φ_B because typical values of metal work functions range from 4–5 eV. In addition to this issue the difficulty of doping GaN p-type means that it is difficult to achieve low specific contact resistance contacts. In order to address these issues annealed, complex metal stacks are utilized. this can reduce the effective metal/p-GaN barrier height and induce a localized increase of hole concentration. Figure 50 describes the frequency that various metal combinations are reported in literature[5].

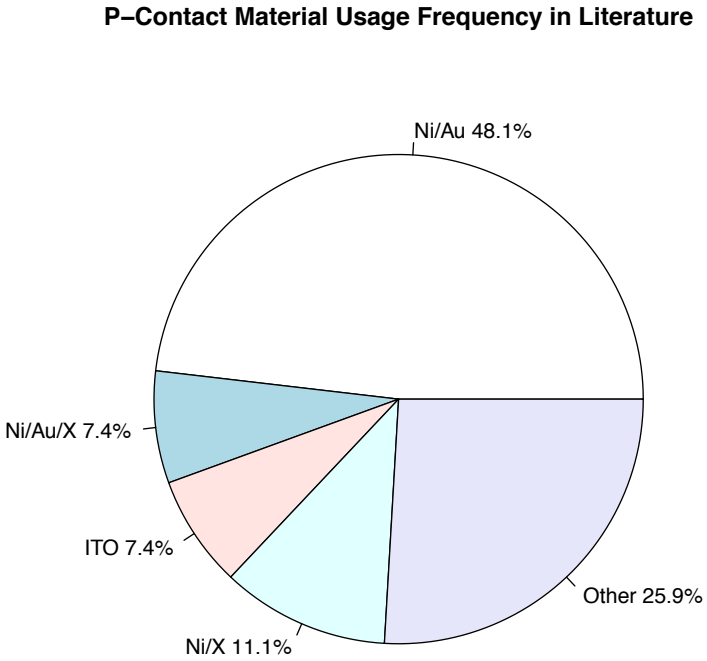

Figure 50: Commonly reported metal/p-GaN contacting systems

There is no apparent correlation between the work function of the metal and the specific contact resistance. This is because the electrical interface between the metal and the p-GaN is dominated less by the Schottky nature of the contact and more by a complex interaction between surface defects, the metallic species, and oxygen. As

50 shows the most reported metal contacting scheme to p-GaN, by a large margin is Ni/Au[5]. Furthermore, Ni/Au is the contact of choice for InGaN based solar cells because annealed, thin (5/5 nm) Ni/Au layers are semitransparent allowing transmission of up to 85% of incident light[122].

3.4.3.2 Ni/Au contact to p-GaN

One significant finding concerning Ni/Au contacts to p-GaN is that annealing the contacts in an oxygen containing ambient tends to decrease the specific contact resistance by an order of magnitude[5]. The role that oxygen plays in the formation of ohmic contacts is not well understood, however. Leading hypotheses are that NiO at the interface can be formed during annealing[148, 5, 149]. It has been reported that the NiO and p-GaN can form a contact with a low Schottky barrier height (0.19 eV)[150], but the height of this barrier has been contested by other sources and reported values as high as 2.28 eV[151]. The controversy about the Schottky barrier height of NiO/p-GaN makes it impossible to know what role, if any, the presence of NiO at the interface plays in the formation of ohmic contacts.

Another hypothesis about the role of oxygen in the formation of ohmic contacts arrises from the Mg–H complexes that can form and tend to strongly decrease the number of activated acceptors. This hypothesis states that during annealing with oxygen the Mg–H complexes can be disassociated and the oxygen containing atmosphere can reduce the hydrogen. This will increase the amount of free carriers in the p-GaN film and narrow the width of the Schottky barrier. Hull *el al.* demonstrate that an oxygen anneal does tend to decrease the amount of H contained in the p-GaN film[greco 100]. However, our own analysis has shown by Hall effect measurement that before and after annealing in oxygen there is no change in the number of carriers in the film. This is consistent with studies of contact annealing in Ar and N_2/O_2 atmospheres performed by Greco *et al.* in which there was no change found in the

doping concentration of the two samples[152].

Furthermore the studies by Koide *et al.* and Greco *et al.* showed that there was a decrease in Schottky barrier height for the sample annealed in N_2/O_2 (0.6–0.78 eV) compared to the sample annealed in N_2 or Ar alone (1.07 eV)[152, 148]. This decrease is consistent with the findings of Ishikawa *et al.* who found that the removal of a 2 nm insulator like the Ga_2O_3 native oxide would change the Schottky barrier height by 0.2–0.3 eV[153]. TEM and XRD analysis or Ni/Au contacts made to p-GaN that have been annealed either in Ar or N_2/O_2 ambient show that a Ni/Au solid solution as well as a NiO layer are formed under oxygen[149]. Specifically, under Ar atmosphere

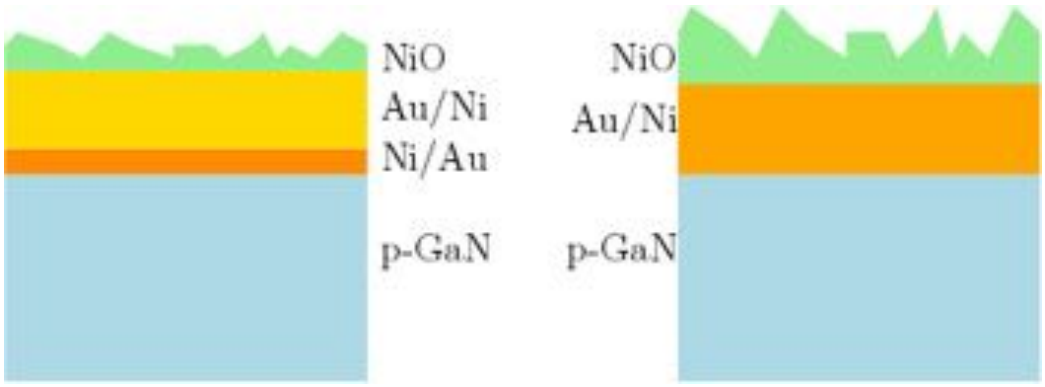

Figure 51: Schematic of TLM results on Ni/Au p-GaN contacts annealed in Ar (left) and N_2/O_2 (right)

there is a clear delineation between the Ni and Au layers after annealing. However when the same contacts are annealed under N_2 the Ni at the interface is no longer present and the XRD data that Ni has reacted with O_2 to form NiO on the surface as displayed schematically in figure 51[149]. This results in an apparent inversion sequence that has been referenced by several authors like Ishikawa *et al.*[153]. The belief is that Ni on the surface of the contact can reduce the native oxide and then diffuse into the Au contact resulting in a self-cleaning effect. Other Ni will form a solid solution with the Au layer and may out-diffuse and transform into NiO at the surface. The resultant out diffusion and NiO formation at the surface may be the cause of the apparent inversion sequence[5, 154].

Further bolstering the effect cleaning effect is the reported effect of surface treatments prior to contacting. Several cleaning recipes have been reported for use before making p-contact to GaN and these include the use of HCl:H_2O solutions diluted to various degrees, boiling KOH or aqua regia (HNO_3:HCl (1:3) solutions)[155, 5].

There are a lot of references regarding ohmic contact formation to p-GaN and much discussion and disagreement as to the mechanisms of the contacts. The most common recipes for ohmic contacts involve the use of HCl:H_2O (1:1) solution for cleaning followed by Ni/Au deposition and annealing under an oxygen containing atmosphere around 500◦ C. We used this recipe as a starting point for our own investigation of Ni/Au contacting to p-GaN.

3.4.3.3 Recipe Development for p-type Contacts

Several studies were performed on TLM structures on p-type GaN to determine both the stability of the contacts to process variations as well as the optimal recipe for metal–p-GaN contact formation. For solar cells the most frequently published scheme for p-contacting is the use of 5/5 nm Ni/Au contacts. When annealed these contacts are nearly transparent making them rather difficult to see in the probe station. Furthermore the thinness of the contact leads to considerable variability in the contact made with the probe station. This variability is caused by the mechanical contact of the probe scratching and removing the fragile metal contacts. Therefore for optimization purposes 10/10 nm Ni/Au contacts were used. In this study all of the samples were cleaned in a 1:1 solution of HCl (37.5%) and H_2O prior to depositing the metal contacts. The metal contacts were all deposited by electron beam evaporation. The evaporation tool has a quartz crystal microbalance (QCM) that is used to determine the deposition rate and total thickness of the film. The crystal is a piezoelectric resonator whose resonant frequency is intimately related to the mass and stiffness of the surface of the crystal. As the metals are deposited on the sample they are also

deposited on the QCM and we can determine the mass loading of the resonator. Since we know the typical density of the metal and area of the QCM we can deduce the thickness of the film deposited with a high degree of accuracy and repeatability. The first parameters optimized were the annealing temperature and time. This study is shown in figure 52. We obtain the data by measuring linear TLM patterns on 540

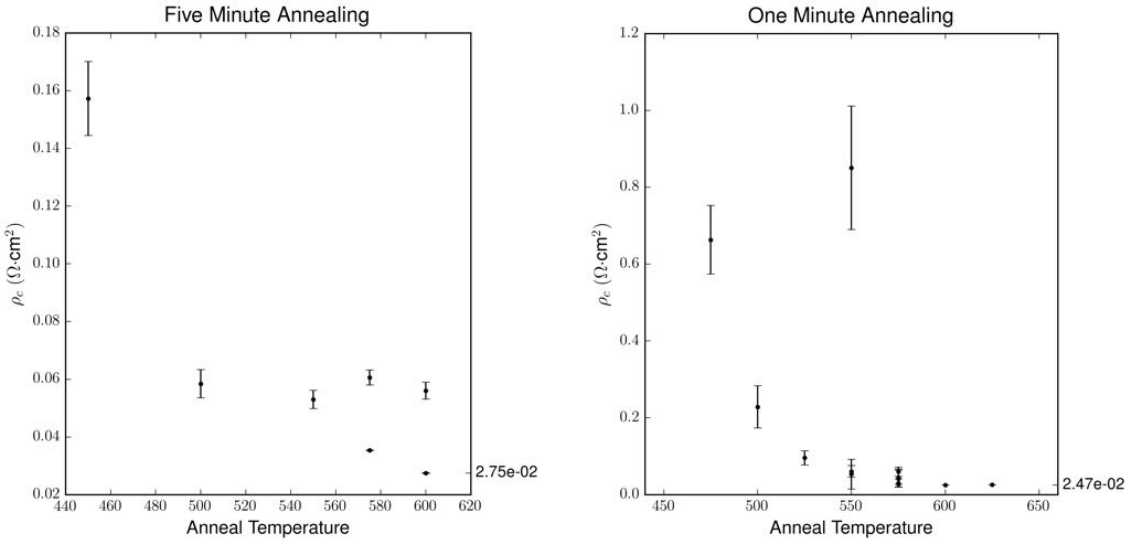

Figure 52: Change in Ni/Au (10/10 nm) p-contact specific contact resistance with temperature for one (right) and five (left) minute annealing under O_2

nm p-type GaN (doping concentration between 3–6$\times 10^{17}$ cm^{-3}). The TLM patterns had gap sizes of 10, 20, 30 50, and 100 μm and a width of 300 μm. While there is no etching or passivation of the linear TLM patterns outside of the pattern area we found a good linearity of the patterns. We estimated a very low systematic uncertainty by as a result of the lack of etching by excluding the largest gap size (100 μm) from the analysis and comparing this value to results obtained with the largest gap size. There was no significant difference between the two measurements. We believe this to be a meaningful estimation of the systematic uncertainties due to the lack of passivation because electrical measurements of the pattern with the largest gap width will be the most effected by passivation. There is a clear trend that in both the one minute annealing and five minute annealing require temperatures higher than about

520° C to obtain moderate specific contact resistances. Furthermore the minimum values, 0.0275 and 0.0301 Ω cm^2 for five and one minute annealing respectively, are very similar. Also for one minute annealing at 575, the value that provided the lowest ρ_c for that time we see a high degree of repeatability from sample to sample.

Since we were able to achieve moderate values of specific contact resistance (on the order of 1×10^{-2} as opposed to state of the art which is on the order of 1×10^{-4} to 1×10^{-6}) with a high degree of repeatability we decided the next effect to study was the ratio between the Ni and Au species. As such we formed metal contacts with thicknesses of 8/12 nm and 12/8 nm Ni/Au. The results of the study (figure 53) show no discernible effect of the various Ni and Au ratios.

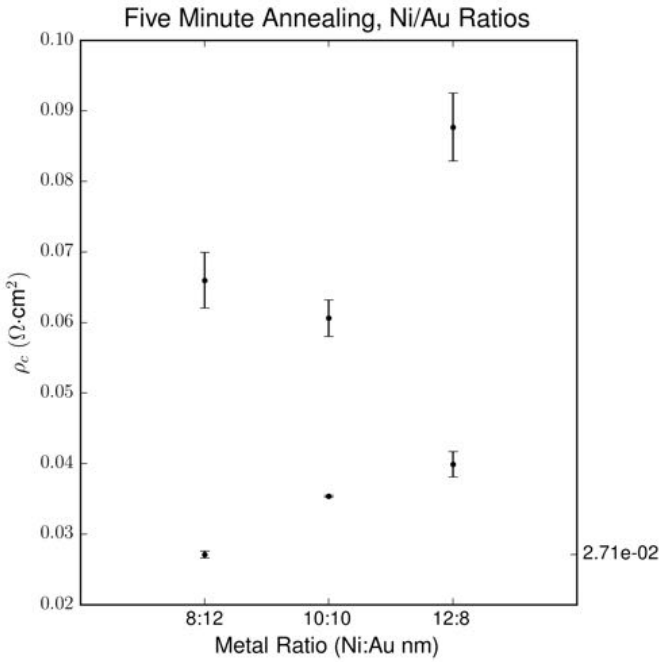

Figure 53: Specific contact resistance vs Ni:Au ratio

We then turned our attention to the sample preparation. As has been previously reported by Chary, *et al.* there is a strong correlation between the specific contact resistance and the concentration of HCl used to clean the substrate prior to metal

deposition[155]. We first used standard organic cleaning (acetone followed by isopropyl alcohol followed by DI-H_2O) to descum the sample. After organic cleaning we used a bilayer photolithography process with LOR-3b and SC1813 photoresists to form the TLM patterns. We attempted to replicate the result of Chary, *et al.* by cleaning the sample in a HCl:H_2O ranging in dilution ratios of 1:1, 2:1, 3:1, and 1:0 or pure concentrated HCl (37.5%)[155]. We found that HCl cleaning after photolithography did not degrade the bilayer photoresist and the hope is to impede potential native oxide growth by limiting the time between the acid cleaning and the beginning of metal deposition. Chary, *et al.* reported that they cleaned their samples for 10 mins in the various solutions at room temperature. We replicated this and also attempted a 5 minute cleaning process. Following metal deposition the photoresist and excess metal was removed in a commercially available liftoff tool using pressurized DMSO and annealed for one minute in an oxygen ambient at 575° C. The results in figure 54

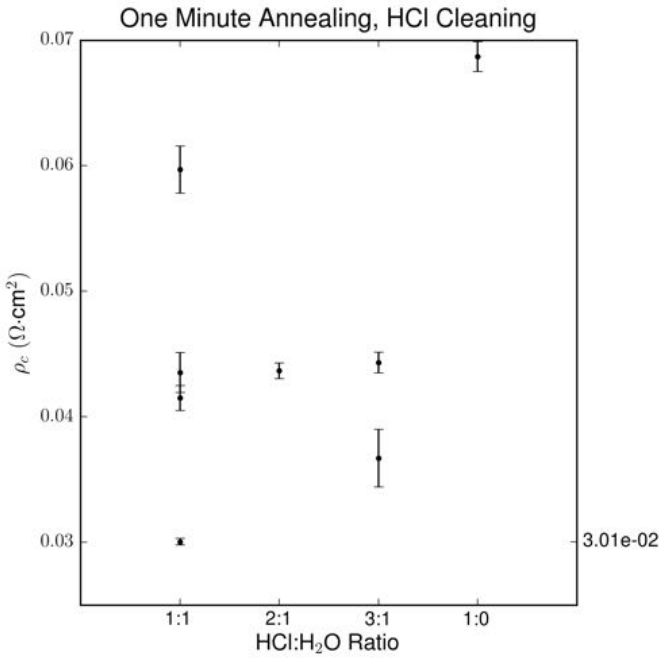

Figure 54: Specific contact resistance vs HCl:H_2O ratio

show no effect of the various cleaning solutions. The only effect we found was that

for one of the samples cleaned in pure HCl the surface of the contacts after metal metal deposition and liftoff was degraded and ohmic contact could not be achieved. Otherwise, no correlation between the cleaning solutions and the specific contact resistance can be determined. This may be because some as yet undetermined variable in the process overshadows the effect of the cleaning and leads to a specific contact resistance between 0.03 and 0.04 Ω cm^2. On the other hand the reported effect of cleaning is high (3×10^{-2} Ω cm^2 to 3×10^{-4} Ω cm^2 by just changing the HCl:H_2O ratio), and we simply do not see that in our results[155].

We have also analyzed the effect of annealing the p-GaN in oxygen prior to metal contact deposition ($\rho_c = (8.5 \pm 1.1) \times 10^{-2}$ Ω cm^2), and annealing 8/12 nm Ni/Au films at 600° C ($\rho_c = (2.45 \pm 0.22) \times 10^{-2}$ Ω cm^2), but again the results show very little change in the specific contact resistance. A summary table of all the metal p-GaN contact measurements is shown in table 11.

Table 11: Summary of Ni/Au – p-GaN Studies and Results

	Hall Effect Measurement		Annealing		Contact (Ni/Au)	Cleaning		TLM Measurement Results		
Sample	Doping (cm^{-3})	R_{sh} (Ω $\square$) $\times 10^3$	Temp ($^\circ$ C)	Time (s)	Ni:Au Ratio	Time (min)	HCl:H_2O ratio	ρ_c (Ω cm^2) $\times 10^{-2}$	R_{sh} (Ω $\square$) $\times 10^3$	L_T (μm)
A-IL-045-0073-2	6.60	7.87	500	300	10/10	5	1:1	5.8 ± 1.5	8.345 ± 0.8493	26.4 ± 4.44
A-IL-045-0073-3	6.60	7.87	550	300	10/10	5	1:1	5.3 ± 0.9	7.516 ± 0.536	26.6 ± 3.1
A-IL-045-0073-4	6.60	7.87	600	300	10/10	5	1:1	Not Ohmic	–	–
A-IL-045-0073-6	6.60	7.87	450	300	10/10	5	1:1	16 ± 4.1	8.002 ± 0.792	44.3 ± 7.1
A-IL-053-0081-1	3.30	13.89	475	60	10/10	5	1:1	Not Very Ohmic - 66.3 ± 11.2	7.68 ± 250	89.9 ± 8.3
A-IL-053-0081-2	3.30	13.89	500	60	10/10	5	1:1	22.8 ± 3	7.08 ± 0.45	56.9 ± 5.2
A-IL-053-0081-3	3.30	13.89	525	60	10/10	5	1:1	9.57 ± 0.43	6.89 ± 0.09	37.2 ± 0.8
A-IL-053-0081-5	3.30	13.89	550	60	10/10	5	1:1	6.03 ± 0.25	7.14 ± 0.09	29.1 ± 0.7
A-IL-053-0081-6	3.30	13.89	575	60	10/10	5	1:1	5.97 ± 0.0019	6.84 ± 0.08	29.5 ± 0.5
A-IL-054-0082-1	–	–	550	60	10/10	5	1:1	5.33 ± 0.3	7.54 ± 0.29	26.6 ± 1.3
A-IL-054-0082-2	–	–	600 pre + 550	300 + 60	10/10	5	1:1	8.55 ± 1.13	4.79 ± 0.14	42.2 ± 3.5
A-IL-054-0082-3	–	–	550	60	10/10	5	1:1	85 ± 2.06	8.43 ± 0.46	98.4 ± 12.4
A-IL-054-0082-4	–	–	575	60	10/10	5	1:1	3 ± 0.03	10.1 ± 0.4	17.2 ± 0.2
A-IL-054-0082-5	–	–	500	300	10/10	5	1:1	Bad Measurement	–	–
A-IL-054-0082-6A	–	–	575	300	10/10	5	1:1	6.06 ± 0.26	6.36 ± 0.16	30.9 ± 1.1
A-IL-054-0082-6B	–	–	600	300	10/10	5	1:1	5.6 ± 0.3	6.27 ± 0.06	29.8 ± 9
A-IL-054-0082-6C	–	–	575	300	8/12	5	1:1	6.6 ± 0.4	7 ± 0.08	30.7 ± 1.1
A-IL-054-0082-6D	–	–	575	300	12/8	5	1:1	8.77 ± 0.0048	6.99 ± 0.17	35.4 ± 1.3

	Hall Effect Measurement		Annealing		Contact (Ni/Au)	Cleaning		TLM Measurement Results		
Sample	Doping (cm^{-3})	R_{sh} (Ω $\square$) $\times 10^3$	Temp ($^\circ$ C)	Time (s)	Ni:Au Ratio	Time (min)	HCl:H_2O ratio	ρ_c (Ω cm^2) $\times 10^{-2}$	R_{sh} (Ω $\square$) $\times 10^3$	L_T (μm)
A-IL-055-0083-1A	6.60	7.87	575	300	10/10	5	1:1	3.53 ± 0.01	3.8 ± 0.01	30.5 ± 0.1
A-IL-055-0083-1B	6.60	7.87	600	300	10/10	5	1:1	2.75 ± 0.01	3.98 ± 0.03	26.2 ± 0.1
A-IL-055-0083-1C	6.60	7.87	575	300	8/12	5	1:1	2.71 ± 0.05	4.29 ± 0.04	25.1 ± 0.3
A-IL-055-0083-1D	6.60	7.87	575	300	12/8	5	1:1	3.99 ± 0.18	4.14 ± 0.04	31 ± 0.9
A-IL-055-0083-1E	6.60	7.87	600	300	8/12	5	1:1	2.45 ± 0.22	4.23 ± 0.11	24.1 ± 1.4
A-IL-055-0083-3A	6.60	7.87	575	60	10/10	5	1:1	4.35 ± 0.16	3.78 ± 0.02	33.9 ± 0.6
A-IL-055-0083-3B	6.60	7.87	575	60	10/10	5	2:1	4.37 ± 0.06	3.81 ± 0.03	33.9 ± 0.3
A-IL-055-0083-3C	6.60	7.87	575	60	10/10	5	3:1	4.43 ± 0.08	3.85 ± 0.02	26.4 ± 7.7
A-IL-055-0083-3D	6.60	7.87	575	60	10/10	5	1:0	Not Ohmic	–	–
A-IL-055-0083-4A	6.60	7.87	575	60	10/10	10	1:1	4.15 ± 0.1	3.65 ± 0.03	33.8 ± 0.5
A-IL-055-0083-4B	6.60	7.87	575	60	10/10	10	3:1	3.67 ± 0.23	3.74 ± 0.02	31.3 ± 1.1
A-IL-055-0083-4C	6.60	7.87	500	600	10/10	10	3:1	3.74 ± 0.01	3.94 ± 0.29	30.9 ± 1.1
A-IL-055-0083-4D	6.60	7.87	575	60	10/10	10	1:0	6.87 ± 0.12	3.5 ± 0.0	44.3 ± 0.4

3.4.4 Effect of P-Contact Thickness and Area on LED performance

For the first LEDs and solar cell that we processed we used a p-contact that was Ni/Au (5/5 nm) as this was the most common thickness used for solar cells[5]. In studying the electrical characteristics and electroluminescence (EL) of LEDs we found an interesting pattern as shown in figure 55.

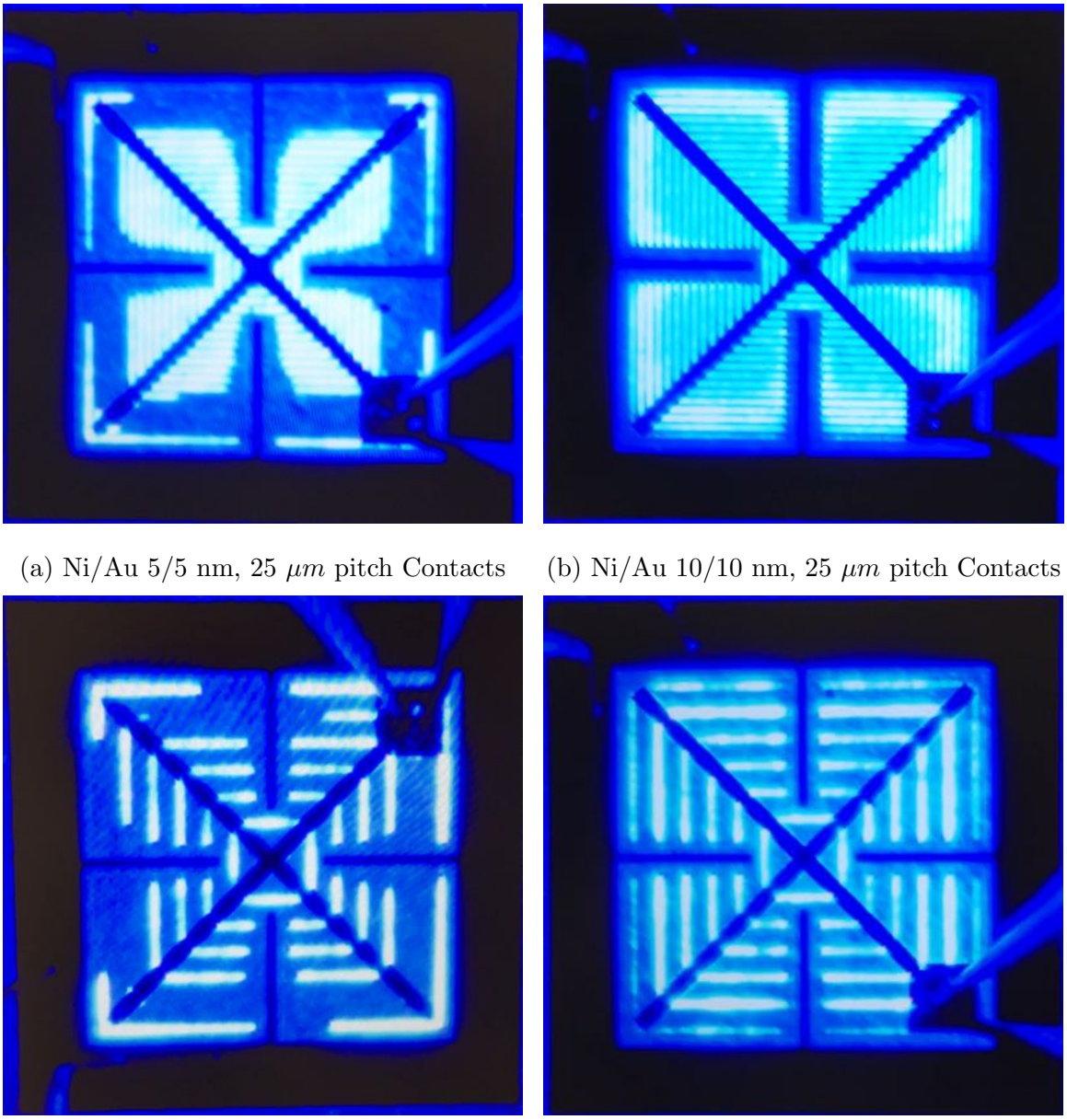

(a) Ni/Au 5/5 nm, 25 μm pitch Contacts

(b) Ni/Au 10/10 nm, 25 μm pitch Contacts

(c) Ni/Au 5/5 nm, 75 μm pitch Contacts

(d) Ni/Au 10/10 nm, 75 μm pitch Contacts

Figure 55: Effect of contact thickness on EL uniformity

Thicker contacts result in a more uniform EL from the LED samples. In order to see if the thin contacts were damaged we examined them in the SEM. as shown in figure 56.

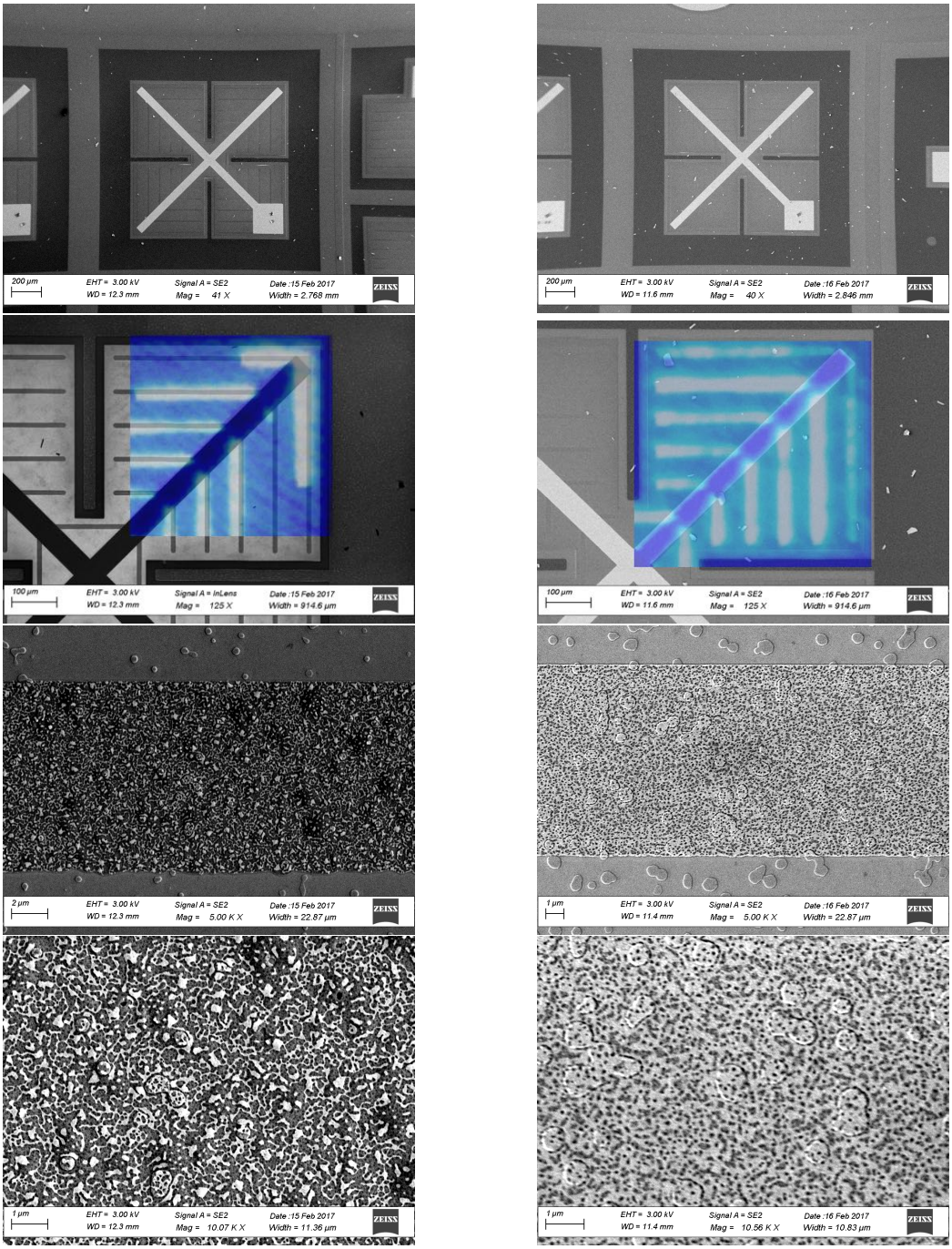

(a) 5/5 nm Ni/Au Contact

(b) 10/10 nm Ni/Au Contact

Figure 56: Effect of contact thickness on morphology

There are no visible breaks or damage in the thinner contacts, however there is a clear change in the morphology of the contact. The thinner, 5/5 nm Ni/Au contacts seem to de-wet the surface of the p-GaN and form a network of thin contacts. These narrow features may not be continuous and may have a higher resistance than the thicker, more uniform contact. This effect coupled with low lateral conduction in the p-GaN leads to the non-uniformity that is seen in the EL. The thicker contacts more uniformly distribute the current through the LED, increasing the active area of the device. This effect is very pronounced in the electrical characteristic as seen in figure 57.

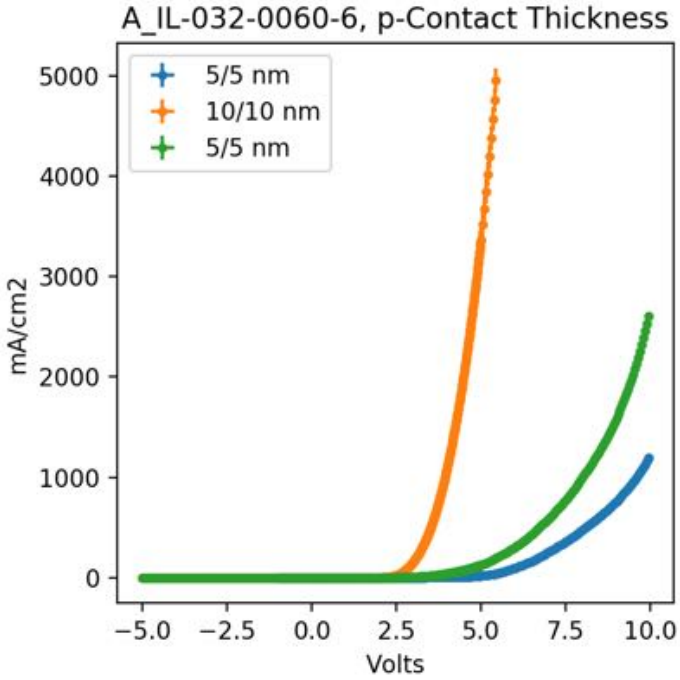

Figure 57: Effect of the contact thickness on the IV characteristics

While the contact thickness clearly has an effect on the electrical performance of the LEDs and solar cells what is necessary for the highest performance is to understand their effect on the optical performance as well. For very thin p-contacts the devices will be limited electrically, but this effect will be negligible after a certain thickness of contact and the contacts being semi-transparent when they are thin

become opaque when they are thick. This will limit the performance of the devices optically. A full study is underway to determine the optimal contact thickness for LEDs and solar cells. The next step will be to investigate other materials, like transparent contacts made of ZnO, ITO, or Ni/ITO.

3.5 Passivation and Passivation Etching

The termination of the GaN crystal on the surface and especially on the edges of the etched mesa produce surface states capable of conducting current[156]. In LEDs and solar cells this results in a leakage current between the anode and cathode that will tend to reduce the shunt resistance and effect the efficiency of the LED and V_{oc} of the solar cell. A dielectric like Al_2O_3 or SiO_2 is often used to passivate the surface and minimize this leakage current. We are studying the effect of both of these materials on the shunt resistance of the LEDs and solar cells, but as yet this study is incomplete. We have in preparation for this study investigated the deposition and etching of SiO_2.

For this study SiO_2 was deposited first by PECVD on Si wafers to determine the etch rate. We achieved a uniformity within the wafer of between 1.1 and 1.2% and a wafer to wafer uniformity of 0.3%. The samples were then etched in 49% HF for various times and the new thickness by ellipsometry. The uncertainty in the thickness measurement is calculated directly from the uncertainty in the current and previous thickness measurements and the uncertainty in the etch time is assumed to be half of a second and will increase with each subsequent etching. The etch rate determined by this experiment was about 6 nm/s as shown in figure 58.

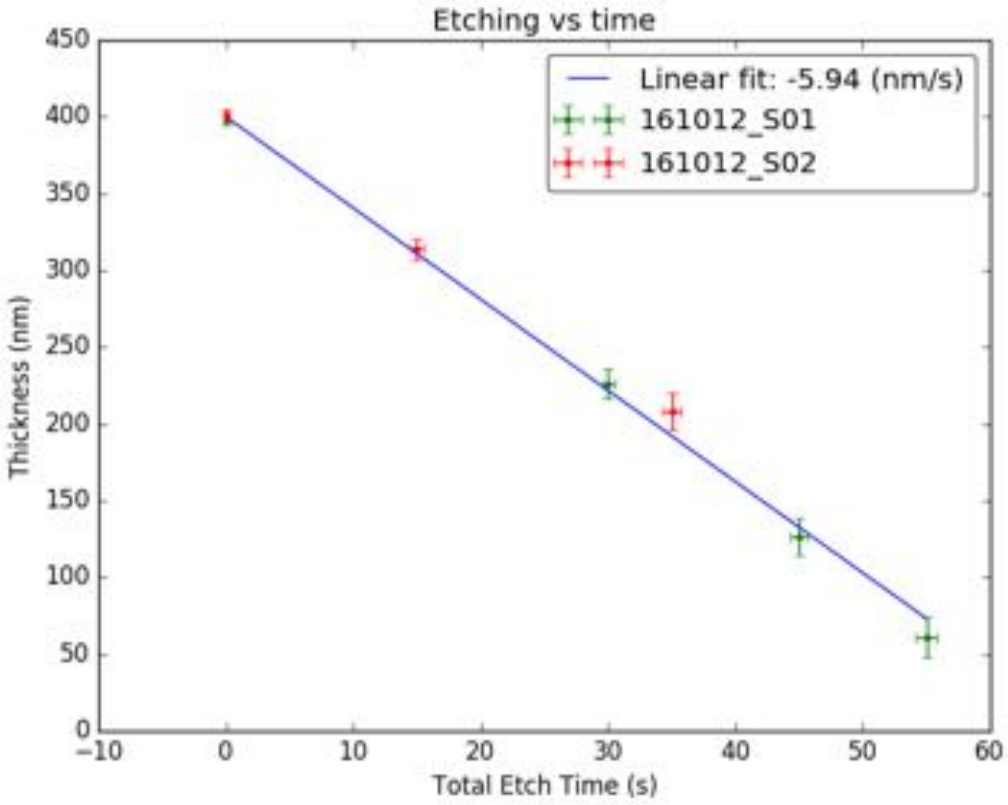

Figure 58: Change in SiO_2 thickness with wet etching

Next we attempted to determine effect on SiO_2 passivation on the InGaN LED samples. However the effect was difficult to determine as the experiment was performed before the p-contact and p-bus bar optimizations were complete. Nonetheless we can show that there is not a detrimental effect to the LEDs in figure 59.

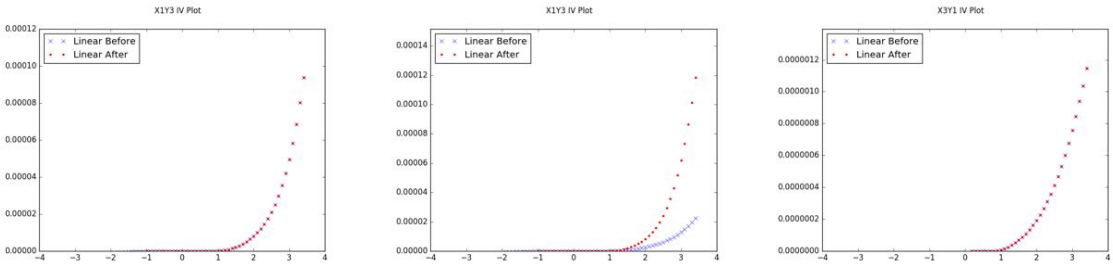

Figure 59: Effect of SiO_2 passivation on the IV characteristic of LEDs with non-optimized p-contacts

3.6 Conclusions and Next Steps

We have deconstructed each step of the process in making InGaN based LEDs and solar cells. We have achieved very uniform and repeatable results for nitride etching. We have also studied the effect of v-pits on InGaN based solar cells and demonstrated that we can fill the v-pits using a cured HSQ resin. We still have to show the v-pit passivation will enhance the V_{oc} of solar cells with low-temperature p-GaN. On the n-contacts we concluded that a Ti/Al/Ni/Au structure was both more stable and resulted in a better morphology after annealing both a two-step Ti/Al n-contact with a Ni/Al/Ni/Au bus bar and a one-step contact of Ti/Al/Ni/Al/Ni/Au contact. We have also made significant progress in optimizing Ni/Au contacting to p-GaN, however this remains a challenge.

We see a decrease in the specific contact resistance of Ni/Au p-contacts with the annealing temperature until about 625° C. There is no clear trend from the studies of HCl cleaning and small variations in Ni:Au ratio. For now we can repeatably achieve ohmic p-type contacts with a moderate specific contact resistance of 2–4$\times 10^{-2}$ Ω cm^2. It is not clear how to proceed to achieve p-contacts with a lower specific contact resistance. The literature suggests a few mechanisms that appear to be correlated with ohmic contact formation on p-GaN but the strength and even validity of each of these mechanisms is still under debate. Assuming that Ni/Au contacts annealed in oxygen have a layer of NiO on the surface there may be some resistance added to the structure that is measured as specific contact resistance but in reality is based on the material. Furthermore the thin quality of the contacts may make the simplification that the contact resistance is greater than the material resistance of the metal contacts false. Therefore simply increasing the amount of Au will improve the measured specific contact resistance. This is because the surface and amount of Ni remain constant while the overall thickness of the contact increases. This increase of thickness will lower the resistance of the metal in itself and the amount of NiO on the surface will

decrease also as more Ni will remain in the solid solution instead of out-diffuse at the surface in contact with oxide (assuming the process is diffusion limited). Also there are mixed results as to the effect of HCl cleaning of the sample. Perhaps a different solution (HF, aqua regia (HNO_3:HCl 1:3), boiling KOH are all mentioned in the literature) will have better results.

Optimizing p-contact thickness is critical for device performance. Thicker p-contacts result in better current spreading, but at a potential loss of optical transparency. The performance vs Ni/Au p-contact thickness of the LEDs and solar cells should be studied as well as the transparency vs thickness using FTIR. These results should be compared against results obtained using a transparent contact like ITO.

We have taken the first steps towards optimizing the mesa passivation required to achieve a high shunt resistance. We have shown that the deposition and etching of SiO_2 is very uniform but have yet to perform an in-depth study on the effect of different dielectric deposition recipes and materials on the shunt resistance. Finally, a study of antireflective coatings should be done to decrease the loss due to optical reflections. These may be deposited in addition to or in parallel with the passivation materials.

In conclusion we have taken the first steps towards a fully optimized process for of high-efficiency LEDs and solar cells. This has resulted in encouraging results for both large (1 cm^2) and small size solar cells and LEDs. Furthermore, we have laid out a clear experimental pathway to move forward and increase the performance of these devices.

CHAPTER IV

RESULTS

4.1 LED Results

InGaN based LEDs are a mature and commercial technology. Therefore can use commercially available data and LEDs to benchmark our growth and fabrication technology. We have characterized our LEDs using a variety of techniques and they show significant improvement after processing optimization as shown in the previous chapter. The structure of the LEDs we have studied is shown in figure 60

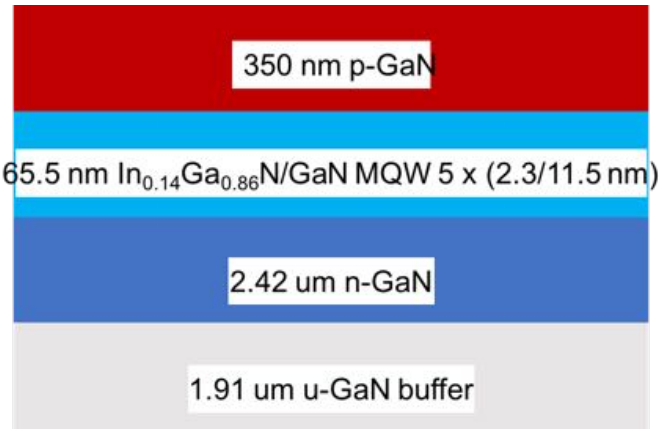

Figure 60: Structure of the MQW LEDs

4.1.1 Growth Results

We can characterize the InGaN MQW thicknesses, composition and quality using x-ray diffraction and reciprocal space mapping on the as-grown samples as shown in figure 61.

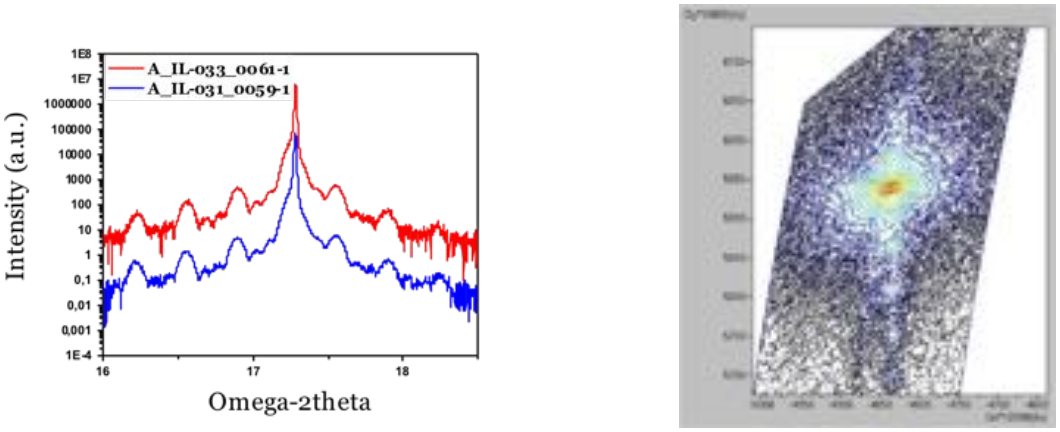

(a) $\omega - 2\theta$ XRD scan of two samples

(b) Reciprocal Space Map

Figure 61: XRD data for 5 periods of $In_{0.14}Ga_{0.86}N$/GaN MQWs on GaN

XRD data give us information about the crystal lattice. For a single, homogeneous crystal the quality can be deduced by the width of the peak of the XRD curve. Layer thickness can be determined by the Pendellösung interference fringes. We are chiefly concerned with the composition, layer thickness, and strain of InGaN epilayers grown on GaN. The composition and strain cannot be determined independently using a single scan as both of these physical properties effect the lattice parameters of the crystal. Therefore both symmetric and asymmetric scans are performed and custom modeling software is used to determine both the composition and strain of the InGaN epilayers[2]. These data indicate that we have achieved the LED structure shown in figure 60.

Furthermore we can characterize the uniformity of the InGaN MQWs across the wafer using photoluminescence. To do so we optically excite the crystal using a UV layers. The sample will then electrons in the sample will recombine resulting in a photoluminescence spectrum that we can measure. A photoluminescence spectrum is shown in figure 62 (a) and a map of the peak wavelength is shown if figure 62 (b).

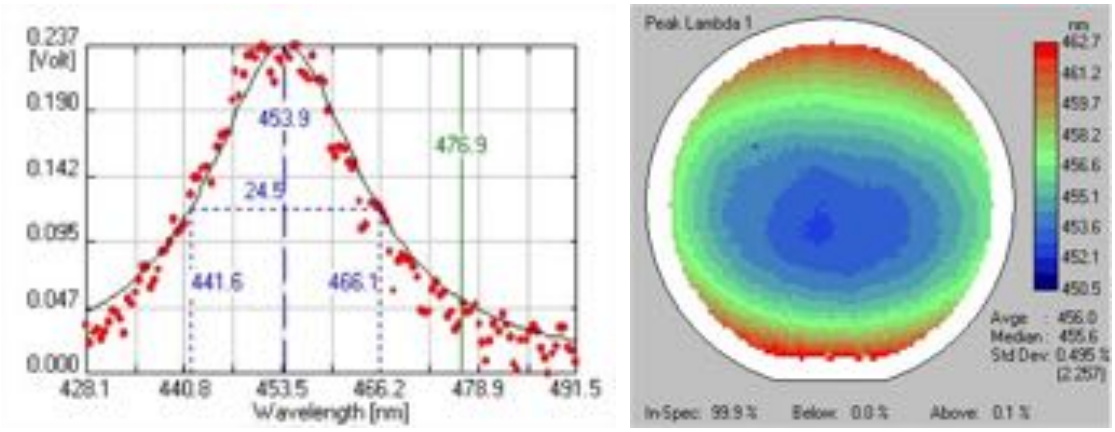

(a) Photoluminescence Spectrum (b) Photoluminescence Mapping

Figure 62: Photoluminescence data for a 5 periods of $In_{0.14}Ga_{0.86}N$/GaN MQWs sample on GaN

These data indicate a peak wavelength of 456 nm with a 0.5% standard deviation across the wafer.

4.1.2 Electrical Characterization

III-Nitride PIN diodes do not fit the traditional ideal diode equation well, instead the presence of schottky barriers at the contacts and the high levels of intrinsic defects result in a complex relationship between the current and the voltage[18, 19]. This relationship can be modeled by breaking the IV curve into 4 zones as shown in figure 63.

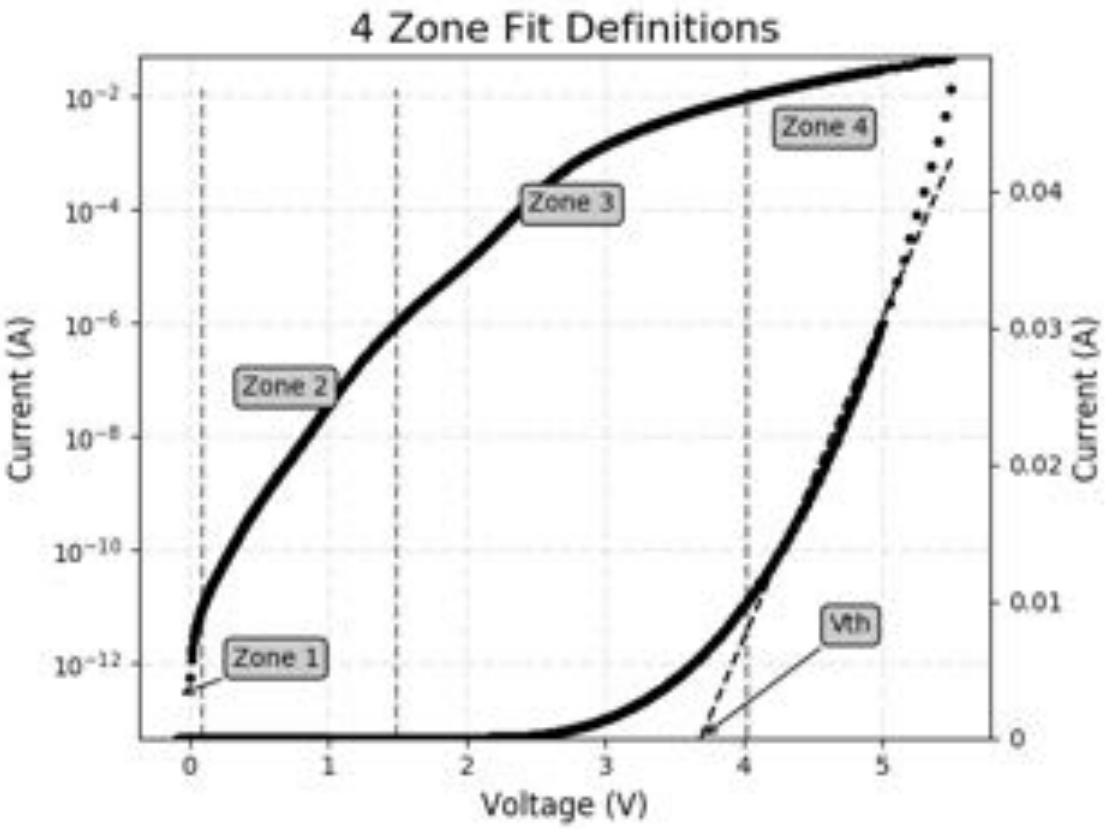

Figure 63: 4 zone model for LED characteristics[18, 19]

These zones are defined by the dominant current that flows through the diode, but the definition of the zones varies from publication to publication as shown in table 12. Furthermore the structure of the LEDs made will impact the zone definitions. Those analyzed by Balliot and Chambion, for example, both included an AlGaN electron blocking layer between the InGaN MQWs and the p-GaN[18, 19]. Therefore, it is generally best to define the zones for analysis based on the IV curve of the LED structure in question.

4.1.2.1 Electronic Model of InGaN Based LEDs

Zone I: Leakage Current

Zone I is characterized by current leakage through defects in the material and across conductive surface states like on the border of the mesa. Zone I can be modeled

Table 12: Definition of zones for 4–Zone IV curve analysis

Zone Number	Dominant Current	Zone Definitions (A)	
		Balliot[18]	Chambion[19]
I	Leakage Current	0–10^{-11}	0–10^{-10}
II	Field Emission + PN Junction	10^{-11}–10^{-6}	10^{-10}–10^{-5}
III	Thermionic/Thermionic Field Emission + PN Junction	10^{-6}–10^{-2}	10^{-5}– 0.1
IV	Series Resistance	$> 10^{-2}$	> 0.1

simply by Ohm's eqaution:

$$J_I = V/R_{sh} \tag{49}$$

Where I is the current in mA, V is the voltage in mV and R_{sh} is the shunt resistance in Ωs. Typical values of R_{sh} range from $10^{10} - 10^{12}$ Ωs

Zone II: Field Emission

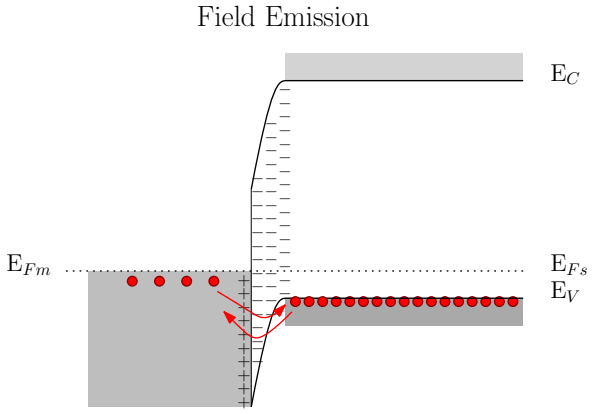

Figure 64: Field Emission through a Schottky Barrier

Current begins to flow through the diode in Zone II. At this voltage there is a potential that current will tunnel through the schottky barrier as seen in figure 64. The current flowing through this section can be described by the equation:

$$J_{II} = A^* T^2 \left(\frac{E_\infty^2}{kT}\right) \frac{\Phi_B - V_d}{\Phi_B} \exp\left(\frac{-2\left(q\Phi_B\right)^{3/2}}{3E_\infty\sqrt{q\Phi_B - qV_d}}\right) \tag{50}$$

Where A^* is the Richardson constant, and E_∞ is a characteristic energy given by:

$$E_\infty = \frac{q\hbar}{2}\sqrt{\frac{N_A}{\epsilon_{SC} m_h^*}} \tag{51}$$

Where N_A is the concentration of acceptors, m_h^* is the hole effective mass, and ϵ_{SC} is the dielectric constant of the semiconductor. Finally the height of the schottky barrier, Φ_B can be described by the equation:

$$q\Phi_B = q\chi_{SC} + E_{g_{SC}} - \Phi_M \tag{52}$$

Finally equation (50) can be simplified, as was done by Morkoç[157]:

$$J_{II} = J_{II_0}\left(\exp\frac{q(V_d - J_{II}R_s)}{\eta_1 kT} - 1\right) \tag{53}$$

Where η_1 is an ideality factor given by:

$$\eta_1 = \frac{E_\infty}{kT}\coth\frac{E_\infty}{kT} \tag{54}$$

Typical values of η_1 and J_{II_0} are between 6–11 and $10^{-11} - 10^{-8}$ respectively.

Zone III: Thermionic and Thermionic Field Emission

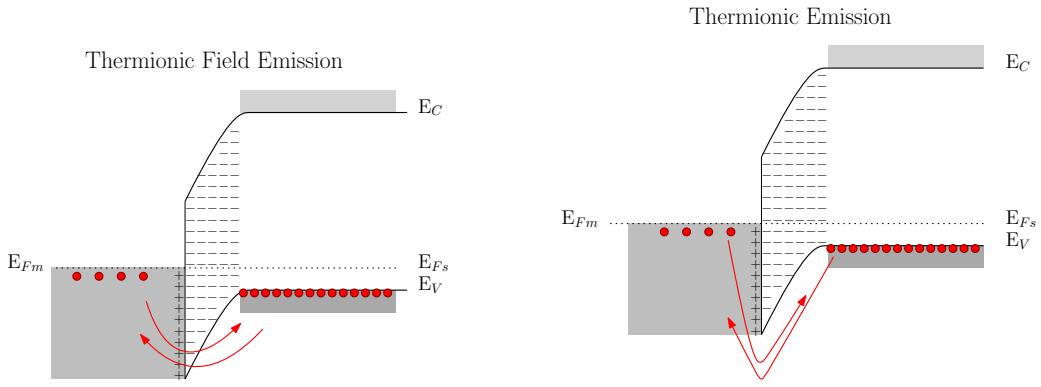

(a) Thermionic Field Emission (b) Thermionic Emission

Figure 65: Thermionic and Thermionic Field Emission

Thermionic and thermionic assisted field emission are shown schematically in figure 65. Similar to field emission we can model the current flow by:

$$J_{III} = \frac{A^* T^2}{2\pi kT} \left(\frac{\pi}{f_{TFE}} \right)^{1/2} \exp\left(\frac{qV}{kT} - b_{TFE} - c_{TFE} E_{TFE} \right) \left(1 + \operatorname{erf}\left(E_{TFE} f_{TFE}^{1/2} \right) \right) \tag{55}$$

Where b_{TFE}, c_{TFE}, and f_{TFE} are the coefficients of the Taylor expansion of the transparency of the barrier around E_{TFE}. Again a simplified version of the equation is used to fit the function given by[157]:

$$J_{III} = J_{III_0} \left(\exp \frac{q(V_d - J_{III} R_s)}{\eta_2 kT} - 1 \right) \tag{56}$$

Typical values of η_2 and J_{III_0} are between 1–1.8 and $\approx 10^{-27}$ respectively.

Zone IV: Series Resistance

Lastly Zone IV is characterized by the diode being in the "on" state with the current being limited by the series resistance of the contacts and the semiconductor. Zone IV can be modeled simply by Ohm's eqaution:

$$J_{IV} = V/R_s \tag{57}$$

Where I is the current in mA, V is the voltage in mV and R_s is the series resistance in Ωs. The threshold voltage can be estimated by extrapolating to where the linear resistance crosses the x-axis. Typical values of R_s and V_{th} range from 0.1 – 8 Ωs and 1.8–3 V respectively.

4.1.2.2 Modeling and Results

Zones I and IV are fitted first to find the series resistance, shunt resistance, and threshold voltage using orthogonal distance regression with linear model. η_1, J_{II_0}, η_2 and J_{III_0}, can then be fit by rewriting equations (53) and (56) in root form and using the series resistance found from zone IV. Newton's method can then be writing the Jacobian with respect to η_1, J_{II_0}, η_2 and J_{III_0} and using a least squares fit. The results vary depending on the thresholds used to determine the zones and so we applied three different thresholds for comparison. The fits on an LED are shown in figure 66.

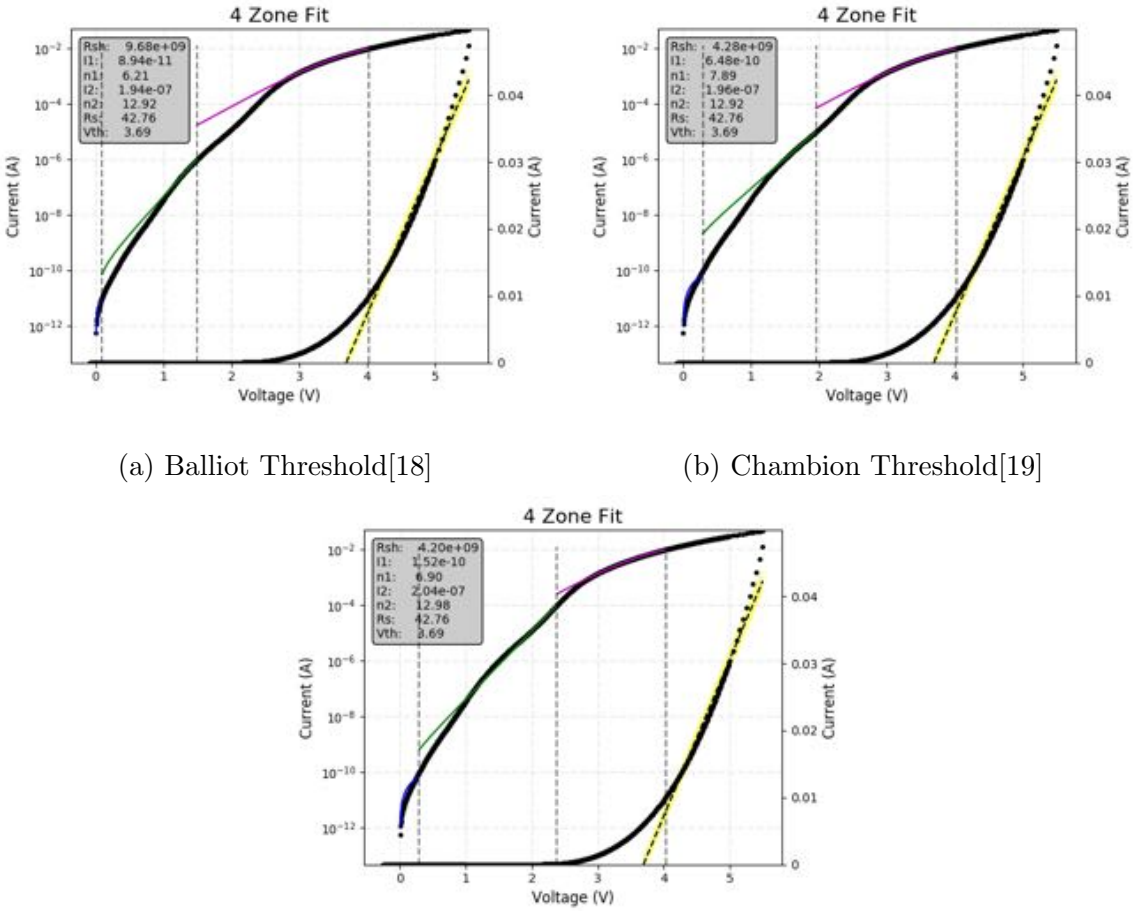

(a) Balliot Threshold[18]

(b) Chambion Threshold[19]

(c) Deterministic Threshold

Figure 66: Four Zone fits to an LED

As can be seen from figure 66, the fits are pretty good which is surprising given that our LEDs are lacking an electron blocking layer. Furthermore it is evident that the fits to zones 1, 2, and 4 are quite close to typical values found in commercial LEDs. The shunt resistance is lower than desired, but this is likely due to the lack of optimized passivation on this sample. In addition the series resistance remains an order of magnitude too large, but this can be lowered by further optimizing the contacts. Zone III is not fit well and also the fitted values are far from the ideal suggesting that further work is necessary optimizing the contacts and the material structure.

Table 13: Comparison of IV curve figures of merit using different zone thresholds

	Thresholds			
Figure of Merit	Balliot[18]	Chambion[19]	Deterministic	Typical Value
R_{sh}	9×10^9	4×10^9	4×10^9	$10^{10} - 10^{12}$
J_{II_0}	9×10^{-11}	6×10^{-10}	1.5×10^{-10}	$10^{-11} - 10^{-8}$
η_1	6	8	7	$6 - 11$
J_{III_0}	2×10^{-7}	2×10^{-7}	2×10^{-7}	$\approx 10^{-27}$
η_2	13	13	13	$1 - 1.8$
R_s	43	43	42	$0.1 - 8$
V_{th}	3.69	3.69	3.69	$1.8 - 3$

4.1.3 Optical Results

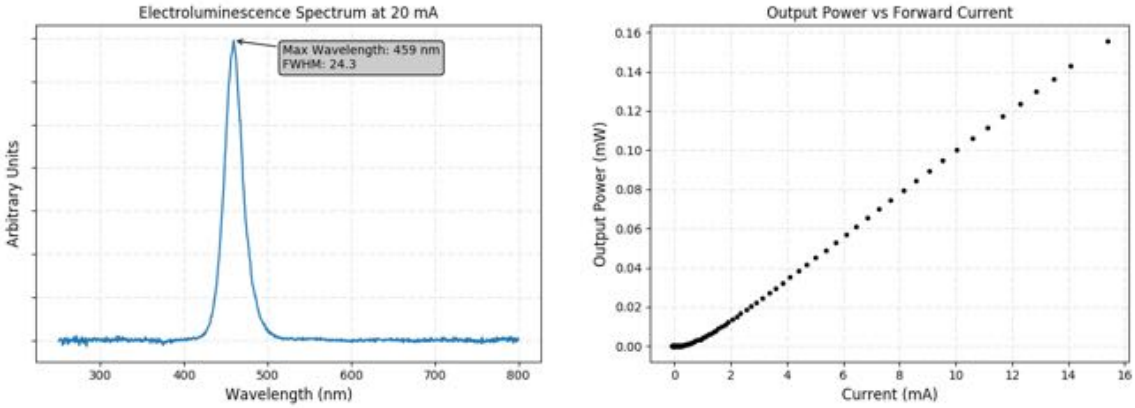

Figure 67: Electroluminescence Measurements

The LEDs Illuminate well with a peak at 459 nm and a FWHM of 24 nm. This is as expected from the PL measurement. Furthermore the optical power vs the current remains linear up above 70 mA.

4.1.4 Solar Cell Results

In order to test the potential of InGaN based solar cells we measured the EQE and solar cell performance of the LEDs. The performance will be limited by the thin absorber layer as well as the thick p-GaN layer.

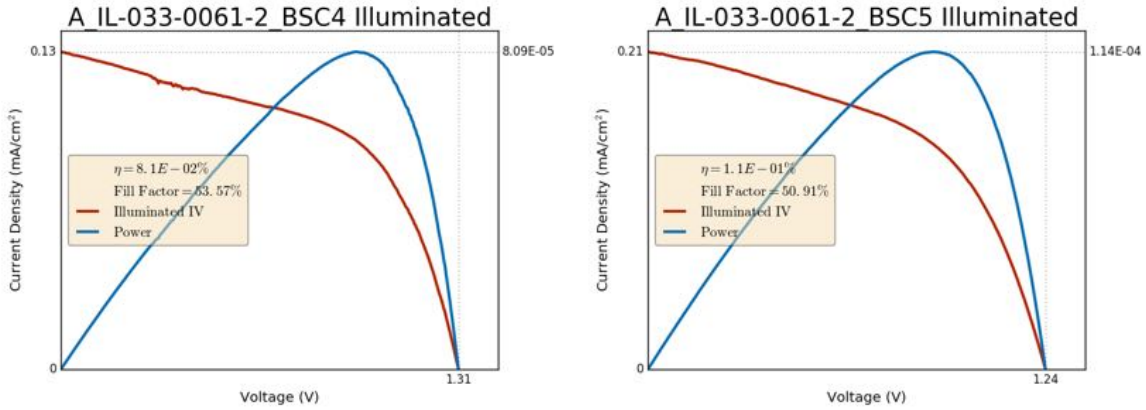

(a) One sun illuminated performance (b) One sun illuminated performance

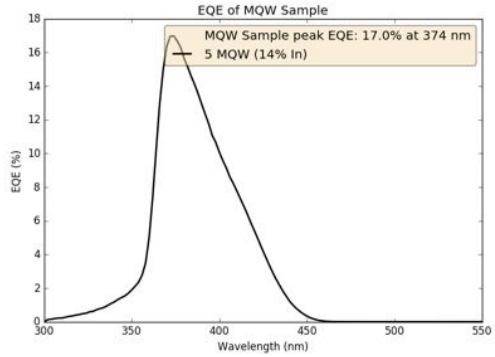

(c) LED EQE

Figure 68: Solar performance of LED Sample

While the efficiency is low, we can see that this is due to a low short circuit current, which is to be expected with only 11 nm of InGaN with 14% In. Also the fill factor could be better as a result of the lack of optimized passivation. A thicker absorber layer will improve the solar cell performance.

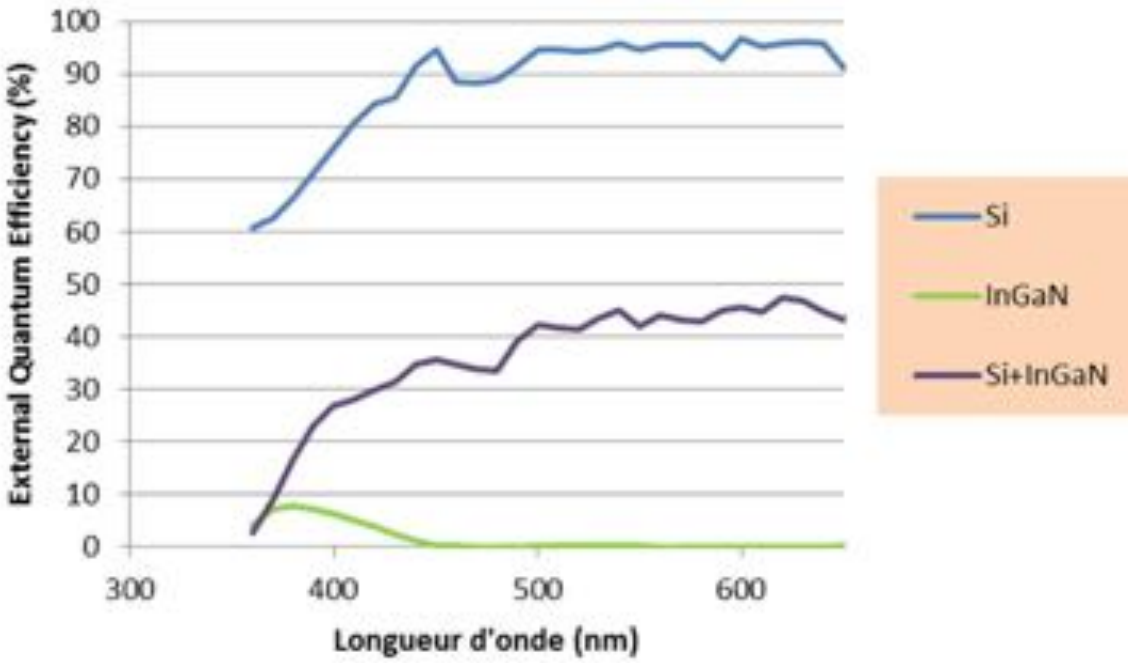

Figure 69: EQE of MQW-InGaN/Si four terminal, tandem solar cell

Furthermore we have measured the EQE of a MQW-InGaN/Si four terminal solar cell tandem device, figure 69, and find that for the stacked geometry there is a large decrease in the performance of the Si solar cell. This is due primarily to reflections from the surface of the nitride cell. We also have a rough measurement of the reflection and the LED reflects approximately 15% of light. Combined with absorption in the p-contacts and reflection and scattering from the sapphire substrate we can account for this loss. We can therefore conclude that for a successful tandem device broad-spectrum transmission must be optimized including the use of an anti-reflective coating.

4.2 Boron Nitride Solar Cell Liftoff

Another avenue for advancement is to grow the solar cell on top of hexagonal born nitride (BN). Hexagonal BN has a Van der Waals structure similar to graphite or graphene and is thus easily mechanically exfoliated. This allows for devices realized

on top of BN to be easily separated from the substrate on which they were grown[158]. This has application for solar cells because the devices could be removed from the sapphire substrate and placed either on a smaller band gap solar cell like Si to form a tandem, or on a heat sink increasing the efficiency of concentrated photovoltaics. Furthermore for solar cells it allows for backside processing of n-contacts that can also serve as rear reflectors. The same qualities that allow for easy lift off also make device fabrication a challenge. Extra care must be taken when processing the materials in solution and performing standard fabrication techniques like metal lift off to not also remove the active film. We have some expertise in this area and have realized UV photodetectors using a thin hexagonal BN film. The BN photodetectors are shown in figure 70.

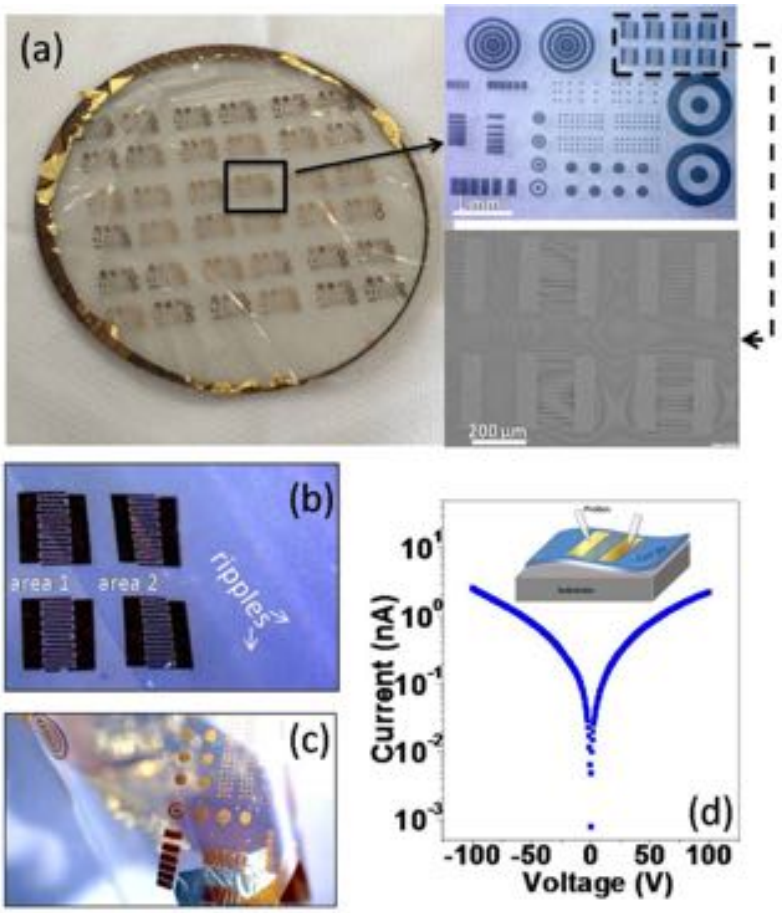

Figure 70: BN photodetector Devices. (a) The wafer showing film plasticity and detail of interdigited schottky diode devices, (b) ripples with a device on the film ripple, (c) freestanding lifted off device, and (d) current voltage characteristic

Using the experience gained with the BN photodiodes to make a first attempt and growing and measuring a solar cell on BN. The structure used was to grow n-GaN/10×(Semibulk $In_{.15}Ga_{.85}N$/GaN (8 nm/1 nm))/GaN/p-GaN/p+GaN on Al-GaN/BN. Then the cell was etched, followed by n and p contact formation and p-pad deposition respectively. This resulted in reasonable dark IV characteristics, but poor solar cell efficiency as shown in figure 71.

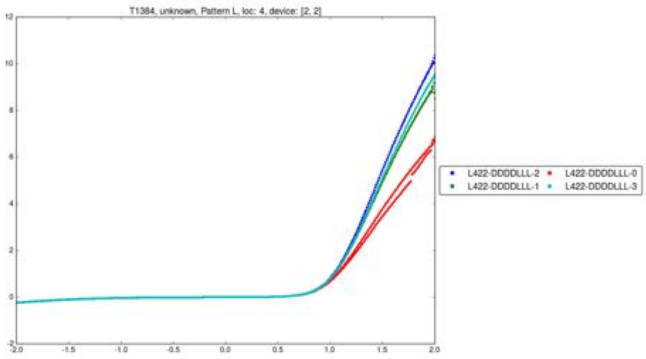

(a) Current (mA) *vs* Voltage for several devices

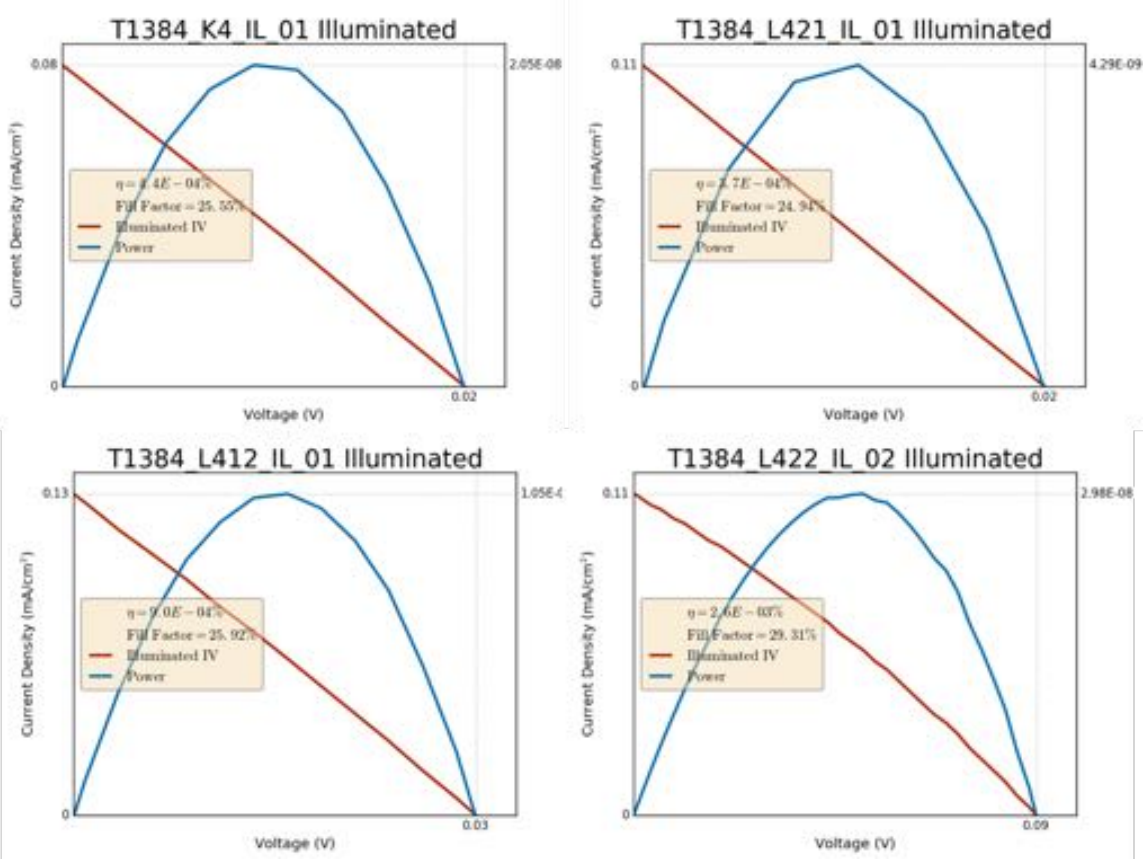

(b) AM1.5G Solar Cell Performance of 4 devices

Figure 71: Diode and Solar Cell Performance of Semibulk InGaN on BN device

The highest AM1.5G solar cell efficiency was 0.0000003%, which is far from the state of the art. The cause of this low efficiency is evident from figure 71 (b). The

solar cell has an extremely poor fill factor as well as a low short circuit current density (0.13 mA/cm^2). Further investigations into the cause of the poor performance led to the hypothesis that the extremely low fill factor was the caused by unpassivated v-pits and the lack of mesa passivation. SEM analysis of the sample in figure 72 seem to support that these processing steps were skipped.

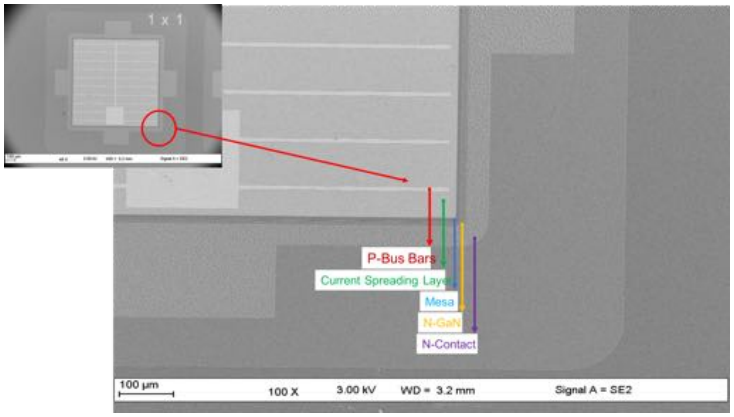

(a) Device Design of Solar Cell on BN

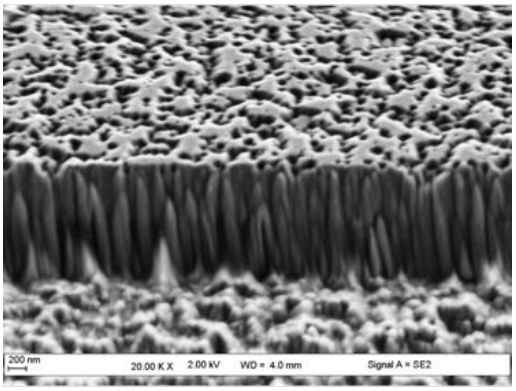

(b) Detail of mesa edge

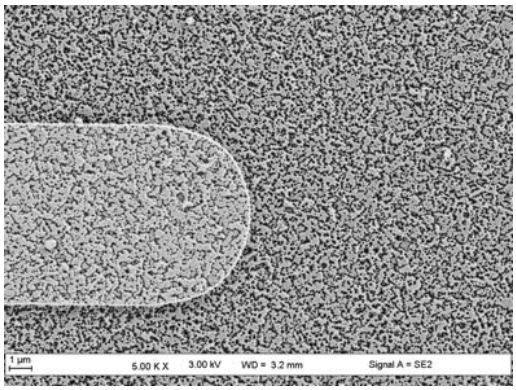

(c) Detail of p-bus bar and current spreading layer

Figure 72: SEM of Semibulk InGaN on BN device

Figure 72 shows no evidence of passivation. Furthermore it can been seen that the p-GaN surface is, as expected, rough and there is evidence of a columnar microstructure from the edge of the mesa. The detail of the top contact (figure 72 (b)) shows that the rough structure of the GaN is transferred to the contacts, and furthermore

shows no evidence of v-pit filling. Further investigations are underway using EBIC to confirm that the unpassivated v-pits are to blame for the poor solar cell performance.

4.3 Nano-selective Area Growth Progress and Solar Cell performance

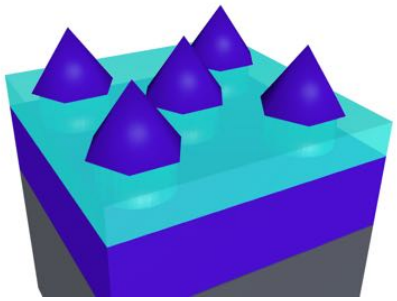

(a) Schematic of NSAG pyramids grown through HSQ mask

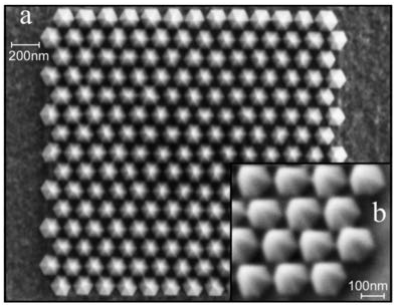

(b) InGaN monocrystal NSAG pyramids and detail of at a 37° tilt

Figure 73: NSAG Growth Method

We have pioneered nano-selective area growth (NSAG) of GaN and InGaN on several substrates ranging from traditional sapphire to wide band gap SiC, inexpensive Si (111), and ZnO [159]. This growth method involves first patterning the template layer using a nanolithography process. We have had success using hydrogen silsesquioxane (HSQ) and electron beam lithography to form a glass-like compound that serves as a mask for the growth process[159]. The GaN and InGaN crystals tend not to nucleate on the mask and instead prefer the template layers. Using of the size of the openings in the mask and the mask aspect ratio we can prefer single crsytalline growth out of the mask. Furthermore the preferential growth direction is along an unstrained facet at an angle to the plane of the substrate. This results in the hexagonal pyramids shown in figure 73 and allows for the crystal to impose it's own lattice and grow unstrained. In addition we have been able to achieve very high levels of In incorporation using NSAG[159]. As a growth process that results in low defect densities the NSAG process may offer a pathway to higher efficiency LEDs and solar cells. Because of the high level of In incorporation possible, we may be able to break the efficiency barriers

limiting InGaN solar cells (that are mostly limited because they are transparent to the majority of the solar spectrum) or potentially make green and white light LEDs.

4.3.1 NSAG Process Development with the CEA

We briefly collaborated with the commissariat à l'énergie atomique or CEA on a process involving NSAG for LEDs. The idea was to show that NSAG could be used to make LEDs and simplify the fabrication process by eliminating GaN ICP etching. The project called for large area nanolithography which is a challenge because of the time required to write large patterns using electron beam lithography. Furthermore the sensitivity of HSQ electron beam resist can vary with time before exposure, and so careful optimization of the first step was required. The proposed process is shown in figure 74. As can be seen it is a simple process that requires only wet etching and contact formation. The primary challenges are the formation of the SiO_2 during nanolithography and achieving epitaxial lateral over growth (ELOG) of the p-GaN.

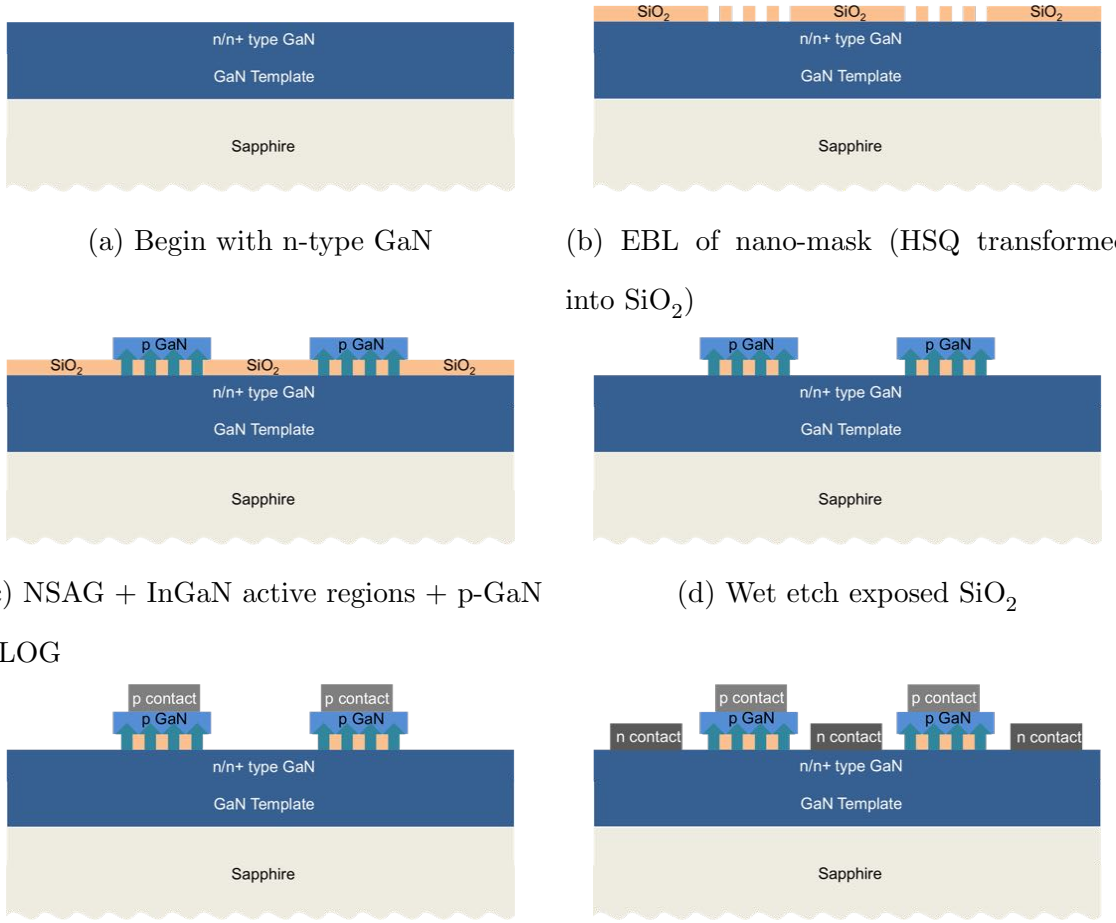

(a) Begin with n-type GaN

(b) EBL of nano-mask (HSQ transformed into SiO_2)

(c) NSAG + InGaN active regions + p-GaN ELOG

(d) Wet etch exposed SiO_2

(e) p-contact formation

(f) n-contact formation

Figure 74: CEA Process

Standard ELOG conditions do not result in overgrowth on NSAG pyramids as shown in figure 75 (a) and (b), but by adding Cp_2Mg in the growth it has been achieved on both small and large scale NSAG regions as is shown in figure 75 (c) and (d).

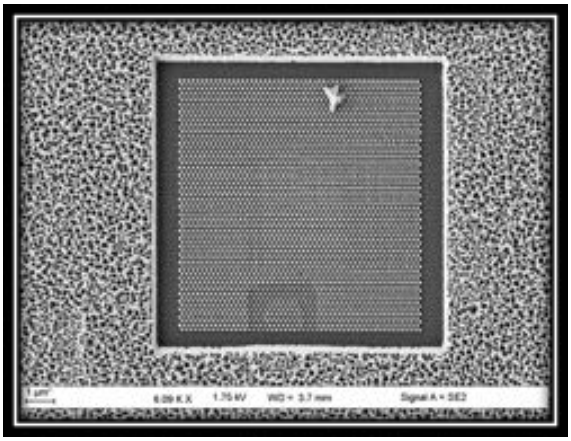

(a) A NSAG before ELOG

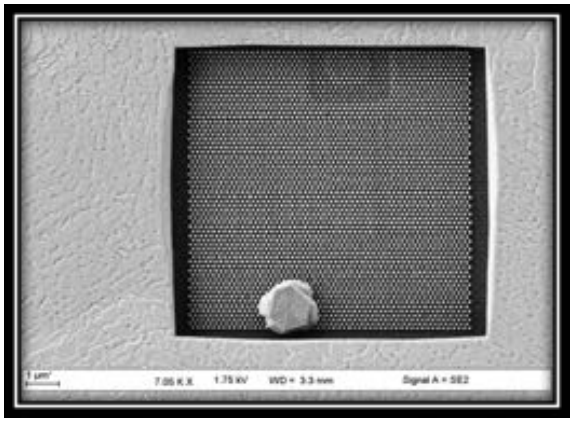

(b) The same NSAG region after ELOG conditions

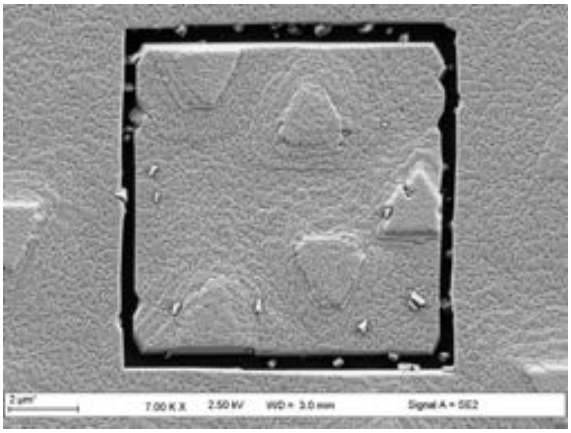

(c) A NSAG region with p-lateral overgrowth

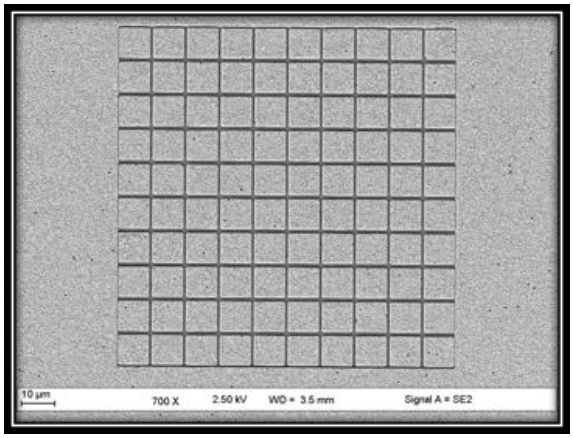

(d) CEA Pattern with p-lateral overgrowth

Figure 75: Epitaxial Lateral Over Growth on NSAG samples

The only other challenge was to achieve large area nanolithography. This was done by first performing monte-carlo simulations of electron scattering in multi-layered material using commercially available sceletron software. Using the simulated dose-radius curves were were able to determine appropriate dose modulations within the region exposed by EBL. This is done because despite the electron beam being quite focused (< 2 nm in diameter) the electrons can scatter off of atoms in the GaN and in the HSQ resist resulting in indirectly increasing the dose of the surrounding areas. Thus to have a uniform does across an area the dose applied to the center of a large

pattern should be less than the dose on the edges. The dose correction is pattern dependent, and we show the nanolithography pattern as well as the dose correction in figure 76.

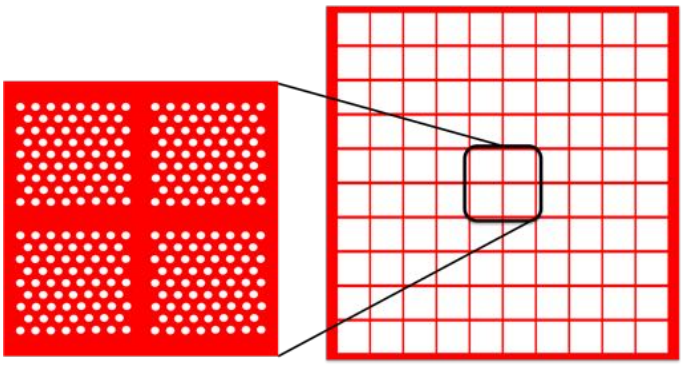

(a) Schematic of the design of the nanolithography mask and a detail of the pattern

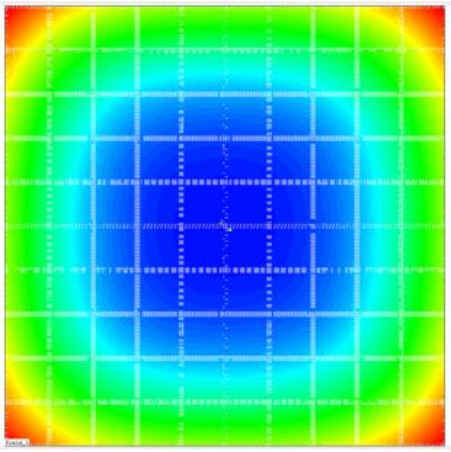

(b) Simulated dose modulations of the nanolithography mask

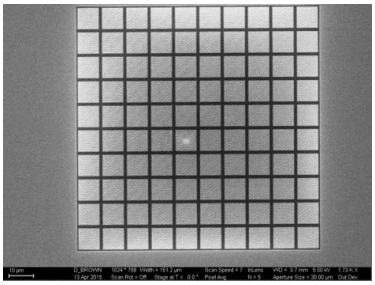

(c) SEM of the mask exposed with optimal dose

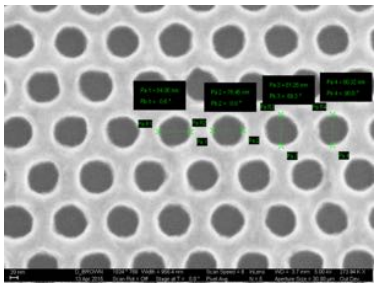

(d) Detail of the center of the nanolithography mask

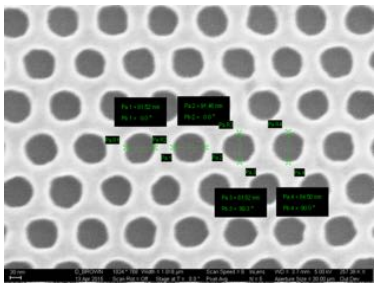

(e) Detail of the corner of the nanolithography mask

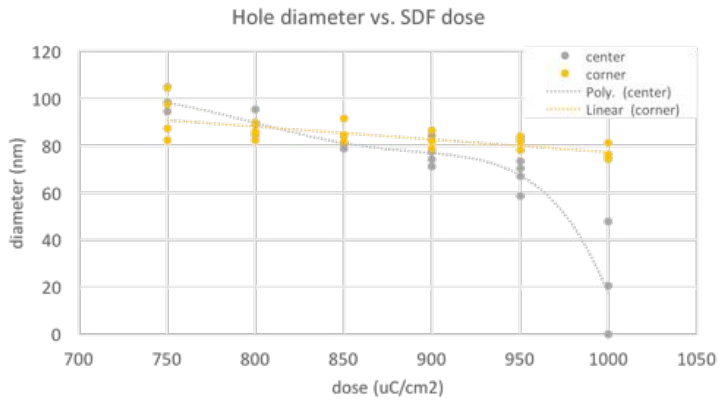

(f) Size of corner and central holes *vs* total dose indicating process window

Figure 76: Nanolithography mask optimization

As can be seen we achieved the large area photomask and by carefully calculating

the dose modulation and varying the dose we found an optimal process window for the nanolithography. Following nanolithography we attempted NSAG growth and encountered problems with the NSAG growth conditions. During growth we lost selectivity with the HSQ mask and small crystallites were found to form with increasing density away from the edges of the mask when previously we had good selectivity. This is shown in figure 77.

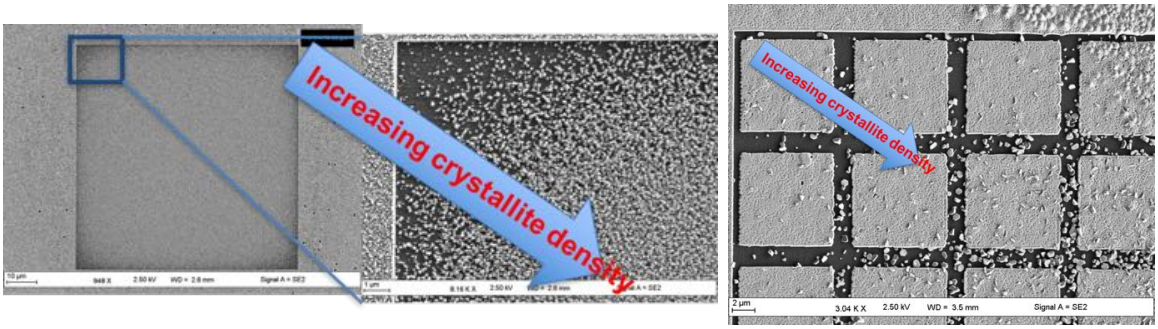

(a) Crystallites forming on an exposed HSQ square with no holes that is used for dose testing

(b) Crystallite formation on nanolithography mask

Figure 77: Issue with crystallite formation/loss of selectivity on HSQ mask

This process shows potential, but further work is necessary to realize the first devices using it.

4.3.2 First Full NSAG LED Process and Results

In fact in order to show the first devices using the NSAG process we prefer a more traditional process flow a mesa is formed by etching and the surface of the entire structure can be passivated using oxide. The first process was developed for 1 cm^2 devices and was carried out in Atlanta, GA. In this process, as is demonstrated in figure 78, HSQ is used to pattern a series of holes on the sample. These holes are typically between 70–100 nm in diameter and have a pitch double to their diameter, arranged in a hexagonal pattern.

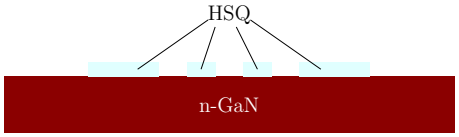

(a) HSQ Coating and EBL

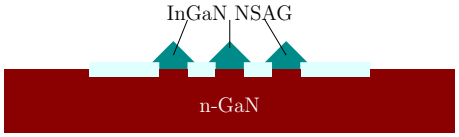

(b) Nano-Selectrive Area Growth

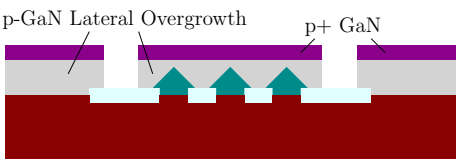

(c) p-Lateral and p+ GaN Growth

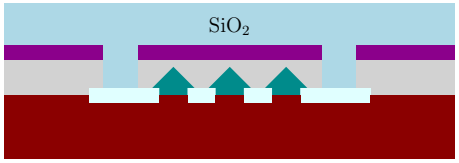

(d) SiO_2 Deposition

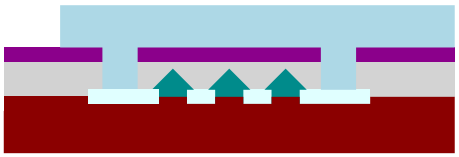

(e) SiO_2 Etching

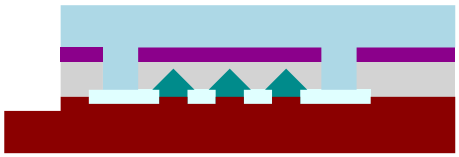

(f) GaN Etching

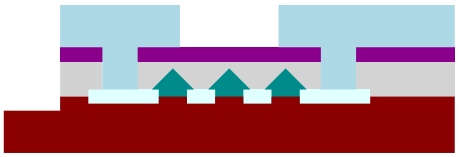

(g) SiO_2 Etching

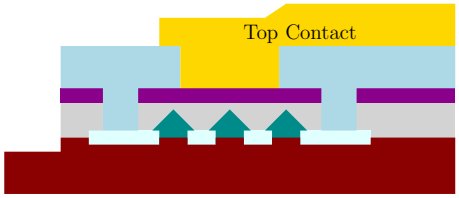

(h) Top Contact Formation

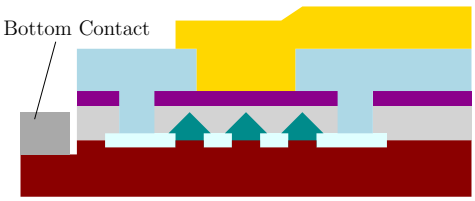

(i) Bottom Contact Formation

Figure 78: First NSAG Process

After nanolithography the samples are returned to the growth reactor where selective area growth is used to grow GaN out of the holes. In this process nanopyramids are formed above the holes. Then InGaN layers can be patterned on the relaxed facets of the pyramids followed by p-GaN growth and potentially epitaxial lateral overgrowth (ELOG). This process is illustrated in figure 79.

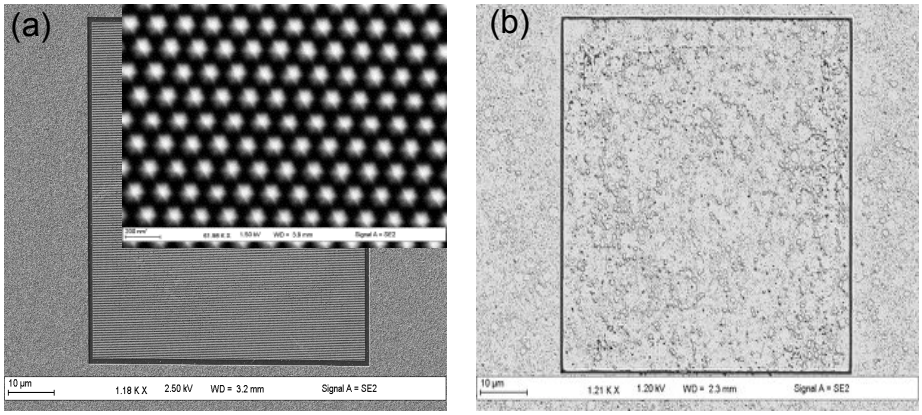

Figure 79: Nanopyramids growing out of the HSQ mask before (a) and after (b) p-GaN epitaxial overgrowth

After ELOG, SiO_2 is deposited to encapsulate the NSAG structures. The SiO_2 is etched to reveal the GaN field which in turn is also etched down to the n-type GaN. n-contacts can then be formed on the n-GaN surface. The SiO2 is then etched again to reveal the p-GaN surface and contact is then made to the p-GaN resulting in the structure you see in figure 80.

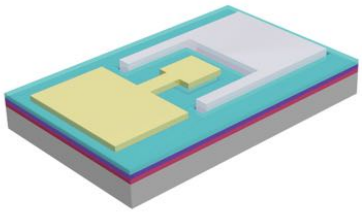

(a) Bird's Eye View of the a NSAG based device

(b) Cross-Section of a NSAG based device

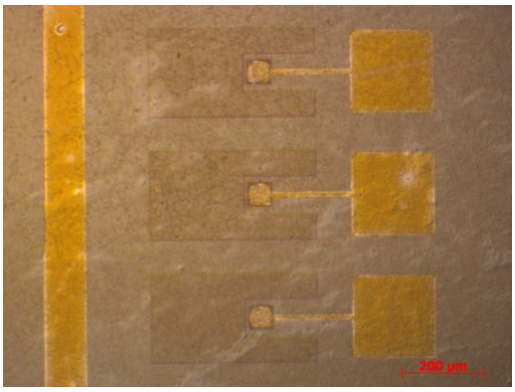

(c) Broad p-contact design before n-contact

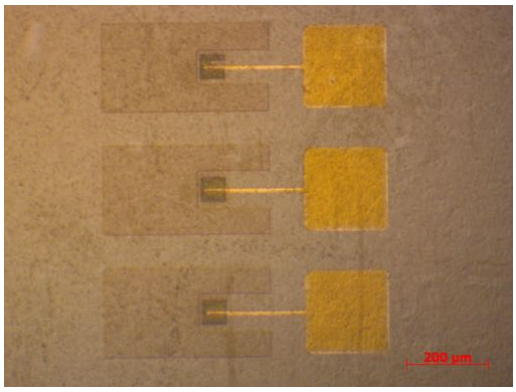

(d) P-contact finger design before n-contact

Figure 80: Realization of our first NSAG based devices

However in realizing the first devices several deficiencies in both the growth and the processing were uncovered. Firstly, the samples that were processed lacked full selective area growth, and so no nanopyramids were formed on the surface. Furthermore the p-GaN ELOG was ineffective, likely because of the lack of surface area by the defective NSAG growth. Then during the processing there were issues during selective GaN etching using the SiO_2 layer as as mask. The SiO_2 layer was thin (100 nm) and it seems that it was removed or at least degraded during the GaN ICP etching. Thus the device pictured in 81 has a short-circuit from the p-pad to the n-GaN. Furthermore the p-contact was annealed at high temperature twice, once for p-contact formation and a second time during the formation of the n-contact. These annealings coupled with the thinness of the contact and the surface topography of

the sample resulted in contact migration as well discontinuities.

Despite these shortcomings in the growth and the process the devices still display rectifying behavior and blue electroluminescent emission as shown in figure 81. This leads us to conclude that the NSAG diode process is a promising candidate for LEDs and solar cells in the near future.

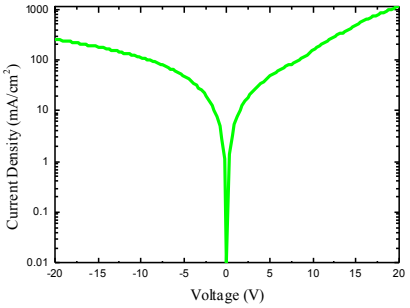

(a) Current Density *vs* Voltage

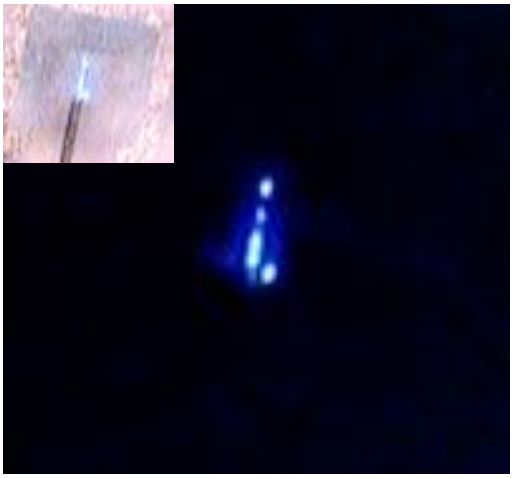

(b) Electroluminescence (background light on in detail)

Figure 81: Electrical and Electroluminescence of InGaN NSAG devices

4.3.3 Second NSAG Process Development and Photomask Design

Experience gained with the InGaN solar cells and LED processing as well as the results of the previous NSAG-LED devices were incorporated into a full 2-in mask. The proposed NSAG process is shown below in figure 82.

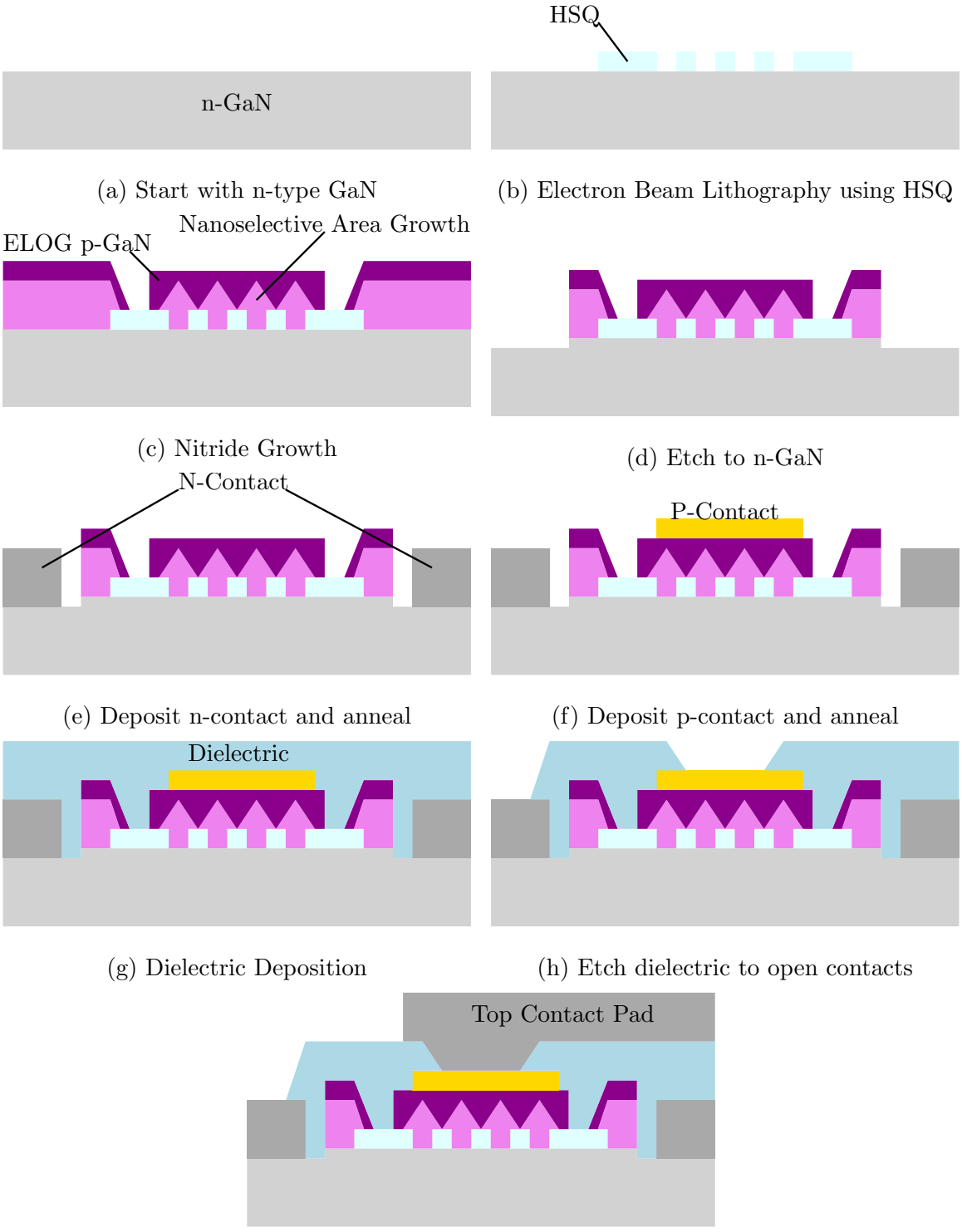

(a) Start with n-type GaN

(b) Electron Beam Lithography using HSQ

(c) Nitride Growth

(d) Etch to n-GaN

(e) Deposit n-contact and anneal

(f) Deposit p-contact and anneal

(g) Dielectric Deposition

(h) Etch dielectric to open contacts

(i) Deposit P-Pad

Figure 82: Revised NSAG process flow

In the revised process flow photoresist is used to mask the active area for etching

to avoid thinning or degradation of the oxide during this and subsequent steps. Furthermore to avoid issues with the top contact it is made in two steps. In this way one thickness and metallization/annealing scheme can be used to form the p-contact and another can be used as the contact pad. This allows for a thin, semitransparent contact to be used on the p-GaN and a thick contact that will have a low resistance and make an electrical connection over the topographical features (dielectric and nitride etching steps) to be used as the pad. To allow for maximum flexibility of devices and nanolithography masks a wide array of designs were made. These designs are illustrated in figure 83.

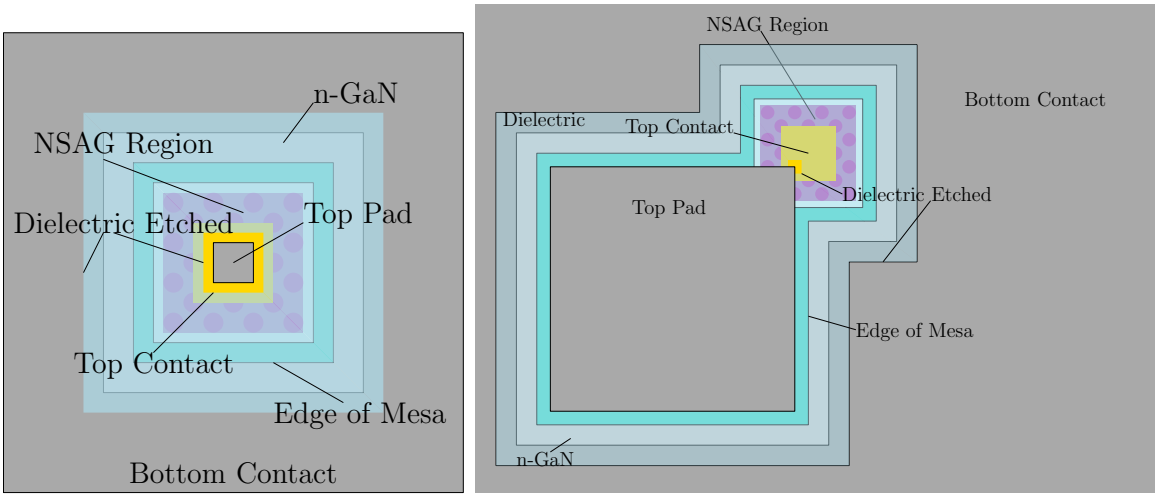

(a) Pad on top design

(b) Pad in corner design

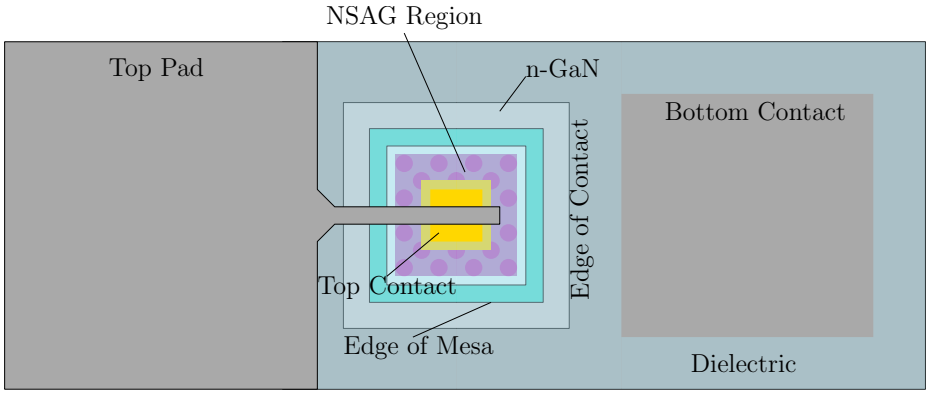

(c) Pad on oxide design

Figure 83: Revised NSAG device designs

The various designs alter both the size of the NSAG region as well as the placement and design of the top contact pad in order to allow the maximum freedom for nanolithography masks. To date these devices have not been realized, but progress is being made and the first results are expected in the next 4 to 6 months.

CHAPTER V

CONCLUSIONS AND FUTURE WORK

Solar cells will be one of many technologies used for producing electricity in the 21st century whether by large, utility-scale solar plants, small distributed power generation on residential and commercial buildings, or in outer space. We have described both the economic pressures driving innovation in solar cell research and advancements in materials and technology that are opening new avenues of research for high efficiency solar cells.

One such advancement was the revision of the band gap energy of InN down to 0.8 eV. Now InGaN appears to be a likely candidate for high performing solar cells, especially when combined in tandem with a lower cost solar cell material like Si. However, many challenges are blocking InGaN from reaching its theoretical maximum potential. Firstly the growth of reproducible, thick, high quality, high In content InGaN has yet to be achieved. Our laboratory has made significant strides in this regard by demonstrating both semibulk and nanoselective area growth approaches. Further difficulties with the number of material defects in InGaN materials caused in no small part by the lack of lattice matched substrates adversely effect the solar cell performance. Again nanoselective area growth combined with lateral epitaxy methods can reduce the effect of this issue. Lastly a double heterojunction (p-GaN/InGaN/n-GaN), approach has proved the most fruitful in the production of InGaN based solar cells. To implement this approach using MOVPE technology a compromise must be made between the InGaN absorber layer quality and the p-GaN morphology. We have shown that using low-temperature p-GaN it is possible to achieve a high quality InGaN absorber, but with v-pits in the p-GaN. These v-pits can enhance the short

circuit current of a solar cell, if included as grown into a final device the solar cell performance is reduced due to a high leakage current. We have shown a promising technology using HSQ resin to passivate the v-pits, thus maintaining both the absorber quality during p-GaN growth and the short circuit enhancement caused by the v-pits.

We have demonstrated the solar cell processing on LEDs and have optimized many of the processing steps. This work has greatly reduced the series resistance and repeatability of the LED devices. Further work needs to be done in studying the p-contacts, mesa passivation, and anti-reflection coatings, but the work has resulted in working InGaN/Si tandem solar cells.

REFERENCES

[1] A. Sreedhar, B. Sharma, and R. Purohit, "Efficiency calculations of heterojunction solar energy converters," *IEEE Transactions on Electron Devices*, vol. 16, no. 3, pp. 309–312, 1969.

[2] K. Pantzas, *Elaboration par MOVPE et caractérisation des matériaux (B)InGaN pour les cellules solaires de 3éme génération*. PhD thesis, Université de Lorraine, 2013.

[3] J. Piprek, *Semiconductor optoelectronic devices: introduction to physics and simulation*. Academic Press, 2013.

[4] A. Bhuiyan, K. Sugita, A. Hashimoto, and A. Yamamoto, "Ingan solar cells: present state of the art and important challenges," *Photovoltaics, IEEE Journal of*, vol. 2, no. 3, pp. 276–293, 2012.

[5] G. Greco, F. Iucolano, and F. Roccaforte, "Ohmic contacts to gallium nitride materials," *Applied Surface Science*, vol. 383, pp. 324–345, 2016.

[6] A. Standard, "G159, standard tables for references solar spectral irradiance at air mass 1.5: Direct normal and hemispherical for a 37 tilted surface," *Society for Testing Matls., West Conshocken, PA, USA*, 1998.

[7] M. Razeghi, *Fundamentals of solid state engineering*. Springer Science & Business Media, 2009.

[8] U. E. I. Administration, "Levelized cost and levelized avoided cost of new generation resources in the annual energy outlook 2016," 2015.

[9] Cadmium, "Pervoskite lattice," 2006. `https://commons.wikimedia.org/wiki/File:Perovskite.jpg,`, [Accessed 25-December-2016].

[10] B. M. Kayes, L. Zhang, R. Twist, I.-K. Ding, and G. S. Higashi, "Flexible thin-film tandem solar cells with $> 30\%$ efficiency," *IEEE Journal of Photovoltaics*, vol. 4, no. 2, pp. 729–733, 2014.

[11] S. Moon, K. Kim, Y. Kim, J. Heo, and J. Lee, "Highly efficient single-junction gaas thin-film solar cell on flexible substrate," *Scientific Reports*, vol. 6, 2016.

[12] A. Barnett, C. Honsberg, D. Kirkpatrick, S. Kurtz, D. Moore, D. Salzman, R. Schwartz, J. Gray, S. Bowden, K. Goossen, *et al.*, "50% efficient solar cell architectures and designs," in *2006 IEEE 4th World Conference on Photovoltaic Energy Conference*, vol. 2, pp. 2560–2564, IEEE, 2006.

[13] M. Arif, W. Elhuni, J. Streque, S. Sundaram, S. Belahsene, Y. El Gmili, M. Jordan, X. Li, G. Patriarche, A. Slaoui, *et al.*, "Improving ingan heterojunction solar cells efficiency using a semibulk absorber," *Solar Energy Materials and Solar Cells*, vol. 159, pp. 405–411, 2017.

[14] W. El-Huni, A. Migan, Z. Djebbour, J.-P. Salvestrini, and A. Ougazzaden, "High-efficiency indium gallium nitride/si tandem photovoltaic solar cells modeling using indium gallium nitride semibulk material: monolithic integration versus 4-terminal tandem cells," *Progress in Photovoltaics: Research and Applications*, vol. 24, no. 11, pp. 1436–1447, 2016. PIP-15-226.R2.

[15] M. Arif, J.-P. Salvestrini, J. Streque, M. B. Jordan, Y. El Gmili, S. Sundaram, X. Li, G. Patriarche, P. L. Voss, and A. Ougazzaden, "Role of v-pits in the performance improvement of ingan solar cells," *Applied Physics Letters*, 2016.

[16] C. Holzwarth, T. Barwicz, and H. I. Smith, "Optimization of hydrogen silsesquioxane for photonic applications," *Journal of Vacuum Science & Technology B*, vol. 25, no. 6, pp. 2658–2661, 2007.

[17] H.-C. Liou and J. Pretzer, "Effect of curing temperature on the mechanical properties of hydrogen silsesquioxane thin films," *Thin Solid Films*, vol. 335, no. 1, pp. 186–191, 1998.

[18] R. Baillot, *Méthodologie d'analyse de défaillance pour l'évaluation de la fiabilité de diodes électroluminescentes GaN*. PhD thesis, Université Sciences et Technologies-Bordeaux I, 2011.

[19] B. Chambion, *Etude de la fiabilité de modules à base de LEDs blanches pour applications automobile*. PhD thesis, Université de Bordeaux, 2014.

[20] M. A. Green, "Silicon solar cells: state of the art," *Philosophical Transactions of the Royal Society of London A: Mathematical, Physical and Engineering Sciences*, vol. 371, no. 1996, p. 20110413, 2013.

[21] L. Hsu and W. Walukiewicz, "Modeling of InGaN/Si tandem solar cells," *Journal of Applied Physics*, vol. 104, no. 2, p. 024507, 2008.

[22] C. E. Backus, *Solar cells*. Institute of Electrical & Electronics Engineers(IEEE), 1976.

[23] J. Parrott, "Radiative recombination and photon recycling in photovoltaic solar cells," *Solar energy materials and solar cells*, vol. 30, no. 3, pp. 221–231, 1993.

[24] S. R. Wenham, *Applied photovoltaics*. Routledge, 2012.

[25] M. M. de Wild-Scholten, "Energy payback time and carbon footprint of commercial photovoltaic systems," *Solar Energy Materials and Solar Cells*, vol. 119, pp. 296–305, 2013.

[26] I. Fraunhofer, "Photovoltaics report, updated november 11, 2016," *Fraunhofer ISE, Freiburg*, 2016.

[27] M. de Wild-Scholten, M. Sturm, M. Butturi, M. Noack, and K. Heasman, "Environmental sustainability of concentrator pv systems: preliminary lca results of the apollon project," in *5th World Conference on Photovoltaic Energy Conversion Valencia. Spain*, pp. 6–10, 2010.

[28] A. De Vos, "Detailed balance limit of the efficiency of tandem solar cells," *Journal of Physics D: Applied Physics*, vol. 13, no. 5, p. 839, 1980.

[29] S. A. Campbell, S. A. Campbell, and A. C. Stephen, *Fabrication engineering at the micro-and nanoscale*. No. Sirsi) i9780195320176, 2008.

[30] J. Zhao, A. Wang, and M. A. Green, "High-efficiency perl and pert silicon solar cells on fz and mcz substrates," *Solar Energy Materials and Solar Cells*, vol. 65, no. 1, pp. 429–435, 2001.

[31] P. Campbell and M. A. Green, "Light trapping properties of pyramidally textured surfaces," *Journal of Applied Physics*, vol. 62, no. 1, pp. 243–249, 1987.

[32] J. Benick, B. Steinhauser, R. Müller, J. Bartsch, M. Kamp, A. Mondon, A. Richter, M. Hermle, and S. Glunz, "High efficiency n-type pert and perl solar cells," in *2014 IEEE 40th Photovoltaic Specialist Conference (PVSC)*, pp. 3637–3640, IEEE, 2014.

[33] D. Jordan and J. Nagle, "Buried contact concentrator solar cells," *Progress in Photovoltaics: Research and Applications*, vol. 2, pp. 171–176, 1994.

[34] J. Wohlgemuth and S. Narayanan, "Buried contact concentrator solar cells," in *Photovoltaic Specialists Conference, 1991., Conference Record of the Twenty Second IEEE*, pp. 273–277, IEEE, 1991.

[35] H. C. Card and E. S. Yang, "Electronic processes at grain boundaries in polycrystalline semiconductors under optical illumination," *IEEE Transactions on Electron Devices*, vol. 24, no. 4, pp. 397–402, 1977.

[36] W. Paul and D. A. Anderson, "Properties of amorphous hydrogenated silicon, with special emphasis on preparation by sputtering," *Solar Energy Materials*, vol. 5, no. 3, pp. 229–316, 1981.

[37] A. Shah, J. Meier, A. Buechel, U. Kroll, J. Steinhauser, F. Meillaud, H. Schade, and D. Dominé, "Towards very low-cost mass production of thin-film silicon photovoltaic (pv) solar modules on glass," *Thin Solid Films*, vol. 502, no. 1, pp. 292–299, 2006.

[38] A. Shah, P. Torres, R. Tscharner, N. Wyrsch, and H. Keppner, "Photovoltaic technology: the case for thin-film solar cells," *science*, vol. 285, no. 5428, pp. 692–698, 1999.

[39] M. A. Green, K. Emery, Y. Hishikawa, W. Warta, and E. D. Dunlop, "Solar cell efficiency tables (version 45)," *Progress in photovoltaics: research and applications*, vol. 23, no. 1, pp. 1–9, 2015.

[40] U. S. G. Survey, "Tellerium," *Mineral Commodity Summaries*, 2008.

[41] N. R. E. Centre, "First solar cdte photovoltaic technology: Environmental, health and safety assessment," *Published Online*, 2013.

[42] M. Marwede and A. Reller, "Future recycling flows of tellurium from cadmium telluride photovoltaic waste," *Resources, Conservation and Recycling*, vol. 69, pp. 35–49, 2012.

[43] K. Zweibel, "Thin film pv manufacturing: Materials costs and their optimization," *Solar energy materials and solar cells*, vol. 63, no. 4, pp. 375–386, 2000.

[44] J. Kalowekamo and E. Baker, "Estimating the manufacturing cost of purely organic solar cells," *Solar Energy*, vol. 83, no. 8, pp. 1224–1231, 2009.

[45] M. Kemell, M. Ritala, and M. Leskelä, "Thin film deposition methods for cuinse 2 solar cells," *Critical Reviews in Solid State and Materials Sciences*, vol. 30, no. 1, pp. 1–31, 2005.

[46] T. Klinkert, M. Jubault, F. Donsanti, D. Lincot, and J.-F. Guillemoles, "Ga gradients in cu (in, ga) se2: Formation, characterization, and consequences," *Journal of Renewable and Sustainable Energy*, vol. 6, no. 1, p. 011403, 2014.

[47] M. Konagai, M. Sugimoto, and K. Takahashi, "High efficiency gaas thin film solar cells by peeled film technology," *Journal of crystal growth*, vol. 45, pp. 277–280, 1978.

[48] M. Grätzel, "Dye-sensitized solar cells," *Journal of Photochemistry and Photobiology C: Photochemistry Reviews*, vol. 4, no. 2, pp. 145–153, 2003.

[49] A. Kojima, K. Teshima, Y. Shirai, and T. Miyasaka, "Organometal halide perovskites as visible-light sensitizers for photovoltaic cells," *Journal of the American Chemical Society*, vol. 131, no. 17, pp. 6050–6051, 2009.

[50] M. M. Lee, J. Teuscher, T. Miyasaka, T. N. Murakami, and H. J. Snaith, "Efficient hybrid solar cells based on meso-superstructured organometal halide perovskites," *Science*, vol. 338, no. 6107, pp. 643–647, 2012.

[51] C. H. Henry, "Limiting efficiencies of ideal single and multiple energy gap terrestrial solar cells," *Journal of applied physics*, vol. 51, no. 8, pp. 4494–4500, 1980.

[52] P. Rappaport, "The photovoltaic effect and its utilization1 rca rev. 20, 373-397," 1959.

[53] R. Anderson, "Experiments on ge-gaas heterojunctions," in *Electronic Structure of Semiconductor Heterojunctions*, pp. 35–48, Springer, 1988.

[54] "Alta devices achieves 31.6% solar energy efficiency record; changes the fundamental economics for unmanned aerial vehicles." Accessed: 2016-12-17.

[55] E. Jackson, "Areas for improvement of the semiconductor solar energy converter," in *Transactions of the Conference on the Use of Solar Energy*, vol. 5, pp. 122–126, 1955.

[56] P. Chiu, D. Law, R. Woo, S. Singer, D. Bhusari, W. Hong, A. Zakaria, J. Boisvert, S. Mesropian, R. King, *et al.*, "Direct semiconductor bonded 5j cell for space and terrestrial applications," *IEEE Journal of Photovoltaics*, vol. 4, no. 1, pp. 493–497, 2014.

[57] H. Serreze, "Optimizing solar cell performance by simultaneous consideration of grid pattern design and interconnect configuration," in *13th Photovoltaic Specialists Conference*, vol. 1, pp. 609–614, 1978.

[58] L. Vegard, "Die konstitution der mischkristalle und die raumfüllung der atome," *Zeitschrift für Physik A Hadrons and Nuclei*, vol. 5, no. 1, pp. 17–26, 1921.

[59] A. R. Denton and N. W. Ashcroft, "Vegard?s law," *Physical review A*, vol. 43, no. 6, p. 3161, 1991.

[60] O. K. Jani, "Development of wide-band gap ingan solar cells for high-efficiency photovoltaics," 2008.

[61] J. Wu, W. Walukiewicz, K. Yu, J. Ager III, E. Haller, H. Lu, and W. J. Schaff, "Small band gap bowing in in1àxgaxn alloys," *Appl. Phys. Lett*, vol. 80, pp. 4741–4743, 2002.

[62] M. Hori, K. Kano, T. Yamaguchi, Y. Saito, T. Araki, Y. Nanishi, N. Teraguchi, and A. Suzuki, "Optical properties of inxga1?xn with entire alloy composition on inn buffer layer grown by rf-mbe," *physica status solidi (b)*, vol. 234, no. 3, pp. 750–754, 2002.

[63] R. Singh, D. Doppalapudi, T. Moustakas, and L. Romano, "Phase separation in ingan thick films and formation of ingan/gan double heterostructures in the entire alloy composition," *Applied Physics Letters*, vol. 70, no. 9, pp. 1089–1091, 1997.

[64] H. Angerer, O. Ambacher, R. Dimitrov, T. Metzger, W. Rieger, and M. Stutzmann, "PEMBE-growth of gallium nitride on (0001) sapphire: A comparison to MOCVD grown GaN," *MRS Internet Journal of Nitride Semiconductor Research*, vol. 1, p. e15, 1996.

[65] T. Hashimoto, F. Wu, J. S. Speck, and S. Nakamura, "A GaN bulk crystal with improved structural quality grown by the ammonothermal method," *Nature materials*, vol. 6, no. 8, pp. 568–571, 2007.

[66] D. Holec, Y. Zhang, D. S. Rao, C. Kappers, Menno J achnd McAleese, and C. J. Humphreys, "Equilibrium critical thickness for misfit dislocations in III-nitrides," *Journal of Applied Physics*, vol. 104, no. 12, p. 123514, 2008.

[67] C. Hemmingsson, P. Paskov, G. Pozina, M. Heuken, B. Schineller, and B. Monemar, "Growth of bulk gan in a vertical hydride vapour phase epitaxy reactor," *Superlattices and Microstructures*, vol. 40, no. 4, pp. 205–213, 2006.

[68] I.-h. Ho and G. Stringfellow, "Solid phase immiscibility in gainn," *Applied Physics Letters*, vol. 69, no. 18, pp. 2701–2703, 1996.

[69] M. Ichimura and A. Sasaki, "Short-range order in iii-v ternary alloy semiconductors," *Journal of applied physics*, vol. 60, no. 11, pp. 3850–3855, 1986.

[70] S. Y. Karpov, "Suppression of phase separation in InGaN due to elastic strain," *MRS Internet Journal of Nitride Semiconductor Research*, vol. 3, p. e16, 1998.

[71] K. Pantzas, Y. El Gmili, J. Dickerson, S. Gautier, L. Largeau, O. Mauguin, G. Patriarche, S. Suresh, T. Moudakir, C. Bishop, *et al.*, "Semibulk InGaN: A novel approach for thick, single phase, epitaxial InGaN layers grown by MOVPE," *Journal of Crystal Growth*, vol. 370, pp. 57–62, 2013.

[72] R. Puybaret, G. Patriache, M. B. Jordan, S. Sundaram, Y. el Gmili, J.-P. Salvestrini, P. L. Voss, W. A. de Heer, C. Berger, and A. Ougazzaden, "Nanoselective area growth of GaN by metalorganic vapor phase epitaxy on 4H-SiC using epitaxial graphene as a mask," *Applied Physics Letters*, vol. 108, pp. 103105–103105–5, 2016.

[73] S. Strite and H. Morkoç, "Gan, aln, and inn: a review," *Journal of Vacuum Science & Technology B*, vol. 10, no. 4, pp. 1237–1266, 1992.

[74] H. Amano, M. Kito, K. Hiramatsu, and I. Akasaki, "P-type conduction in mg-doped gan treated with low-energy electron beam irradiation (leebi)," *Japanese Journal of Applied Physics*, vol. 28, no. 12A, p. L2112, 1989.

[75] S. Nakamura, M. Senoh, and T. Mukai, "Highly p-typed mg-doped gan films grown with gan buffer layers," *Japanese journal of applied physics*, vol. 30, no. 10A, p. L1708, 1991.

[76] Y. Guo, X. Liu, H. Song, A. Yang, X. Xu, G. Zheng, H. Wei, S. Yang, Q. Zhu, and Z. Wang, "A study of indium incorporation in In-rich InGaN grown by MOVPE," *Applied Surface Science*, vol. 256, no. 10, pp. 3352–3356, 2010.

[77] C. A. Fabien and W. A. Doolittle, "Guidelines and limitations for the design of high-efficiency ingan single-junction solar cells," *Solar Energy Materials and Solar Cells*, vol. 130, pp. 354–363, 2014.

[78] T. Wang, T. Ciszek, C. Schwerdtfeger, H. Moutinho, and R. Matson, "Growth of silicon thin layers on cast mg si from metal solutions for solar cells," *Solar energy materials and solar cells*, vol. 41, pp. 19–30, 1996.

[79] O. Jani, H. Yu, E. Trybus, B. Jampana, I. Ferguson, A. Doolittle, and C. Honsberg, "Effect of phase separation on performance of III-V nitride solar cells," in *22nd European Photovoltaic Solar Energy Conference*, pp. 3–7, 2007.

[80] J. Wu, W. Walukiewicz, K. Yu, W. Shan, J. Ager Iii, E. Haller, H. Lu, W. J. Schaff, W. Metzger, and S. Kurtz, "Superior radiation resistance of in1- xgaxn alloys: Full-solar-spectrum photovoltaic material system," *Journal of Applied Physics*, vol. 94, no. 10, pp. 6477–6482, 2003.

[81] A. Mukhtarova, *Puits quantiques de composés nitrures InGaN/GaN pour le photovaoltaique*. PhD thesis, Grenoble Alpes, 2015.

[82] X. Cai, Y. Wang, B. Chen, M.-M. Liang, W.-J. Liu, J.-Y. Zhang, X.-Q. Lv, L.-Y. Ying, and B.-P. Zhang, "Investigation of InGaN pin homojunction and heterojunction solar cells," *IEEE Photonics technology letters*, vol. 25, no. 1, pp. 59–62, 2013.

[83] C. Yang, X. Wang, H. Xiao, J. Ran, C. Wang, G. Hu, X. Wang, X. Zhang, J. Li, and J. Li, "Photovoltaic effects in InGaN structures with p–n junctions," *physica status solidi (a)*, vol. 204, no. 12, pp. 4288–4291, 2007.

[84] O. Jani, B. Jampana, M. Mehta, H. Yu, I. Ferguson, R. Opila, and C. Honsberg, "Optimization of GaN window layer for InGaN solar cells using polarization effect," in *Photovoltaic Specialists Conference, 2008. PVSC'08. 33rd IEEE*, pp. 1–4, IEEE, 2008.

[85] A. Yamamoto, M. R. Islam, T.-T. Kang, and A. Hashimoto, "Recent advances in InN-based solar cells: status and challenges in InGaN and InAlN solar cells," *physica status solidi (c)*, vol. 7, no. 5, pp. 1309–1316, 2010.

[86] A. Yamamoto, K. Sugita, M. Horie, Y. Ohmura, M. R. Islam, and A. Hashimoto, "Mg-doping and n+-p junction formation in MOVPE-grown $In_xGa_{1-x}n$ (x 0.4)," in *Photovoltaic Specialists Conference, 2008. PVSC'08. 33rd IEEE*, pp. 1–3, IEEE, 2008.

[87] B. R. Jampana, A. G. Melton, M. Jamil, N. N. Faleev, R. L. Opila, I. T. Ferguson, and C. B. Honsberg, "Design and realization of wide-band-gap (2.67 eV) InGaN pn junction solar cell," *Electron Device Letters, IEEE*, vol. 31, no. 1, pp. 32–34, 2010.

[88] P. Misra, C. Boney, N. Medelci, D. Starikov, A. Freundlich, and A. Bensaoula, "Fabrication and characterization of 2.3 eV InGaN photovoltaic devices," in *Photovoltaic Specialists Conference, 2008. PVSC'08. 33rd IEEE*, pp. 1–5, IEEE, 2008.

[89] C. Boney, I. Hernandez, R. Pillai, D. Starikov, A. Bensaoula, M. Henini, M. Syperek, J. Misiewicz, and R. Kudrawiec, "Growth and characterization of InGaN for photovoltaic devices," in *Photovoltaic Specialists Conference (PVSC), 2010 35th IEEE*, pp. 003316–003321, IEEE, 2010.

[90] X. Cai, S. Zeng, and B.-P. Zhang, "Favourable photovoltaic effects in InGaN pin homojunction solar cell," *Electronics letters*, vol. 45, no. 24, p. 1, 2009.

[91] X. Chen, K. Matthews, D. Hao, W. Schaff, and L. Eastman, "Growth, fabrication, and characterization of InGaN solar cells," *physica status solidi (a)*, vol. 205, no. 5, pp. 1103–1105, 2008.

[92] X. Chen, K. Matthews, D. Hao, W. Schaff, L. Eastman, W. Walukiewicz, J. Age, and K. Yu, "Characterization of Mg-doped InGaN and InAlN alloys grown by MBE for solar applications," in *Photovoltaic Specialists Conference, 2008. PVSC'08. 33rd IEEE*, pp. 1–6, IEEE, 2008.

[93] R. Dahal, B. Pantha, J. Li, J. Lin, and H. Jiang, "InGaN/GaN multiple quantum well solar cells with long operating wavelengths," *Applied Physics Letters*, vol. 94, no. 6, p. 063505, 2009.

[94] M.-J. Jeng, Y.-L. Lee, and L.-B. Chang, "Temperature dependences of $In_xGa1-xN$ multiple quantum well solar cells," *Journal of Physics D: Applied Physics*, vol. 42, no. 10, p. 105101, 2009.

[95] K. Lai, G. Lin, Y. Lai, Y. Chen, and J. He, "Effect of indium fluctuation on the photovoltaic characteristics of InGaN/GaN multiple quantum well solar cells," *Applied Physics Letters*, vol. 96, no. 8, p. 081103, 2010.

[96] R. Dahal, J. Li, K. Aryal, J. Lin, and H. Jiang, "InGaN/GaN multiple quantum well concentrator solar cells," *Appl. Phys. Lett*, vol. 97, no. 7, p. 073115, 2010.

[97] Y.-J. Lee, M.-H. Lee, C.-M. Cheng, and C.-H. Yang, "Enhanced conversion efficiency of InGaN multiple quantum well solar cells grown on a patterned sapphire substrate," *Applied Physics letters*, vol. 98, no. 26, p. 263504, 2011.

[98] J.-K. Sheu, C.-C. Yang, S.-J. Tu, K.-H. Chang, M.-L. Lee, W.-C. Lai, and L.-C. Peng, "Demonstration of GaN-based solar cells with GaN/ InGaN superlattice absorption layers," *Electron Device Letters, IEEE*, vol. 30, no. 3, pp. 225–227, 2009.

[99] B. W. Liou, "InGaN–GaN–based solar cells with a multiple-quantum-well structure on SiCN–Si (111) substrates," *Photonics Technology Letters, IEEE*, vol. 22, no. 4, pp. 215–217, 2010.

[100] C. Yang, J. Sheu, X.-W. Liang, M.-S. Huang, M. Lee, K. Chang, S. Tu, F.-W. Huang, and W. Lai, "Enhancement of the conversion efficiency of GaN-based photovoltaic devices with AlGaN/ InGaN absorption layers," *Appl. Phys. Lett*, vol. 97, no. 2, p. 021113, 2010.

[101] Y. Kuwahara, T. Fujii, T. Sugiyama, D. Iida, Y. Isobe, Y. Fujiyama, Y. Morita, M. Iwaya, T. Takeuchi, S. Kamiyama, *et al.*, "GaInN-based solar cells using strained-layer GaInN/GaInN superlattice active layer on a freestanding GaN substrate," *Applied physics express*, vol. 4, no. 2, p. 021001, 2011.

[102] O. Jani, I. Ferguson, C. Honsberg, and S. Kurtz, "Design and characterization of GaN/ InGaN solar cells," *Applied Physics Letters*, vol. 91, no. 13, p. 132117, 2007.

[103] C. J. Neufeld, N. G. Toledo, S. C. Cruz, M. Iza, S. P. DenBaars, and U. K. Mishra, "High quantum efficiency InGaN/GaN solar cells with 2.95 eV band gap," *Applied Physics Letters*, vol. 93, no. 14, p. 3502, 2008.

[104] X. Zheng, R.-H. Horng, D.-S. Wuu, M.-T. Chu, W.-Y. Liao, M.-H. Wu, R.-M. Lin, and Y.-C. Lu, "High-quality InGaN/GaN heterojunctions and their photovoltaic effects," *Applied Physics Letters*, vol. 93, no. 26, p. 261108, 2008.

[105] R.-H. Horng, S.-T. Lin, Y.-L. Tsai, M.-T. Chu, W.-Y. Liao, M.-H. Wu, R.-M. Lin, and Y.-C. Lu, "Improved conversion efficiency of GaN/ InGaN thin-film solar cells," *Electron Device Letters, IEEE*, vol. 30, no. 7, pp. 724–726, 2009.

[106] C.-L. Tsai, G.-S. Liu, G.-C. Fan, and Y.-S. Lee, "Substrate-free large gap InGaN solar cells with bottom reflector," *Solid-State Electronics*, vol. 54, no. 5, pp. 541–544, 2010.

[107] Y. Kuwahara, T. Fujii, Y. Fujiyama, T. Sugiyama, M. Iwaya, T. Takeuchi, S. Kamiyama, I. Akasaki, and H. Amano, "Realization of nitride-based solar cell on freestanding GaN substrate," *Applied physics express*, vol. 3, no. 11, p. 111001, 2010.

[108] E. Matioli, C. Neufeld, M. Iza, S. C. Cruz, A. A. Al-Heji, X. Chen, R. M. Farrell, S. Keller, S. DenBaars, U. Mishra, *et al.*, "High internal and external quantum efficiency InGaN/GaN solar cells," *Applied Physics Letters*, vol. 98, no. 2, p. 021102, 2011.

[109] H. C. Lee, Y. K. Su, W. H. Lan, J. C. Lin, K. C. Huang, W. J. Lin, Y. C. Cheng, and Y. H. Yeh, "Study of electrical characteristics of GaN-based photovoltaics with graded in ga n absorption layer," *Photonics Technology Letters, IEEE*, vol. 23, no. 6, pp. 347–349, 2011.

[110] J.-P. Shim, M. Choe, S.-R. Jeon, D. Seo, T. Lee, and D.-S. Lee, "InGaN-based p–i–n solar cells with graphene electrodes," *Applied physics express*, vol. 4, no. 5, p. 052302, 2011.

[111] J. Lang, C. Neufeld, C. Hurni, S. Cruz, E. Matioli, U. Mishra, and J. Speck, "High external quantum efficiency and fill-factor InGaN/GaN heterojunction solar cells grown by NH_3-based molecular beam epitaxy," *Applied Physics Letters*, vol. 98, 2011.

[112] G. Zhang, Y. Tong, Z. Yang, S. Jin, J. Li, and Z. Gan, "Relationship of background carrier concentration and defects in GaN grown by metalorganic vapor phase epitaxy," *Applied physics letters*, vol. 71, no. 23, pp. 3376–3378, 1997.

[113] S. Heikman, S. Keller, S. P. DenBaars, and U. K. Mishra, "Growth of Fe doped semi-insulating GaN by metalorganic chemical vapor deposition," *Applied Physics Letters*, vol. 81, no. 3, pp. 439–441, 2002.

[114] W. Lee, J.-H. Ryou, D. Yoo, J. Limb, R. D. Dupuis, D. Hanser, E. Preble, M. N. Williams, and K. Evans, "Optimization of Fe doping at the regrowth interface of GaN for applications to III-nitride-based heterostructure field-effect transistors," *Applied Physics Letters*, vol. 90, no. 9, p. 09509, 2007.

[115] A. Castiglia, J.-F. Carlin, and N. Grandjean, "Role of stable and metastable Mg–H complexes in p-type GaN for cw blue laser diodes," *Applied Physics Letters*, vol. 98, no. 21, p. 213505, 2011.

[116] C. G. Van de Walle, "Interactions of hydrogen with native defects in GaN," *Physical Review B*, vol. 56, no. 16, p. R10020, 1997.

[117] L. Dobos, B. Pécz, L. Tóth, Z. J. Horváth, Z. Horvath, A. Toth, E. Horvath, B. Beaumont, and Z. Bougrioua, "Metal contacts to n-GaN," *Applied Surface Science*, vol. 253, no. 2, pp. 655–661, 2006.

[118] A. Schmitz, A. Ping, M. A. Khan, Q. Chen, J. Yang, and I. Adesida, "Metal contacts to n-type GaN," *Journal of Electronic Materials*, vol. 27, no. 4, pp. 255–260, 1998.

[119] H. L. Skriver and N. Rosengaard, "Surface energy and work function of elemental metals," *Physical Review B*, vol. 46, no. 11, p. 7157, 1992.

[120] B. Luther, S. Mohney, T. Jackson, M. A. Khan, Q. Chen, and J. Yang, "Investigation of the mechanism for ohmic contact formation in Al and Ti/Al contacts to n-type GaN," *Applied physics letters*, vol. 70, no. 1, pp. 57–59, 1997.

[121] Y. Lin, S.-J. Chang, Y.-K. Su, T.-Y. Tsai, C. Chang, S.-C. Shei, C. Kuo, and S. Chen, "InGaN/GaN light emitting diodes with Ni/Au, Ni/ITO and ITO p-type contacts," *Solid-State Electronics*, vol. 47, no. 5, pp. 849–853, 2003.

[122] J. Sheu, Y.-K. Su, G.-C. Chi, P. Koh, M. Jou, C. Chang, C. Liu, and W. Hung, "High-transparency Ni/Au ohmic contact to p-type GaN," *Applied physics letters*, vol. 74, no. 16, pp. 2340–2342, 1999.

[123] J. Smalc-Koziorowska, S. Grzanka, E. Litwin-Staszewska, R. Piotrzkowski, G. Nowak, M. Leszczynski, P. Perlin, E. Talik, J. Kozubowski, and S. Krukowski, "Ni–Au contacts to p-type GaN–structure and properties," *Solid-State Electronics*, vol. 54, no. 7, pp. 701–709, 2010.

[124] X. Cao, S. Pearton, A. Zhang, G. Dang, F. Ren, R. Shul, L. Zhang, R. Hickman, and J. Van Hove, "Electrical effects of plasma damage in p-GaN," *Applied physics letters*, vol. 75, no. 17, 1999.

[125] N. Young, E. Perl, R. Farrell, M. Iza, S. Keller, J. Bowers, S. Nakamura, S. DenBaars, and J. Speck, "High-performance broadband optical coatings on ingan/gan solar cells for multijunction device integration," *Applied Physics Letters*, vol. 104, no. 16, p. 163902, 2014.

[126] Y. El Gmili, G. Orsal, K. Pantzas, T. Moudakir, S. Sundaram, G. Patriarche, J. Hester, A. Ahaitouf, J. Salvestrini, and A. Ougazzaden, "Multilayered ingan/gan structure vs. single ingan layer for solar cell applications: A comparative study," *Acta Materialia*, vol. 61, no. 17, pp. 6587–6596, 2013.

[127] L. Sang, M. Liao, N. Ikeda, Y. Koide, and M. Sumiya, "Enhanced performance of ingan solar cell by using a super-thin aln interlayer," *Applied Physics Letters*, vol. 99, no. 16, p. 161109, 2011.

[128] J. W. Ager, L. A. Reichertz, Y. Cui, Y. E. Romanyuk, D. Kreier, S. R. Leone, K. M. Yu, W. J. Schaff, and W. Walukiewicz, "Electrical properties of ingan-si heterojunctions," *physica status solidi (c)*, vol. 6, no. S2, pp. S413–S416, 2009.

[129] H. Zhou, S. Chua, S. Chow, H. Pan, Y. Zhu, Y. Feng, L. Wang, K. Zang, W. Liu, and S. Tripathy, "Characteristics of threading dislocations in zno grown on facet-controlled epitaxial overgrown gan templates," *Journal of Physics: Condensed Matter*, vol. 19, no. 35, p. 356203, 2007.

[130] L. A. Reichertz, I. Gherasoiu, K. M. Yu, V. M. Kao, W. Walukiewicz, and J. W. A. III, "Demonstration of a iiinitride/silicon tandem solar cell," *Applied Physics Express*, vol. 2, no. 12, p. 122202, 2009.

[131] I. Gherasoiu, L. A. Reichertz, K. M. Yu, J. W. Ager, V. M. Kao, and W. Walukiewicz, "Photovoltaic action from inxga1-xn p-n junctions with x¿ 0.2 grown on silicon," *physica status solidi (c)*, vol. 8, no. 7-8, pp. 2466–2468, 2011.

[132] E. Yablonovitch, O. D. Miller, and S. Kurtz, "The opto-electronic physics that broke the efficiency limit in solar cells," in *Photovoltaic Specialists Conference (PVSC), 2012 38th IEEE*, pp. 001556–001559, IEEE, 2012.

[133] X. Wu, C. Elsass, A. Abare, M. Mack, S. Keller, P. Petroff, S. DenBaars, J. Speck, and S. Rosner, "Structural origin of v-defects and correlation with localized excitonic centers in ingan/gan multiple quantum wells," *Applied Physics Letters*, vol. 72, no. 6, pp. 692–694, 1998.

[134] R. M. Farrell, C. Neufeld, S. Cruz, J. Lang, M. Iza, S. Keller, S. Nakamura, S. DenBaars, U. Mishra, and J. Speck, "High quantum efficiency ingan/gan multiple quantum well solar cells with spectral response extending out to 520 nm," *Applied Physics Letters*, vol. 98, no. 20, p. 201107, 2011.

[135] M. Haugk, J. Elsner, T. Frauenheim, T. Staab, C. Latham, R. Jones, H. Leipner, T. Heine, G. Seifert, and M. Sternberg, "Structures, energetics and electronic properties of complex iii-v semiconductor systems," *Physica Status Solidi B Basic Research*, vol. 217, no. 1, pp. 473–512, 2000.

[136] S. Maximenko, S. Soloviev, D. Cherednichenko, and T. Sudarshan, "Electron-beam-induced current observed for dislocations in diffused 4h-sic pn diodes," *Applied physics letters*, vol. 84, no. 9, pp. 1576–1578, 2004.

[137] K. Laaksonen, M. Ganchenkova, and R. Nieminen, "Vacancies in wurtzite gan and aln," *Journal of Physics: Condensed Matter*, vol. 21, no. 1, p. 015803, 2008.

[138] S. Hautakangas, J. Oila, M. Alatalo, K. Saarinen, L. Liszkay, D. Seghier, and H. Gislason, "Vacancy defects as compensating centers in mg-doped gan," *Physical review letters*, vol. 90, no. 13, p. 137402, 2003.

[139] J. Neugebauer and C. G. Van de Walle, "Atomic geometry and electronic structure of native defects in gan," *Physical Review B*, vol. 50, no. 11, p. 8067, 1994.

[140] C. G. Van de Walle and J. Neugebauer, "First-principles calculations for defects and impurities: Applications to iii-nitrides," *Journal of Applied Physics*, vol. 95, no. 8, pp. 3851–3879, 2004.

[141] W.-C. Liu, C.-C. Yang, W.-C. Chen, B.-T. Dai, and M.-S. Tsai, "The structural transformation and properties of spin-on poly (silsesquioxane) films by thermal curing," *Journal of Non-Crystalline Solids*, vol. 311, no. 3, pp. 233–240, 2002.

[142] J. Foresi and T. Moustakas, "Metal contacts to gallium nitride," *Applied physics letters*, vol. 62, no. 22, pp. 2859–2861, 1993.

[143] Y.-F. Wu, W.-N. Jiang, B. Keller, S. Keller, D. Kapolnek, S. Denbaars, U. Mishra, and B. Wilson, "Low resistance ohmic contact to n-gan with a separate layer method," *Solid-State Electronics*, vol. 41, no. 2, pp. 165–168, 1997.

[144] C. Lu, A. Davydov, D. Josell, and L. Bendersky, "Interfacial reactions of ti/n-gan contacts at elevated temperature," *Journal of applied physics*, vol. 94, no. 1, pp. 245–253, 2003.

[145] Q. Liu and S. Lau, "A review of the metal–gan contact technology," *Solid-State Electronics*, vol. 42, no. 5, pp. 677–691, 1998.

[146] A. Motayed, K. A. Jones, M. A. Derenge, M. C. Wood, D. Zakharov, Z. Liliental-Weber, D. J. Smith, A. V. Davydov, W. T. Anderson, A. A. Iliadis, *et al.*, "Electrical, microstructural, and thermal stability characteristics of taõtiõniõau contacts to n-gan," *Journal of applied physics*, vol. 95, no. 3, 2004.

[147] M. E. Levinshtein, S. L. Rumyantsev, and M. S. Shur, *Properties of Advanced Semiconductor Materials: GaN, AIN, InN, BN, SiC, SiGe*. John Wiley & Sons, 2001.

[148] Y. Koide, T. Maeda, T. Kawakami, S. Fujita, T. Uemura, N. Shibata, and M. Murakami, "Effects of annealing in an oxygen ambient on electrical properties of ohmic contacts to p-type gan," *Journal of electronic materials*, vol. 28, no. 3, pp. 341–346, 1999.

[149] J. K. Kim, J. H. Je, J.-L. Lee, Y. J. Park, and B.-T. Lee, "Microstructural investigation of ni/au ohmic contact on p-type gan," *Journal of The Electrochemical Society*, vol. 147, no. 12, pp. 4645–4651, 2000.

[150] J.-K. Ho, C.-S. Jong, C. C. Chiu, C.-N. Huang, K.-K. Shih, L.-C. Chen, F.-R. Chen, and J.-J. Kai, "Low-resistance ohmic contacts to p-type gan achieved by the oxidation of ni/au films," *Journal of Applied Physics*, vol. 86, no. 8, pp. 4491–4497, 1999.

[151] L. Yu and D. Qiao, "Comment on"low-resistance ohmic contacts to p-type gan achieved by the oxidation of ni/au films"[j. appl. phys. 86, 4491 (1999)]," *Journal of applied physics*, vol. 96, pp. 4666–4667, 2004.

[152] G. Greco, P. Prystawko, M. Leszczyński, R. L. Nigro, V. Raineri, and F. Roccaforte, "Electro-structural evolution and schottky barrier height in annealed au/ni contacts onto p-gan," *Journal of Applied Physics*, vol. 110, no. 12, p. 123703, 2011.

[153] H. Ishikawa, S. Kobayashi, Y. Koide, S. Yamasaki, S. Nagai, J. Umezaki, M. Koike, and M. Murakami, "Effects of surface treatments and metal work functions on electrical properties at p-gan/metal interfaces," *Journal of Applied Physics*, vol. 81, no. 3, pp. 1315–1322, 1997.

[154] H. W. Jang, S. Y. Kim, and J.-L. Lee, "Mechanism for ohmic contact formation of oxidized ni/au on p-type gan," *Journal of Applied Physics*, vol. 94, no. 3, pp. 1748–1752, 2003.

[155] I. Chary, A. Chandolu, B. Borisov, V. Kuryatkov, S. Nikishin, and M. Holtz, "Influence of surface treatment and annealing temperature on the formation of low-resistance au/ni ohmic contacts to p-gan," *Journal of electronic materials*, vol. 38, no. 4, pp. 545–550, 2009.

[156] S. Pearton, F. Ren, A. Zhang, and K. Lee, "Fabrication and performance of gan electronic devices," *Materials Science and Engineering: R: Reports*, vol. 30, no. 3, pp. 55–212, 2000.

[157] H. Morkoç, *Handbook of Nitride Semiconductors and Devices: Electronic and Optical Processes in Nitrides*. Springer, 2008.

[158] K. Kumakura, Y. Kobayashia, M. Hiroki, T. Makimotob, T. Akasaka, and H. Yamamoto, "Mechanically transferred gan-based optical and electronic devices-a method for lifting thin-film devices from substrates using hexagonal bn," 2016.

[159] R. Puybaret, S. Suresh, X. Li, Y. El Gmili, K. Pantzas, D. Troadec, G. Patriache, J. Rogers David, F. H. Teherani, E. Sandana Vinod, P. Bove, P. L. Voss, J. Salvestrini, and A. Ougazzaden, "Nanoselective area growth of high quality thick InGaN/GaN on sacrificial ZnO templates," in *E-MRS Spring Meeting*, (Lille, France), 2015.